Terahertz Evanescent Field Imaging and Sensing for Biological Application

By

Suzanna Freer

A thesis submitted to
the University of Birmingham
for the degree of
DOCTOR OF PHILOSOPHY

Metamaterials Research Group
School of Physics and Astronomy
College of Engineering and Physical Sciences
University of Birmingham
March 2022

ABSTRACT

The terahertz regime sits between the infrared and microwave frequencies. Termed the 'terahertz gap', terahertz generation and detection technology remains underdeveloped compared to its bounding frequency bands. Since the first terahertz image in the early 1990s, terahertz has experienced an explosion of interest and development of technology, for biological and medical applications in particular. The regime is rich with spectral fingerprints of biological molecules, with vibrational, rotational and librational modes with terahertz eigenfrequencies. It is non-ionising, in contrast to medical imaging technologies such as x-rays. Meanwhile, it is highly sensitive to water content, a property which can be exploited given that 70% of the human body is composed of water. These properties make terahertz a highly attractive frequency regime for imaging. There is, however, a drawback: a mismatch between terahertz wavelengths and the dimensions of biological analytes such as cells. Hence, efforts have been focused on enhancing interactions with samples. This can be achieved through evanescent fields.

This thesis presents the exploitation of the large water absorption experienced by terahertz radiation for biological sensing and quantitative imaging. The work sets out to improve upon standard time domain spectroscopy (TDS) through evanescent field subwavelength detection. The work involves characterisation of the TDS measurement system using beam profiling techniques, unveiling previously neglected nuances in the terahertz beam. Attention is turned to the extraction of quantitative information from images, through the development of several algorithms, to reliably retrieve the dielectric properties of complex

multilayer samples (heterotopic ossification bone slices). The implementation of the algorithms stems from the desire to overcome widely known and problematic artifacts in extracted dielectric properties. Finally, evanescent fields are exploited for enhanced sensing and imaging beyond standard TDS capabilities. This involved design, fabrication and characterisation of structures supporting evanescent surface waves, demonstrating great potential as highly sensitive liquid sensing platforms for biological applications. Highly efficient and broadband field coupling to a surface wave structure is presented, alongside investigations of evanescent field mechanisms.

DEDICATION

To Poppy

You have given me great happiness.

ACKNOWLEDGMENTS

Looking back upon my time at the University of Birmingham, I find myself indebted to a great number of people who have supported and shaped me and my research, from my undergraduate supervisor at the University of Sheffield, David Mowbray, who inspired my love of research, to my PhD supervisors, Miguel Navarro Cía and Stephen M. Hanham, whose support and guidance proved invaluable.

Beyond the academic scene, there have been a multitude of people who have injected sunlight into the past few years. I will forever be grateful to the Nuclear office for tolerating my imposition, with good vibes and endless humour – would recommend a visit. I would like to thank Ross Allen, Mark Griffiths, Chris Oliver and Angus Hollands in particular, for the great amount of happiness they have given me. My profound appreciation goes to Aidan Hughes, who has been a great friend and support for many years (I owe you one). My deep gratitude goes to Mia Browne, for her boundless positivity and encouragement, and for a great escape to nature through countless Poppy walks. I would like to thank Elida Nekovic, for her compassion and hundreds of kilometers of runs. Hvala ti! You are all an inspiration and I cannot wait to see all the great things you will achieve.

Finally, last but by no means least, I would like to express my deep gratitude to my jumbo-sized family, each of which have had some part in hauling me over the finish line. It is fair to say that, as I write this, I would not have reached this stage without two of my greatest champions, my parents, Sarah and Martin. I owe a large part of my sanity to their overwhelming encouragement and support. You really are superhuman. (Martin, particular thanks for your thesis acknowledgements template.) Lastly, I would like to express

my extreme gratitude to my sister, Emily, for her endless and inspirational kindness. I will forgive your terrible music taste.

SCIENTIFIC OUTPUT

PUBLICATIONS
FROM THESIS WORK

[SF1] **S. Freer**, C. Sui, S. M. Hanham, L. M. Grover, and M. Navarro-Cía, "A Hybrid Reflection Retrieval Method for Terahertz Dielectric Imaging of Human Bone", *Biomedical Optics Express*, 12, 4807–4820 (2021).

Author's contribution: Measurements, numerical results and manuscript write-up was carried out by S. Freer.

[SF2] **S. Freer**, A. Gorodetsky, M. Navarro-Cía, "Beam Profiling of a Commercial Lens-Assisted Terahertz Time Domain Spectrometer," *IEEE Transactions on Terahertz Science and Technology*, 11, 90–100 (2021).

Author's contribution: All experimental work and manuscript write-up was carried out by S. Freer.

[SF3] **S. Freer**, M. Camacho, S. A. Kuznetsov, R. R. Boix, M. Beruete and M. Navarro-Cía, "Revealing the Underlying Mechanisms Behind TE Extraordinary THz Transmission," *OSA Photonics Research*, 8, 430–439, (2019).

Author's contribution: Measurements, CST simulations and manuscript write-up was carried out by S. Freer, under the supervision of M. Navarro Cía.

OTHER

1. M. Camacho, A. Nekovic, **S. Freer**, P. Penchev, R. R. Boix, S. Dimov, and M. Navarro-Cía, "Symmetry and Finite-size Effects in Quasi-optical Extraordinarily THz Transmitting Arrays of Tilted Slots", *IEEE Transactions on Antennas and Propagation*, 68, 6109–6117, (2020).

PEER REVIEWED CONFERENCE PROCEEDINGS FROM THESIS WORK

1. **S. Freer**, C. Sui, L. M. Grover, S. M. Hanham, and M. Navarro-Cía, "Temperature dependent hyperspectral terahertz imaging of human bone for disease diagnosis", *SPIE Photonics West, Advanced Biomedical and Clinical Diagnostic and Surgical Guidance Systems XX* (2022).

2. **S. Freer**, C. Sui, P. Penchev, S. Dimov, A. Gorodetsky, S. M. Hanham, L. M. Grover, and M. Navarro-Cía, "Hyperspectral terahertz imaging for human bone biometrics," *SPIE Optics and Photonics, Terahertz Emitters, Receivers, and Applications XII* (2021).

3. **S. Freer**, R. G. Martínez, D. Perez-Quintana, M. Beruete, S. M. Hanham, M. M. Attallah, and M. Navarro-Cía, "Metal 3D Printed D-Band Waveguide to Surface Wave Transition," *45th International Conference on Infrared, Millimeter and Terahertz Waves (IRMMW-THz)*, (2020).

4. **S. Freer**, M. Camacho, S. A. Kuznetsov, E. Shalom, R. R. Boix, M. Beruete and M. Navarro-Cía, "Modes and Pseudo-modes in TE Extraordinary THz Transmission," *44th International Conference on Infrared, Millimeter, and Terahertz Waves (IRMMW-THz)*, (2019).

5. **S. Freer**, E. Shalom, M. Navarro-Cía, S. A. Kuznetsov, and M. Beruete, "Study of Leaky Waves Responsible for Terahertz TE Extroardinary Transmission," *12th UK-Europe-China Workshop on Millimeter Waves and Terahertz Technologies (UCMMT)*, (2019).

6. A. Gorodetsky, **S. Freer**, and M. Navarro-Cía, "Peculiarities of Commercial PCA based THz Spectrometer Beam Profiling," SPb Photonic, Optoelectronic & Electronic

Materials, SPb - POEM 2020, Saint-Petersburg, Russia, April (2020) – Invited.

7. **S. Freer**, S. A. Kuznetsov, and M. Beruete, and M. Navarro-Cía, "On the behaviour of leaky waves in TE extraordinary terahertz transmission," *Antennas and Propagation Conference 2019 (APC)*, (2019).

OTHER

1. T. Attwood, E. Adams, **S. Freer**, A. J. Vernon, S. M. Hanham, C. Constantinou, L. Azpilicueta and M. Navarro-Cía, "Time and Frequency Analysis of Rough Surface Scattering in the THz Spectrum," *European Microwave Week, London* (2022).

2. E. Adams, T. Attwood, **S. Freer**, S. M. Hanham, C. Constantinou, F. Hu, L. Azpilicueta, and M. Navarro-Cía, "Broadband Characterisation of Interior Materials and Surface Scattering using Terahertz Time-Domain Spectroscopy," *14th UK-Europe-China Workshop on Millimetre-Waves and Terahertz Technologies (UCMMT)* (2021).

3. A. Gorodetsky, **S. Freer**, and M. Navarro-Cía, "Continuous Wave Sub-Terahertz Lensless Holographic Reflective Imaging," *45th International Conference on Infrared, Millimeter and Terahertz Waves (IRMMW-THz)*, (2020).

4. A. Nekovic, M. Camacho, **S. Freer**, P. Penchev, R. R. Boix, S. Dimov, and M. Navarro-Cía, "Taming Extraordinary THz Transmission through sub-λ slot arrays via array truncation, slot rotation, polarization and angle of incidence", *45th International Conference on Infrared, Millimeter, and Terahertz Waves, IRMMW-THz 2020, Buffalo, U.S.A.*, (2020).

5. A. Gorodetsky, **S. Freer**, and M. Navarro-Cía, "Assessment of Cameras for Continuous Wave Sub-Terahertz Imaging," *SPIE Optics + Photonics, San Diego, U.S.A.*, (2020).

6. M. Camacho, **S. Freer**, R. R. Boix, S. A. Kuznetsov, and M. Beruete, and M. Navarro-Cía, "THz time-domain quasi-optical systems for characterisation of frequency selective surfaces," *IET Colloquium on Millimetre-wave and Terahertz Engineering & Technology*, (2019).

7. A. Nekovic, M. Camacho, P. Penchev, **S. Freer**, S. Dimov, R. R. Boix, and M. Navarro-Cía, "Extraordinary Terahertz Transmission Beyond Symmetric Unit Cells: Frequency, Time and Method of Moments Analysis," 14th International Congress on Artificial Materials for Novel Wave Phenomena, Metamaterials' 2020, New York, U.S.A., September (2020).

AWARDS

Margaret K B Day Academic Award for academic excellence in research on Terahertz Evanescent Field Imaging and Sensing for Biological Applications – The British Federation of Women Graduates (2021).

Best Student Paper Award – The UK/Europe-China Workshop on Millimetre-Waves and Terahertz Technologies (2019).

Life isn't about

learning how to weather the storm.

It's about learning how to

dance in the rain.

– Monica Fish

Contents

Acronyms

ASM Angular spectrum method.

CW Continuous wave.

ET Extraordinary transmission.

GDS Grounded dielectric slab.

HA Hydroxyapatite.

HO Heterotopic ossification.

IMPATT Impact avalanche transit-time.

LGDS Leaky grounded dielectric slab.

MSKK Multiply subtractive Kramers-Kronig.

PCA Photoconductive antenna.

PEC Perfect electric conductor.

PP Polypropylene.

SNR Signal to noise ratio.

SSKK Singly subtractive Kramers-Kronig.

SSP Spoof surface plasmon.

TDS Time-domain spectroscopy.

TE Transverse electric.

TM Transverse magnetic.

TPX Polymethylpentene.

XRF X-ray fluorescence.

Chapter One

Introduction

1.1 Development of Terahertz

The terahertz regime sits between the infrared and microwave regimes (Figure 1.1). Coined the 'terahertz gap' [1, 2], generation and detection development in this region lags behind technology in its bounding frequency bands, illustrated in Figure 1.1. Electronic sources used in the microwave region are limited at frequencies exceeding microwave by the switching rate of electronics [3], while optical sources used in the infrared band, whose operation is based on quantum electronic transitions, work at energy scales too high for terahertz generation [4].

Spectroscopy at terahertz frequencies first drew interest in the late 1980s and early 1990s, when the development of femtosecond optoelectronics triggered the generation of terahertz radiation using a time-domain spectroscopy (TDS) system [5]. This remains one of the most prolific methods of terahertz spectroscopy to this day, owed to the unique time-domain nature of the technique. This triggered a rapid development of the field, resulting in the production of a multitude of terahertz sources [6, 7, 8]. These sources can be categorised into two groups: electronic and photonic sources. Electronic sources, or tunable continuous

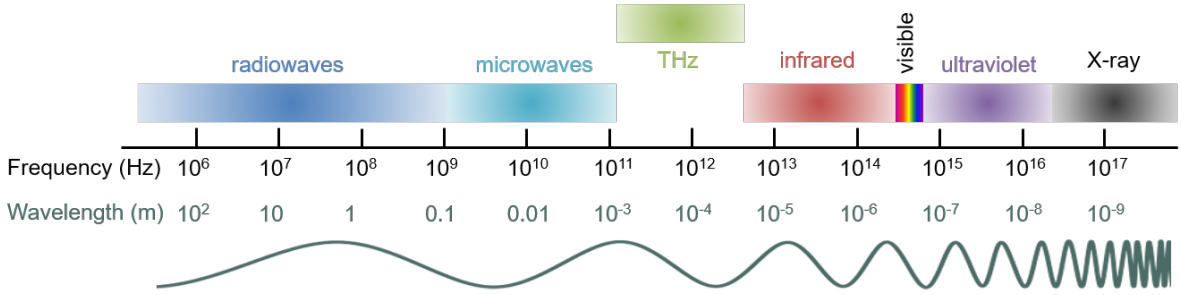

Figure 1.1: Electromagnetic spectrum illustrating the frequency and wavelength of terahertz radiation.

wave (CW) narrowband sources, are derived from the microwave regime, including microwave frequency multipliers such as Gunn diodes [9] and impact avalanche transit-time (IMPATT) diodes [10]. These generate frequencies towards the microwave end of the terahertz spectrum (up to 300 GHz), with limited power at higher frequencies. Photonic sources include optical rectification using nonlinear crystals and photoconductive antennas (PCAs). These sources can generate CW narrowband and pulsed broadband radiation across the terahertz spectrum, finding themselves to be prevalent in the field of terahertz imaging, particularly for medical application.

This region of the electromagnetic (EM) spectrum opened up a view of the microscopic world, which had previously been unexplored. Continued expansion of technologies unlocked the terahertz frequency band for broad application. Terahertz found itself to be valuable for biological [11, 12, 13] and material characterisation, chemical molecular spectroscopy and pharmaceutical manufacturing [14, 15], which utilised the low energy of terahertz photons (4-40 meV), matching the electronic excitations and vibrational modes in solids, and vibrational and rotational transitions in molecules [16]. Meanwhile, lower terahertz frequencies found application in security screening [17], radar imaging and communication [6], pushing towards 6G wireless technology.

1.2 Emergence of Terahertz in biomedicine

The non-ionising nature of terahertz radiation, (unlike x-rays); high hydration sensitivity [18]; and increased spatial resolution over microwaves and ultrasound [19], place terahertz in a prime position as a biomedical imaging technique. The frequency range is rich with spectral fingerprints for biological molecules, with vibrational and rotational modes at terahertz eigenfrequencies [18, 20]. Potential for terahertz as a complementary imaging method has been realised in the field, with research focusing on exploitation of these unique characteristics for realising the potential to monitor real-time changes in molecules through terahertz sensing or imaging [21].

The polar nature, and hence strong polarisability of water molecules [22], generates high interactions with terahertz fields [18]. Large interactions naturally results in large absorption of radiation which, in applications where large water absorption contrasts are valuable, can become an attribute. It enables sensitive measurements of hydration, which is highly valuable in biomedical imaging, where 70% of the human body is composed of water and tissue hydration levels can be used to monitor bodily functions, particularly when health problems arise. One of the first in vivo terahertz images of skin cancers were taken in 2003 [23], presenting improved contrast between healthy and diseased tissue over standard in vitro histological testing. Since then, application of terahertz imaging has reached fields varying from dentistry, for early detection of dental carries [24], to breast cancer differentiation [25].

However, large absorption in water naturally limits the penetration of radiation within materials with high hydration, such as biological tissues. Penetration depths of 1.5 mm of skin for a signal to noise ratio (SNR) of 500:1 have been reported [26]. This is, indeed, a limitation researchers have faced. To overcome this, research has been focused on in vitro imaging of thin, clinically pretreated tissue samples and the use of reflection geometry [27, 28]. These techniques are naturally limited by difficulty in preservation of the original sample

conditions, such as hydration.

1.3 Scaling down to the subwavelength

Advances in terahertz imaging of bulk samples has paved the way for sensing biological systems on the subwavelength scale. The dimension mismatch between biological materials such as cells and the wavelength of terahertz, however, means that the underlying interactions are weak. Hence, enhanced terahertz-matter interactions are required to access these events. Naturally, this can be achieved through increasing the field strength of the probing radiation, up to a limit, beyond which high powers can destroy the sample. The developmental stage of terahertz sources and detectors, however, means that field strength is limited for detectable frequency regimes. To overcome this, one can draw on evanescent fields.

An evanescent field is an oscillating EM field that, unlike an EM wave, does not propagate in space. It remains tightly confined to a material interface, producing regions of high energy density [29]. This means that interactions with its environment are enhanced, allowing for both subwavelength and enhanced field-matter interactions. This can be utilised in biological imaging or sensing of small sample volumes or of molecules smaller than the terahertz wavelength, which cannot be detected through conventional free space approaches. Evanescent fields can be produced by several mechanisms, such as boundaries where total internal reflection occurs: in prisms [30] or optical fibres [31]. Recent advances in metamaterials have opened up extraordinary methods of generating and manipulating evanescent fields on a subwavelength scale. Periodically patterning metallic surfaces can support these surface modes by slowing the phase velocity of a wave, the extent of this being determined by the pattern dimensions. The slower the wave, the more confined the field becomes. Metamaterial design is well versed in the microwave regime, providing a knowledge platform

for researchers to extend towards terahertz frequencies [32, 33]. This ability to engineer the patterns provides a powerful technique for manipulating these confined fields, enabling controllable, enhanced interaction with analytes for on-chip sensing.

1.4 Thesis outline

1.4.1 Beam profiling

Effective use of any spectroscopic [34, 35] and imaging [36] technique fundamentally relies on knowledge of the parameters of the excitation, such as beam profile and polarisation. This determines the excitation region of the sample and field polarisation, information which is hugely important when dealing with in-homogeneous or polarisation sensitive materials. Despite this, coupled with the prolific use of time-domain spectroscopy (TDS) in the terahertz field, limited work has been reported on the characteristics of a beam emitted in a TDS system. Hence, Chapter 2 aims to address this knowledge gap through investigation of the beam properties of the commercially available TDS system used throughout this thesis through a number of standard single pixel profiling techniques [SF2]. This provides a fundamental platform for terahertz TDS imaging within not only the Birmingham group, but the wider terahertz community.

1.4.2 Dielectric imaging for biomedicine

Since the realisation of terahertz imaging as a diagnostic tool in biomedicine in the 1990s, the rapid development of terahertz instrumentation has made systems more affordable and accessible for medical use. This has enabled the formation of an ever-expanding library of dielectric properties at terahertz frequencies of a vast range of tissue types. Armed with

a thorough understanding of the terahertz excitation, Chapter 3 aims to expand on this development through TDS dielectric imaging of thin samples of biological tissue, specifically heterotopic ossification (HO) bone for prospective application to disease detection, extending to prostheses design [37, 38, 39].

For materials with high water content, such as biological samples, large absorption of terahertz radiation make reflection measurements far more practical than transmission. Reflection measurements, however, rely heavily on two factors for accurate retrieval of the material dielectric properties. These are knowledge of the sample thickness and a sample thickness large enough to enable reflected pulses to be resolvable in time. These limitations are well known in the field to generate artefacts in dielectric results, with researchers striving to overcome such complications. Chapter 3 presents a novel algorithm combining Kramers-Kronig calculations and Fabry-Pérot modelling developed to overcome these challenges, aiming for broader applicability and reduced computational complexity over existing solutions [40, 41, 42]. These retrieval processes provide a base for developing sensitive, subwavelength imaging and sensing techniques through evanescent fields, improving upon standard TDS methods [SF1].

1.4.3 Surface waves for enhanced sensing

Chapter 4 scales down from bulk sensing to the micrometer scale, of the order of tens of microns. The mismatch between the wavelength of terahertz, of the order of hundreds of micrometers, and the dimensions of biological cells, of the order of micrometers, limits the sensing capabilities of terahertz fields due to low field-matter interactions. In Chapter 4, the recent advances in metamaterials are exploited for extraordinary methods of manipulating electric fields to generate highly confined evanescent fields on a subwavelength scale. This ability to engineer the patterns provides a powerful technique for manipulating these confined

fields, enabling controllable, enhanced interaction with analytes for on-chip sensing.

To enhance sensitivities through enhancing field-matter interactions, evanescent fields are employed in the form of surface waves [43, 44, 45]. Generation of surface waves through metamaterial design is presented, with large focus on characterisation of field properties such as dispersion and field distribution, in addition to attenuation, a property of which its importance is underestimated in the literature for surface wave application. Inspired by microwave technology, further field enhancement is investigated through enhancing coupling efficiencies to surface modes through structural design [33, 46].

Chapter Two

Beam Profiling

This chapter is an edited version of S. Freer, *et al.*, 'Beam profiling of a commercial lens-assisted terahertz time domain spectrometer,' *IEEE Transactions on Terahertz Science and Technology*, 11(1), 2020, [SF2].

2.1 Overview of beam profiling of TDS systems

The technological development of commercial terahertz instruments [47, 48] in recent years has meant that TDS is far more accessible. TDS is a broadband spectroscopic technique that provides both the temporal response and spectroscopic information of materials [48]. The imaging capabilities of TDS systems have drawn significant attention [36, 49]. Typical imaging methods perform two-dimensional scanning of objects with a focused terahertz beam, limiting the transverse spatial resolution of images [49]. To improve upon this, a combination of pinhole scanning and single pixel detection can be exploited. This increases spatial resolutions to 0.5 mm, while providing full wavefront detection and spectral information of the material [50, 51]. However, a deficit of commercial cameras that are both sensitive to fields generated by a TDS source and have sufficient resolution, coupled with

the large scanning times of two-dimensional raster scanning, means researchers are focusing efforts towards a compressed sensing approach and single pixel detection [52, 53].

Standard commercial terahertz TDS systems are typically made up of an emitter and detector (see Figure 2.1), each with an integrated silicon lens [48, 54]. Beam propagation can be controlled through implementation of quasi-optical components [55] such as lenses and mirrors, illustrated in Figure 2.1. Knowledge of the beam parameters over the entire spectral range of the system is fundamental for both spectroscopy [34, 35] and imaging [36]. This includes both the beam waist, defined as 1/e decay half width of the field amplitude, and its cross-polar level. Pioneering beam characterisation was carried out two decades ago for optical free-space-coupled [56, 57], fiber-coupled [58, 59, 60] and hybrid [61] customised systems, followed by beam characterisation of free-space-coupled in-house systems [62, 63, 64, 65].

Studies of the impact of the detection process on beam profiling however is limited in the open literature. Fibre-coupled systems, while cost effective, are far more flexible than free space systems, in that the emitter and detector are more movable, in that the exciting laser illumination can be moved with the emitter or detector. In this chapter, this flexibility is utilised to de-couple the influence of the (quasi-)optics of the detector, through scanning the pinhole and detector simultaneously.

This chapter presents an extensive beam characterisation of a commercial TERA K15 Mark II all fiber-coupled terahertz TDS system produced by Menlo Systems, with focus on the impact of the detector (quasi-)optics on the estimated beam profile. Given the lack of commercial cameras sensitive to collimated beams from TDS systems, two aperture scanning methods (see Figure 2.3) and a knife-edge method are presented. The aperture scanning approaches consist of raster scanning a pinhole and scanning the pinhole and detector simultaneously, an approach which is unique to fiber-coupled systems. This work has since been

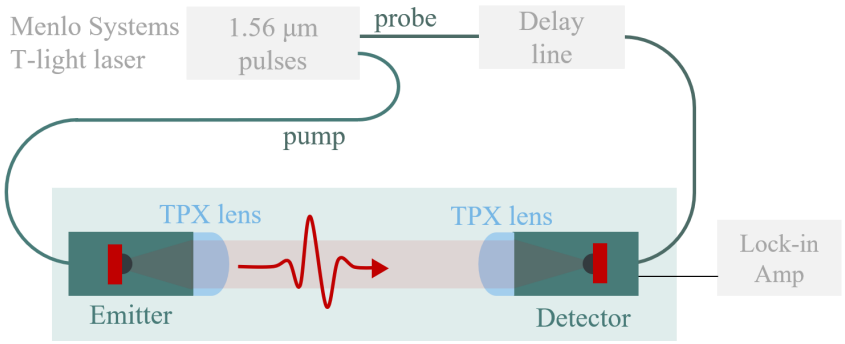

(a) Schematic of TDS system

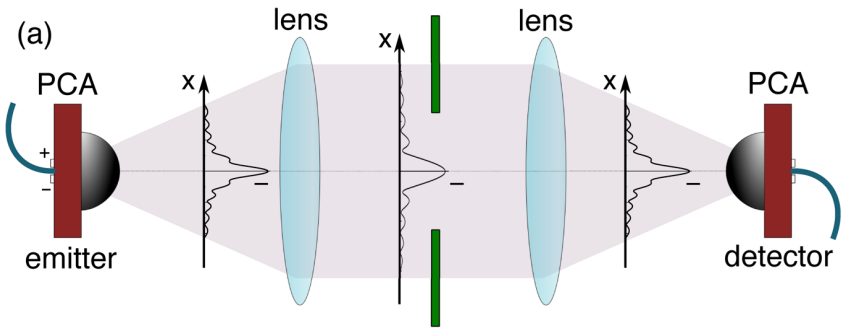

(b) Schematic of TDS emission and detection

Figure 2.1: (a) Schematic of the terahertz time-domain spectrometer. The femtosecond laser is used to trigger the time-domain emission and detection of the terahertz pulses. (b) Optical setup of the TERA K15 terahertz TDS, with illustration of the propogation of beam intensity profiles. Figure taken from [SF2].

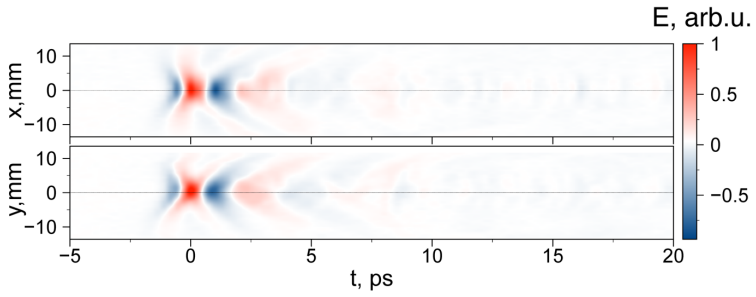

Figure 2.2: X- and Y-time maps of the terahertz beam corresponding to the pinhole-only scan. Figure taken from [SF2].

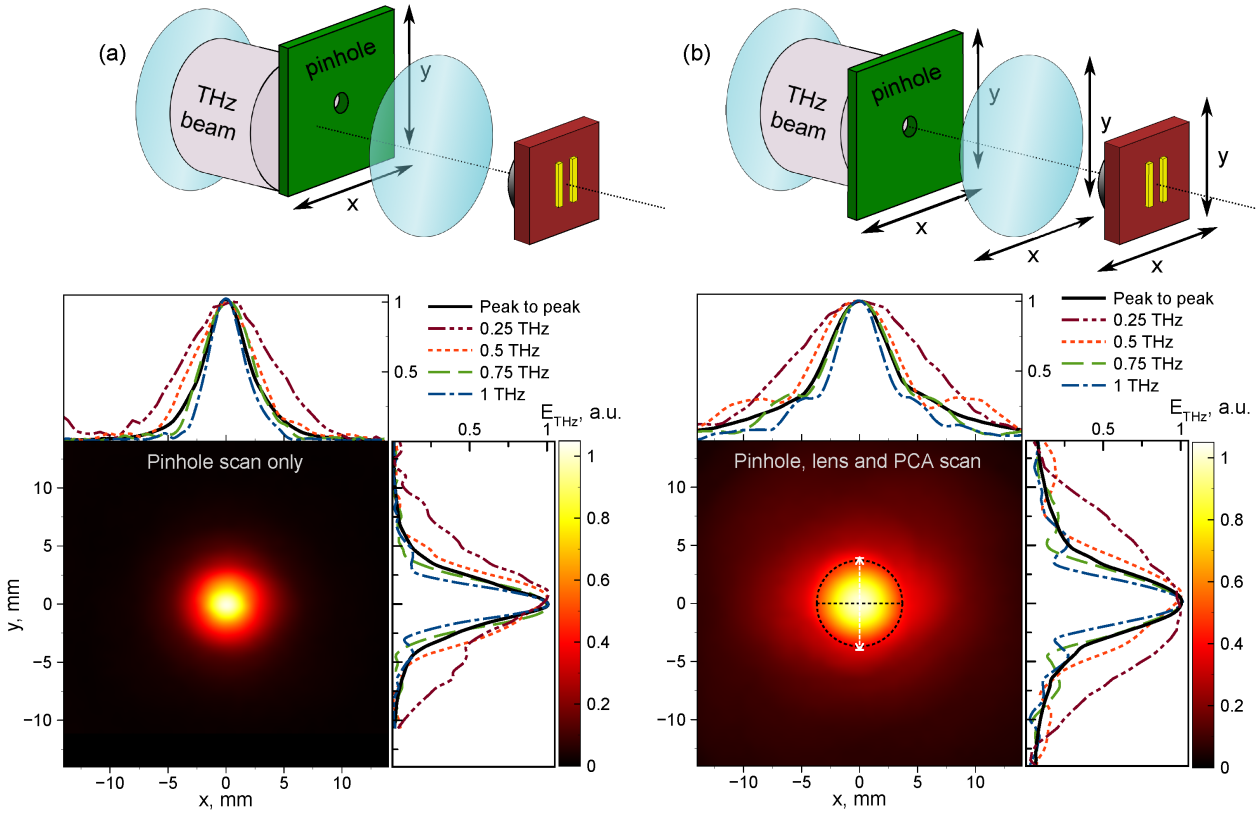

Figure 2.3: Peak-to-peak terahertz beam profiles obtained from two pinhole scanning approaches, illustrated in the top insets. (a) Two-dimensional (2D) raster scan of a ⌀1 mm pinhole-only, and (b) 2D raster scan of a ⌀1 mm pinhole and detector together. The pinhole was placed in the middle point of the terahertz setup. The cross-section plots show the peak-to-peak and frequency dependent profiles. Figure taken from [SF2].

corroborated by analytical work carried out in Ref. [66]. This experimental effort is complemented by stepwise angular spectrum method results, carried out by Dr Andrei Gorodetsky, and a reduced number of computationally-affordable full-wave simulations.

2.2 Profiling approaches, results and initial observations

Within the TERA K15 Mark II system, terahertz radiation is generated and detected by PCA modules manufactured by the Fraunhofer Heinrich-Hertz Institute [67, 68]. Technical details of the PCA modules, system specifications and measurement settings can be found in Appendix 2.5.1. Throughout this thesis, the spectral response of the terahertz field is obtained from the Fourier transformation of the temporal E-field waveform, illustrated in Figure 2.2, using Hanning windowing.

2.2.1 Method A: Pinhole-only scanning

Pinhole-only scanning consists of spatially sampling the terahertz beam by two-dimensional scanning of a pinhole in the xy-plane. This is a standard technique used for both far-field [62] and near-field [69, 70, 71] beam mapping. In these measurements, the pinhole was formed of a 1 mm thick metallic beam block, with a small aperture. Aperture diameter defines both the resolution of the image and SNR of the detected signal. A compromise between the two must therefore be found [62]. In this case, where a pinhole diameter of $\oslash$1 mm was used, a raster scan step of 0.7 mm along both the x and y axes was selected. The distance between the two TPX lenses (see Figure 2.1) was approximately 230 mm, and the scanning plane was at the midpoint of the setup. From the field image presented in Figure 2.3(a), the beam waist of the main lobe was extracted, presented in Figure 2.4 (see Appendix 2.5.2).

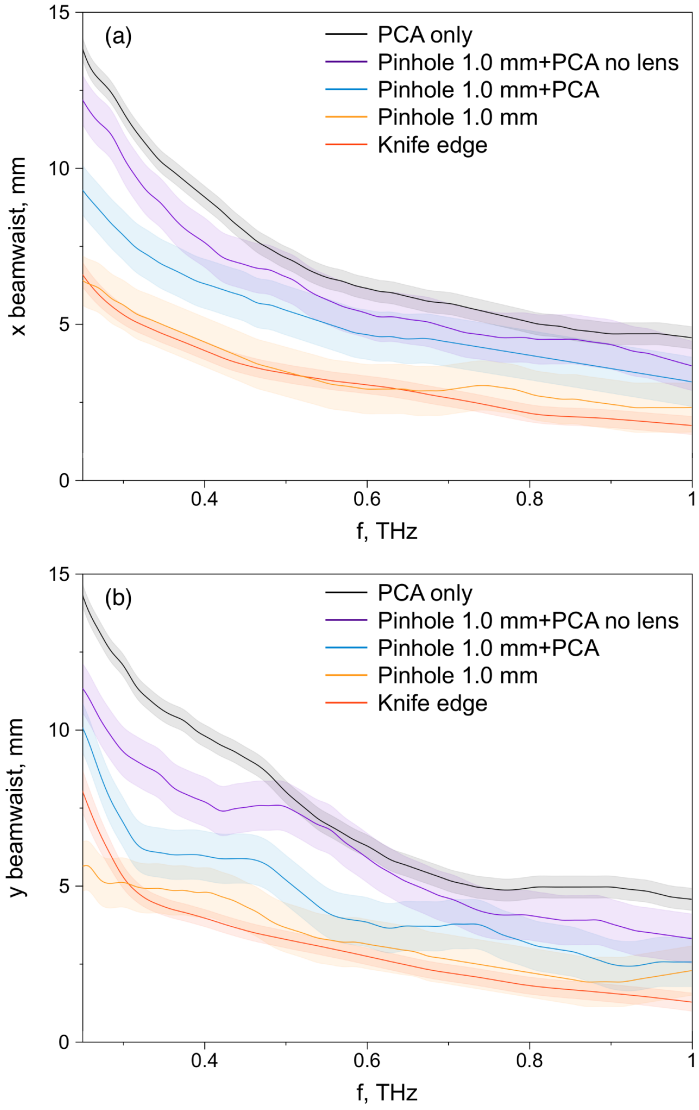

Figure 2.4: Beam waist along (a) x and (b) y as a function of frequency for the five different scanning methods presented in this chapter: the pinhole-only scanning method (method A), the co-aligned pinhole and detector scanning method with (method B) and without focusing TPX lens (method C), the detector scanning method without focusing TPX lens (method D) and the knife-edge method (Appendix 2.5.3). The shaded regions represent beam waist uncertainty. Figure taken from [SF2].

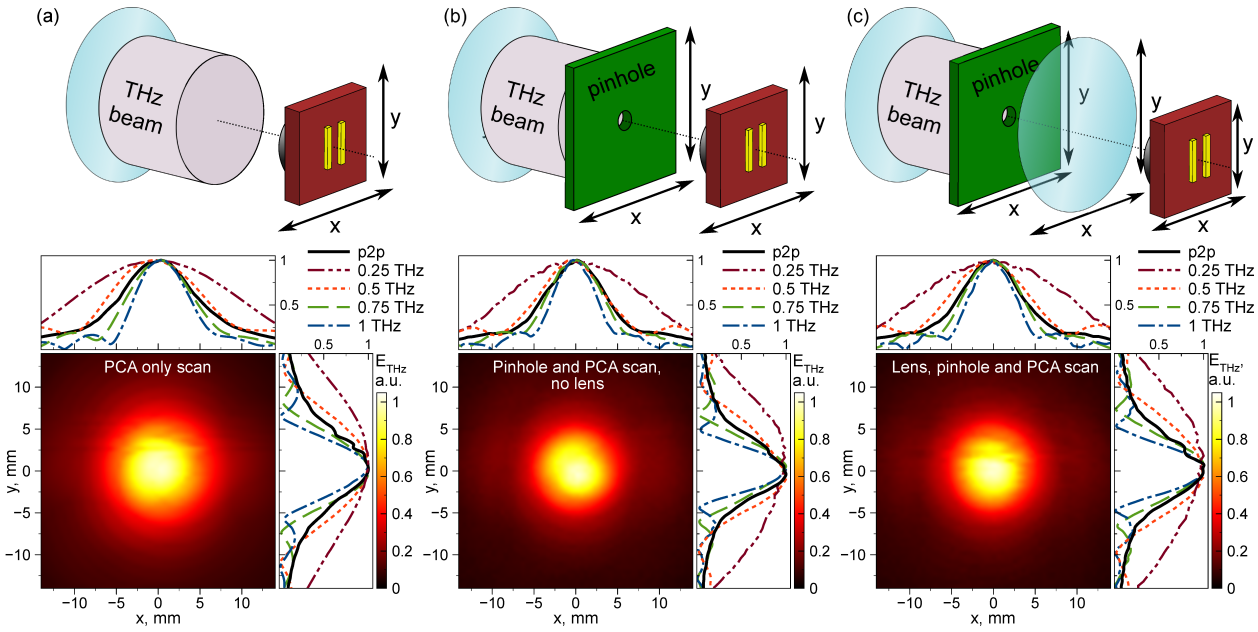

Figure 2.5: Peak-to-peak beam profiles obtained from the three different scanning methods, illustrated in the top insets. (a) Method D: 2D raster scan with the PCA only. (b) Method C: 2D raster scan with the ⌀1 mm pinhole placed at the second TPX lens position, moved together with the PCA detector. (c) Method B_2: 2D raster scan with the ⌀1 mm pinhole placed 4 mm in front of the second TPX lens. The cross-section images show the peak-to-peak and fixed frequency profiles. Figure taken from [SF2].

2.2.2 Method B: Pinhole and detector scanning

To determine the effect of detection on measurements, the detector and pinhole were scanned as a unit. Three scans were undertaken: the first with the detector unit, including TPX lens, positioned ∼100 mm from the pinhole plane, illustrated in Figure 2.3(b). This 15 mm offset compared to method A was introduced purely to enable the pinhole and detector to be mounted on the same xy-translation stage. For the second scan, the pinhole was positioned closer to the detector, ∼4 mm from the TPX lens, illustrated in Figure 2.5(c). It should be noted that in this case the scanning plane was not the centre plane of the setup. The raster scan steps for the first and second methods were 0.7 mm and 0.5 mm, respectively.

The frequency domain field cross-sections presented in Figure 2.3(b) (method B) illustrate an asymmetry along the x and y planes. Consistent with the extracted beam waists in Figure 2.4, a narrower beam waist along the y-axis (H-plane) is evident, supported by the knife-edge results in Appendix 2.5.3. This asymmetry is attributed to the difference in Fresnel reflection of s- and p-polarised light. In the x (E-plane) and y (H-plane) directions, the field is p- and s-polarised, respectively. At the silicon lens surface in both the PCA emitter and detector, p-polarised light exhibits a lower reflection coefficient, and hence higher transmission. This was confirmed by full-wave simulations of the lens-assisted PCA performed in CST Microwave Studio, presented in Figure 2.6(a). The absence of asymmetry in the pinhole-only scan (Figure 2.3(a)) is attributed to the field further from the beam axis having a reduced field projection in the detector plane. Beam asymmetry has also been reported for a more recent generation of emitter modules produced by Fraunhofer Heinrich-Hertz Institute [60].

From the fixed frequency field cross-sections presented in Figure 2.3(b) and 2.5(c), one can observe interference fringes. These fringes are a result of the refractive index boundary between the silicon lens and InP substrate of the emitter [56, 61, 63], consistent with simulations of the lens-substrate configuration performed in CST Microwave Studio. The absence of fringes in the images produced by pinhole-only scanning (Figure 2.3(a)) is attributed to the field projection on the detector. Reduced field projection results in suppression of the side-lobes when the detector is off-axis with the pinhole. Given that pinhole-only scanning is the standard method of beam profiling of TDS systems, this suppression may explain the frequent reports of Gaussian beams [48, 54, 59, 61, 62, 64, 72], in contrast to initial understandings [56].

It should be noted that the temporal length of measurements is also important for observation of interference fringes. Full-wave simulations in CST Microwave Studio, presented in Figure 2.6(b), reveal increasing significance of the interference fringes for longer

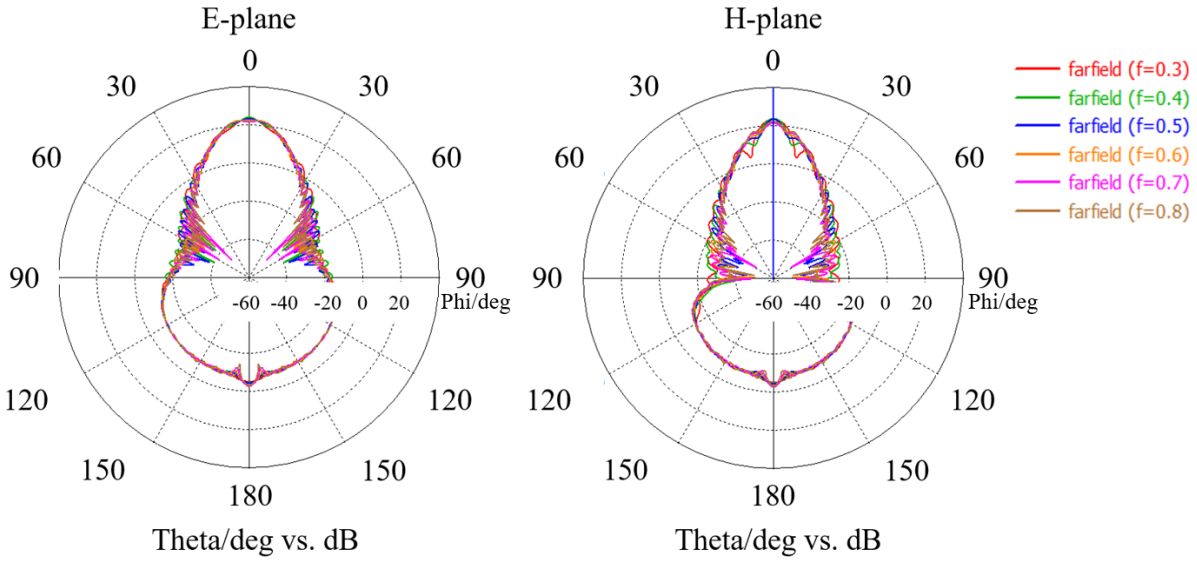

(a) Short waveform ($t = 30$ ps)

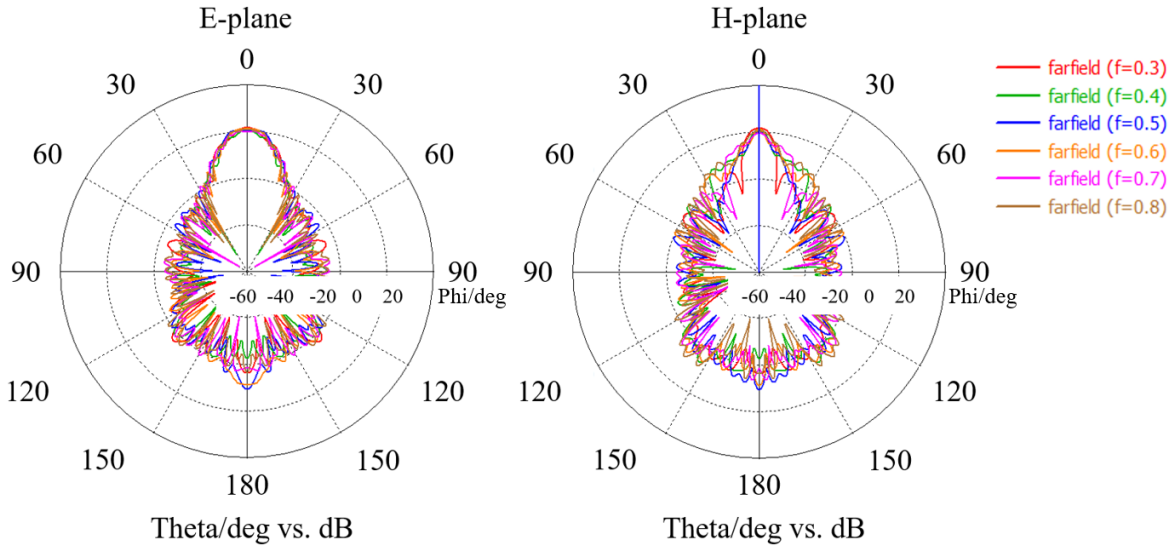

(b) Long waveform ($t = 1000$ ps)

Figure 2.6: Radiation pattern in the E- (left) and H-plane (right) of the lens-assisted PCA simulated in CST Microwave Studio, for multiple frequencies. Theta is the radiation angle in each plane. (a) The measurement window is short, and hence only the leading pulse is considered. (b) The measurement window is long, and therefore internal reflections are considered.

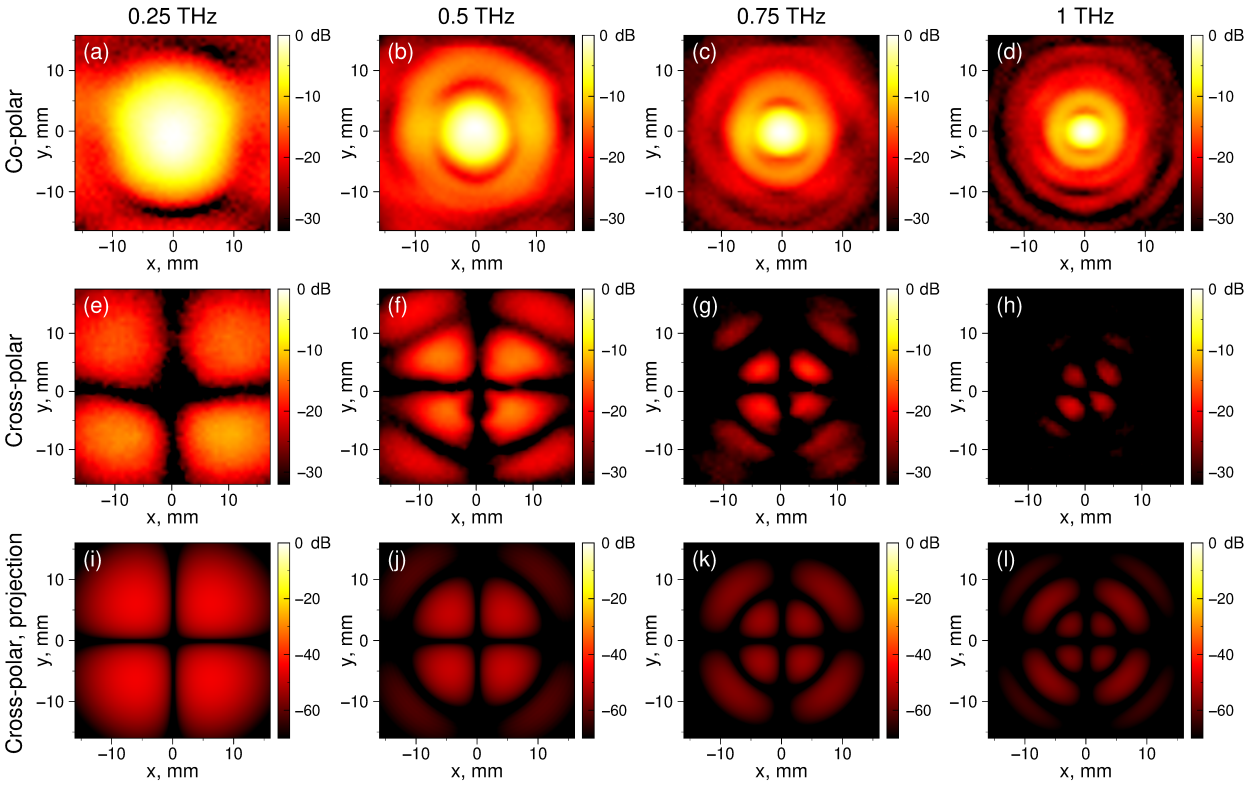

Figure 2.7: Experimental co- (top row) and cross-polarisation (middle row) images of the beam at the middle plane of the setup for 0.25 THz, 0.5 THz, 0.75 THz and 1 THz (from left to right), obtained with the ⌀1 mm pinhole and detector scanning method. (Bottom row) Corresponding simulated cross-polarisation beam images. Figure taken from [SF2].

temporal windows. This is a result of reflections inside the silicon lens and diffraction on the boundaries of the emitter chip. Consideration of these fringes is highly important for spectroscopy and imaging applications that require long time delays, as well as CW system using lens-assisted PCAs, such as photomixing systems [73]. For reference, in this study the measurement window is 52 ps.

2.2.3 Methods C and D: Scanning with TPX lens removed

Through removal of the TPX lens in the detector unit (blue lens in Figure 2.1), one can determine the effect of the lens within the detector unit. In methods C and D, the lens was removed and each scan (PCA scan without and with pinhole) were repeated. The layouts are illustrated in Figure 2.5(a,b). This is a similar approach to that presented in [65], but for a fibre-coupled rather than free-space-coupled system. Note the non-central scanning plane, which is justified through measurements of high beam collimation. The images obtained are presented in Figure 2.5(a,b). The beam profiles for pinhole and PCA scans without and with a TPX lens presented in Figure 2.5(b,c) confirm the negligible effect of the focusing lens on the beam characterisation. This, in turn, confirms the high collimation of the beam. This was supported by scans of the beam at multiple z-planes along the beam axis. From multiple-plane scanning, the divergence (full angle) was calculated to be $\Theta \approx$1.5 deg – 0.7 deg, from 0.25 THz – 1 THz, in both principal planes. The corresponding frequency dependent beam waist is presented in Figure 2.4.

2.2.4 Cross-polarised field distribution

The cross-polar level of a beam, defined as the ratio of the cross-polar component of the field at a specific point in space to the maximum co-polar field, can be used to characterise the beam polarisation purity. Despite its importance for antennas [64, 74, 75], quasi-optical systems [55, 76] and spectroscopy of anisotropic materials [77, 78] and metamaterials [79, 80, 81, 82], consideration of beam polarisation purity is rare for terahertz TDS systems, except on-axis.

An estimation of the cross-polar level in the xy-plane was obtained for two scanning techniques: the pinhole and detector scan (method B) and removed focusing TPX lens scan

(method C). This was achieved through 90 deg rotation of the detector. Deconvolution of the cross-polarisation of the detector was performed through estimation of the detector polarisation sensitivity, as described in Appendix 2.5.4. The deconvolved cross-polar component in the xy-plane is presented in the second row of Figure 2.7 and Figure 2.8. The cross-polar measurements consist of a combination of the cross-polarisation of the emitter and a diverging wave front. Given a vertically polarised Gaussian beam waist at a given location, if one were to propagate this beam to a plane some distance away from the optical axis, the intercepted wavefront would have a non-zero E-field in the horizontal direction. In spherical coordinates, $E_\theta \neq 0$ and $E_\phi = 0$. When this radiation is intercepted at a plane that is normal to $\theta = \pi/2$ and $\phi = 0$, the projection of E_θ at any point on the plane corresponding to $E_\theta \neq 0$ and $E_\phi \neq 0$ produces a non-zero E_x and non-zero E_y. Additionally, given that the origin ($x = 0$, $y = 0$) on the plane is coincident with the $\theta = \pi/2$, $\phi = 0$ axis, the projected horizontal E-field component should be symmetric about the x-axis and y-axis. This is evident in Figure 2.7 and Figure 2.8 and supported by calculated projections extracted from simulations using the stepwise approach to the angular spectrum method (ASM) [83], carried out by Andrei Gorodetsky.

The cross-polar levels extracted from Figure 2.7 and Figure 2.8 are presented in Table 2.1, demonstrating good consistency between methods. In comparison to cross-polar levels of -30 dB reported in high-performance CW quasi-optical systems [55, 76], levels reported here are significantly lower, while being an improvement on levels achieved for in-house leaky lens antennas and PCAs [64, 75].

2.2.5 Beam directivity

The directivity of the emitter can be estimated using the formula:

$$\frac{1}{D} = \frac{1}{2}\left(\frac{1}{D_x} + \frac{1}{D_y}\right), \tag{2.1}$$

Table 2.1: Cross-polar levels extracted from Figure 2.7 and Figure 2.8, for the pinhole and detector scanning method and removed TPX lens scanning method, respectively.

Freq (THz)	Pinhole + PCA Cross-Polar Level (dB)	Removed TPX Lens Cross-Polar Level (dB)
0.25	-11.6	-13.0
0.5	-13.9	-12.1
0.75	-17.3	-16.3
1	-21.2	-20.6

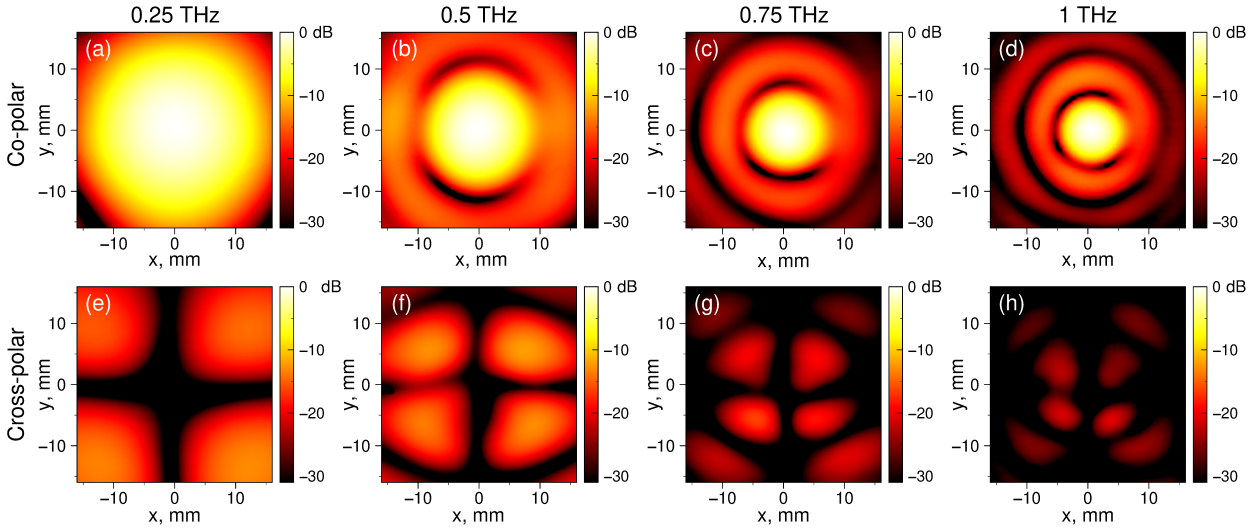

Figure 2.8: Experimental co- (top) and cross-polarisation (bottom) beam maps at the detector plane for 0.25 THz, 0.5 THz, 0.75 THz and 1 THz (from left to right), measured with the PCA only (no pinhole and no TPX lens) scanning method. Figure taken from [SF2].

where D_x and D_y are the directivities extracted from the x and y cross-sections [84], given by

$$D_x = \frac{|E(\theta)|^2_{max}}{\frac{1}{2}\int_0^\pi |E(\theta,0)|^2 sin\theta d\theta} \tag{2.2}$$

and

$$D_y = \frac{|E(\phi)|^2_{max}}{\frac{1}{2}\int_0^\pi |E(\theta,\pi/2)|^2 sin\theta d\theta}, \tag{2.3}$$

where $E(\theta,\phi)$ is the E-field at polar coordinates θ and ϕ. In this work, the frequency dependent beam directivity was extracted from the x and y cross-sections of the pinhole and detector scan profile in Figure 2.7. Figure 2.9 presents the beam directivity with the corresponding divergence (full angle), demonstrating reasonable collimation of the beam. The divergence, similarly to the directivity, was calculated from comparison of beam radii in multiple scanning planes along the beam axis. Menlo Systems report a full-wave at half-maximum divergence angle of 12.5 deg for the emitter without the TPX lens, demonstrating the collimation of the TPX lens in the emitter unit.

2.3 Discussion

In this section, the stepwise approach to ASM simulations of the terahertz beam on the experimental setup were carried out by Andrei Gorodetsky. They are reported here to aid dicussion of results.

2.3.1 Simulation of beam profile propagation

Figure 2.10 presents simulations of the beam profile along the terahertz setup. The ASM was limited to two-dimensional calculation to accelerate calculation time, and was fulfilled

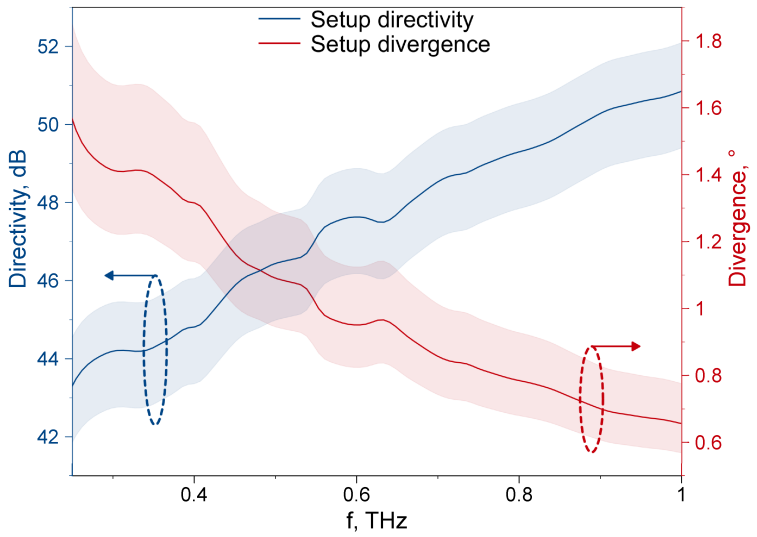

Figure 2.9: Terahertz directivity (blue dashed line, left axis) and divergence (full angle) (red dot-dashed line, right axis) spectra, extracted from the pinhole and detector scan. The shaded regions represent uncertainty extracted from the uncertainty in the distance to the phase centre of the beam. Figure taken from [SF2].

with band-limiting [85]. This assumption was made due to the axial symmetry of the system, neglecting the slight asymmetry of the emitter chip radiation pattern. Initial beam profiles were taken as rectangular, with a width of 4.22 mm for all frequencies. This initial profile produces a field distribution similar to distributions reported for silicon lens coupled PCA in Ref. [56], see Figure 2.11(a). The TPX lenses were accounted for in the thin lens approximation.

The characteristic frequency-dependent beam waist at the midpoint of any 4f confocal setup [16] can be observed in Figure 2.10. These simulations confirm the non-negligible sidelobes observed in the measurements. Hence, the beam in this commercial TDS system cannot be considered Gaussian. With this in mind, the beam waist (i.e. 1/e decay half width of the field amplitude) is defined for the main lobe where the Gaussian function is a good approximation [56]. Beam waists were obtained from the simulation at the midpoint of the

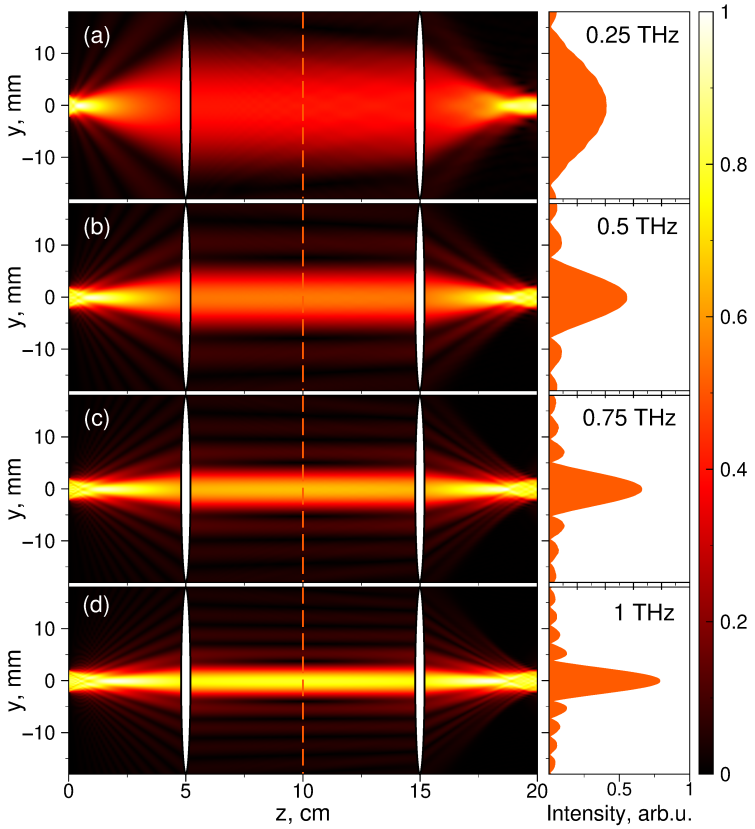

Figure 2.10: Simulated normalised frequency beam profile across the setup computed via the stepwise angular spectrum method. Figure taken from [SF2].

setup (and thus, unaffected by the filtering effect of the detector; this effect is accounted for and discussed below). The calculated beam waists are found to be comparable with the experimental estimates: 6.7 mm at 0.25 THz, 3.4 mm at 0.5 THz, 2.2 mm at 0.75 THz and 1.7 mm at 1 THz.

2.3.2 S- and P-polarised Fresnel reflection

This section presents a study of the simulation of all beam profiling methods undertaken in this work. Initial comparison focuses on methods where the pinhole was at the midpoint of terahertz setup and scanning was performed either by moving the pinhole alone (Figure 2.2(d)

and Figure 2.3(a)) or by moving the pinhole, lens, and detector as a unit (Figure 2.2(e) and Figure 2.3(b)). To simulate these cases, radiation outside the pinhole diameter was blocked. The signal on the detector PCA was estimated as:

$$E = \int_{-r}^{r} T_i(x) \cos(\theta_t(x))\, dx, \tag{2.4}$$

where $T_i(x) = \sqrt{1 - R_i^2}$ is the Fresnel transmission coefficient, r is the distance of the field from the beam axis, i denotes s- or p-polarisation and $\theta_t(x)$ is the angle of refraction inside the hemispherical silicon lens. Note, this simulation does not take into account the similar effect at the emitter PCA, responsible for the beam asymmetry observed in Figures 2.3-2.8 and Figure 2.14. Figure 2.11 (b) presents $T_i(x) * \cos(\theta_t(x))$ for s- and p-polarisations. T_s and T_p did not demonstrate any detectable differences in the simulated field profiles. Figure 2.11 (c-j) therefore only presents the s-polarisation (y-axis field cross-section). Similarly, simulation of the pinhole-only, and the pinhole, lens and detector unit scans did not demonstrate noticeable differences in the beam profile symmetry (see Figure 2.11 (c-d)). The experimental asymmetry is therefore attributed to the difference in Fresnel reflection of s- and p-polarised radiation, as discussed, since this is not fully taken into account in the scalar simulations. Larger discrepancies at lower frequencies are attributed to lower SNR of the TDS system.

Further simulation of each scanning method were undertaken to reveal the origin of the difference in beam waist presented in Figure 2.5. Figure 2.12 presents consistence between the simulation and the experimental PCA-only scan. The effect of the lens in measurements involving the pinhole manifests itself differently. In the experiment, it results in a wider beam, while in the simulation it results in a slightly narrower beam. This is a result of the effect of the Fresnel reflection from the TPX lens, which are unaccounted for in the simulation.

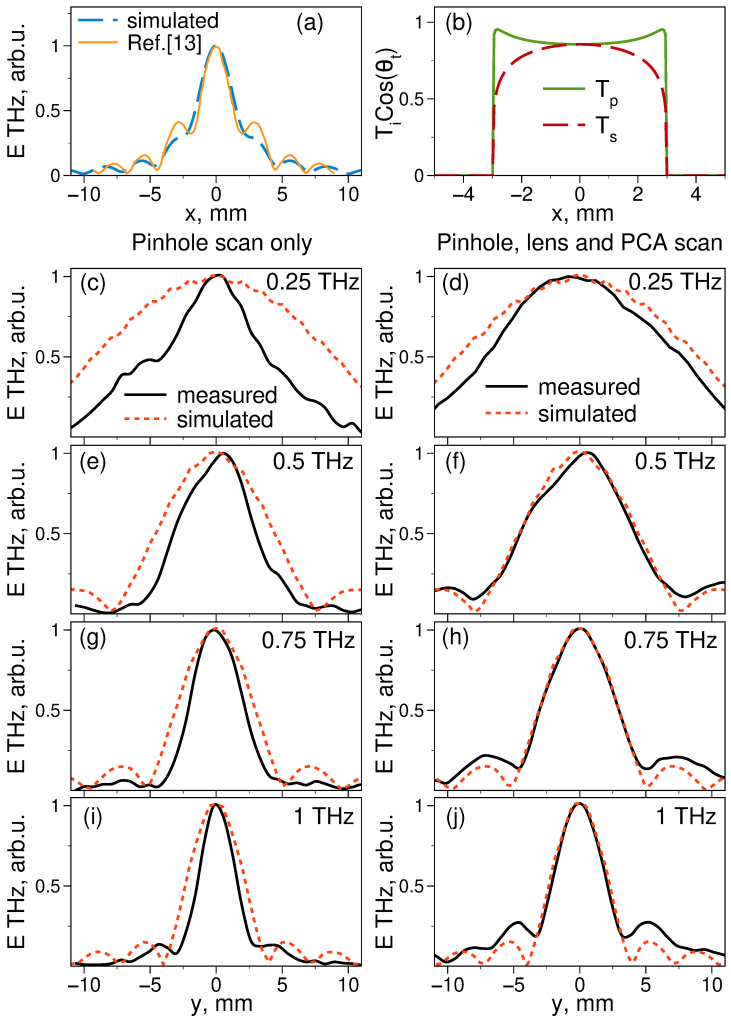

Figure 2.11: (a) Simulated beam profile at 0.586 THz 25 mm from the silicon lens surface with overlayed profile obtained in Ref. [56] at 0.586 THz 35 mm from the silicon lens surface; (b) PCA simulation window for s- and p- polarised radiation; (c) - (j) beam profiles for pinhole-only (c), (e), (g), (i) and pinhole, lens and PCA unit (d), (f), (h), (j) scans. The black line illustrates the experimental data for s- polarised (y) axis, while the red lines show simulated data with scalar fields. Simulations were carried out by Dr Andrei Gorodetsky. Figure taken from [SF2].

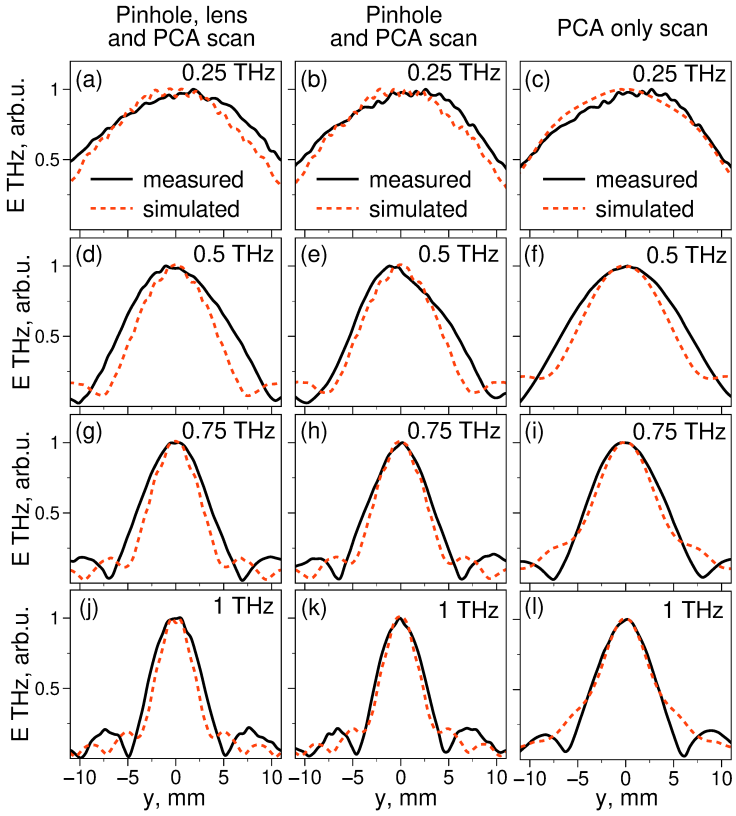

Figure 2.12: Normalised beam profiles at different frequencies: 0.25 THz (a,b,c), 0.5 THz (d,e,f), 0.75 THz (g,h,i), 1 THz (j,k,l) obtained with: (a,d,g,j) a 0.6 mm pinhole placed 4 mm in front of the second TPX lens, (b,e,h,k) a 0.6 mm pinhole placed instead of the second TPX lens, (c,f,j,l) and without a pinhole. In all cases, the PCA, pinhole (where present) and lens (where present) were moved as a unit. Figure taken from [SF2].

2.3.3 Comparison of profiling approaches

The most straightforward beam profiling approach, exploited here, uses single-aperture scanning. More advanced approaches include double-aperture scanning and beam masking followed by single-aperture scanning, termed the Hartmann test. The Hartmann test has been studied for free-spaced-coupled TDS systems [62]. Selection of the appropriate aperture scanning approach naturally depends on the prospective application. This study has revealed that the pinhole and detector scan provides a more accurate beam profile over the pinhole-only scan, with reduced suppression of interference side-lobes stemming from Fresnel reflections. This is confirmed by the simulated ASM results, which show negligible difference between pinhole-only and pinhole and detector scanning. Knowledge of the beam profile is fundamental for applications where the entire beam is used for probing the dielectric properties of materials, and hence the pinhole and detector scan approach would be the optimal profiling method. For applications such as single pixel imaging, where the beam is spatially modulated with a series of masks and the 'bucket' detector remains stationary, the pinhole-only scan provides a pertinent beam waist estimate. The recommended technique therefore depends on two key factors: the availability of time and the application of characterisation.

Table 2.2 tabulates the beam waist estimates using the different experimental approaches. One can see that the results produced by the knife-edge and pinhole scanning methods are in reasonable agreement. However, the pinhole and PCA scan and both scans without TPX lenses provide much larger beam waist measurements. This is thought to be attributed to the reduced E-field projection in the detector plane for the knife-edge and pinhole-only scanning methods. This results in a suppression of the side-lobes, and hence an underestimation of the beam waist. This understanding is corroborated by the supporting simulations, and it can therefore be concluded that scanning the detector with the pinhole provides a more accurate profile of the beam.

2.4 Chapter conclusion

For single pixel imaging, the most prolific beam profiling approach for terahertz TDS systems, a comprehensive understanding of the beam profile of the imaging system is fundamental. Despite this importance, the influence of the profiling technique is often neglected in imaging applications. In this chapter, the beam profile characterisation of a commercial all fiber-coupled TDS system in collimated beam configuration is undertaken through a number of profiling techniques: pinhole-only scanning, simultaneous pinhole and detector scanning (with and without a TPX lens), detector scanning without a pinhole or TPX lens and the knife-edge method, complemented by stepwise ASM simulations. Nuances affecting beam waist estimates are unveiled, including beam asymmetry. This demonstrates that the beam, contrary to the common understanding, is not Gaussian. A Gaussian distribution, however, is a reasonable assumption when the central lobe is considered exclusively. In this instance, the frequency-dependent beam waist ranges from 8.4 mm to 2.8 mm at 0.25 THz to 1 THz. Despite the underestimation of the actual beam waist provided by the pinhole-only scan, the similarity of the scan with the imaging scheme means that this technique would be the most suitable characterisation method for single pixel imaging.

As the core spectroscopic tool used throughout this thesis, the characterisation of the TDS system, including the beam profile and polarisation purity, crucially paves the way for informed imaging and sensing. Chapter 3 investigates single pixel imaging of biological materials, where beam waists estimates are extracted from the pinhole-only scanning approach and cross-polar information is necessary for material anisotropy investigations. Chapter 4 illustrates methods of enhancing fields and sensing through mechanisms such as extraordinary transmission [35], where knowledge of the actual excitation region is fundamental, and hence a pinhole and detector unit scan beam distribution will be assumed.

2.5 Appendices

2.5.1 Appendix A: Time-domain spectrometer settings

The all fiber-coupled terahertz time-domain spectrometer TERA K15 Mark II from Menlo Systems is investigated in this work. Note that its antenna modules are produced by the Fraunhofer Heinrich-Hertz Institute (HHI). The emitter chip is composed of an LT InGaAs/InAlAs on InP multi-layer photoconductive antenna (≈0.35 mm thick in total) in a 25 µm stripline configuration, whose radiation is linearly (x-) polarised, and a ∼6 mm silicon lens [47]. The detector chip is a 25 µm dipole antenna with 10 µm gap and a ∼6 mm silicon lens. Both silicon lenses are substrate-integrated aplanatic hyperhemispherial lenses with 3.5 mm height. The TPX lens has an effective focal length EFL≈54 mm. The terahertz path is not purged, which restricts the usable bandwidth to 1 THz given the signal-to-noise ratio when using pinholes. The lock-in constant was set to 30 ms and the total temporal length of the recorded waveforms was 52 ps to have a spectral resolution of 15 GHz. Figure 2.13 presents a typical waveform and spectrum generated by the experimental setup.

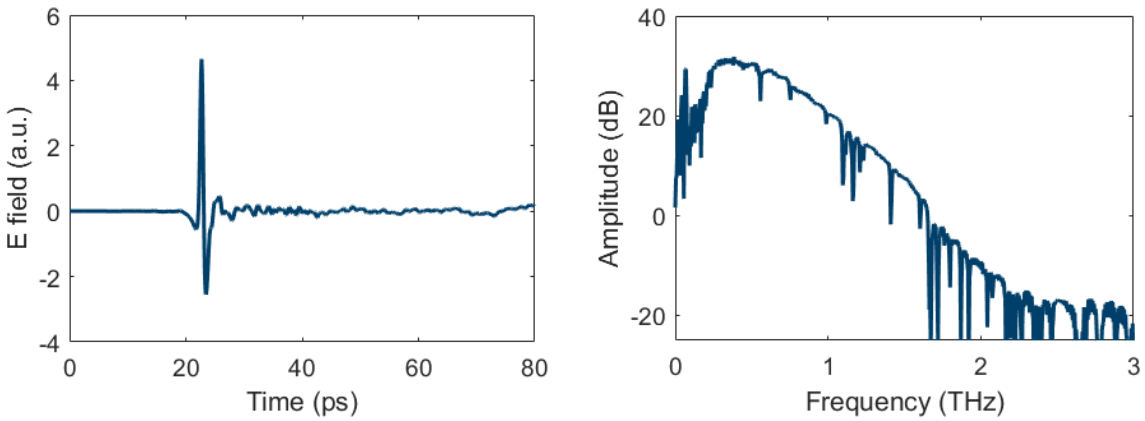

(a) Temporal waveform (b) Frequency domain amplitude

Figure 2.13: (a) Temporal waveform and (b) spectrum of the THz signal generated by the TDS spectrometer used in this work.

Table 2.2: Beam waist (mm) of the collimated terahertz TDS beam at different frequencies and time domain peak-to-peak beam waist. The scanned plane was 115 mm from the emitter TPX lens for the pinhole-only scan, pinhole and detector scan, and knife-edge scan, and 263 mm (226 mm) from the emitter TPX lens for the scan without the TPX lens and without (with) pinhole.

Freq (THz)	Axis	⌀1 mm Pinhole	⌀1 mm Pinhole + PCA	No Pinhole, No TPX lens	⌀1 mm Pinhole, No TPX lens	Knife edge
0.25	X	5.6 ± 0.7	8.4 ± 0.7	13 ± 0.5	10 ± 0.5	6.2 ± 0.3
	Y	5.6 ± 0.7	7.7 ± 0.7	13 ± 0.5	10 ± 0.5	7.4 ± 0.4
0.5	X	3.5 ± 0.7	5.6 ± 0.7	8.5 ± 0.5	6.0 ± 0.5	3.5 ± 0.3
	Y	3.5 ± 0.7	5.6 ± 0.7	8.0 ± 0.5	5.5 ± 0.5	3.4 ± 0.3
0.75	X	2.8 ± 0.7	4.2 ± 0.7	5.5 ± 0.5	4.5 ± 0.5	2.5 ± 0.3
	Y	3.5 ± 0.7	3.5 ± 0.7	5.5 ± 0.5	4.0 ± 0.5	2.0 ± 0.3
1	X	1.4 ± 0.7	3.5 ± 0.7	4.0 ± 0.5	3.5 ± 0.5	1.8 ± 0.3
	Y	1.4 ± 0.7	2.8 ± 0.7	4.5 ± 0.5	3.0 ± 0.5	1.3 ± 0.3
P2P	X	2.8 ± 0.7	4.2 ± 0.7	7.0 ± 0.5	5.5 ± 0.5	3.4 ± 0.3
	Y	2.8 ± 0.7	4.2 ± 0.7	7.0 ± 0.5	5.5 ± 0.5	3.1 ± 0.3

2.5.2 Appendix B: Tabulated beam waists

The main lobe beam waists extracted from the different beam profiling approaches are presented in Table 2.2 for frequencies 0.25 THz, 0.5 THz, 0.75 THz and 1 THz, alongside the beam waist extracted from temporal peak-to-peak images.

2.5.3 Appendix C: Knife-edge scan method

The knife-edge method is a simple technique used to determine beam parameters. Here, a 50 μm thick metallic beam block was translated across the middle plane of the terahertz setup (whose distance between emitter and detector TPX lenses is approximately 230 mm) in both the x and y directions in increments of 0.5 mm, and the decreasing transmitted E-field measured. From this, the beam waist can be extracted from the derivative of the detected power through Gaussian fitting [86], presented in Table 2.2. The field derivatives presented in Figure 2.14(a,b) demonstrate the frequency dependent characteristic of the beam waist. These results show that the beam is slightly asymmetric, which is in agreement with other studies for in-house lens-assisted terahertz systems [59, 61, 64, 75]. Such beam asymmetry results from the combined effect of the slight asymmetric radiation pattern of the feed and polarisation dependent Fresnel coefficients at the silicon-air interface. Meanwhile, these results mask the non-Gaussian distribution of the beam that we report in the main text (previously acknowledged in the seminal work on free-space-coupled TDS systems [56]), and thus, the provided beam waist is only a rough estimate of the true beam waist.

2.5.4 Appendix D: PCA polarisation sensitivity

To remove the effect of the cross-polar sensitivity of the detector from cross-polar results, E-field measurements were taken for varying rotation angle of the detector with respect to the emitter. The detector was positioned 230 mm from the emitter with a polarising grid immediately before it, to ensure linear polarisation of the incident field. The detector was then rotated around the beam axis (z-axis) from 0 deg to 90 deg in increments of 5 deg, to measure the sensitivity of the detector to rotated polarisation. Figure 2.15 presents the Fourier transformed field as a function of rotation angle.

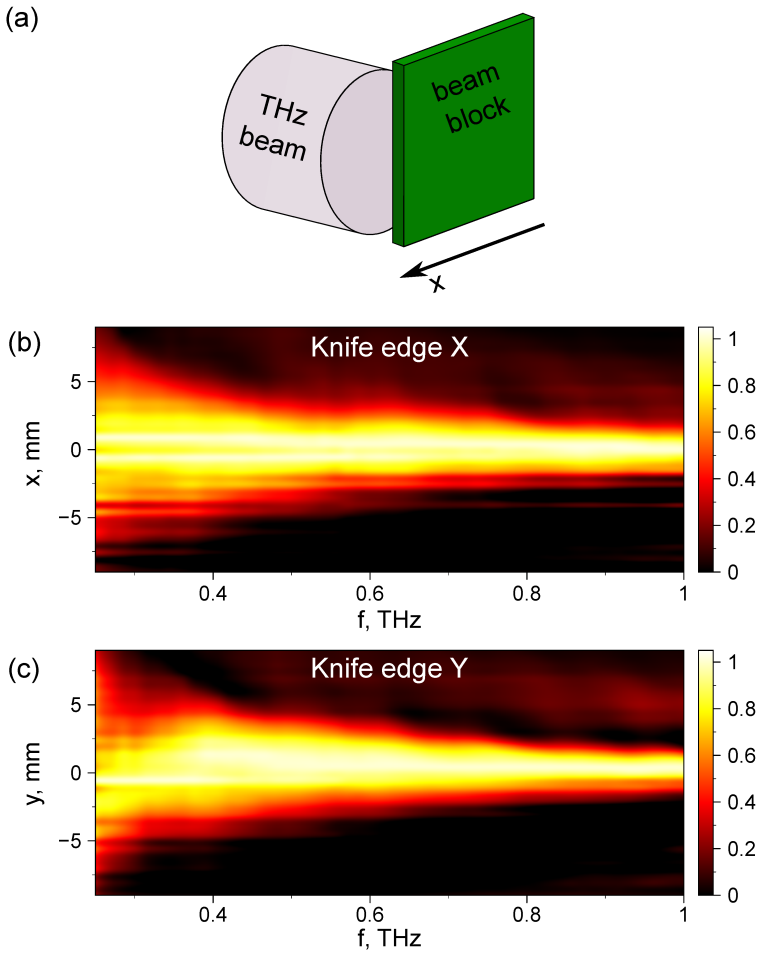

Figure 2.14: (a) Knife-edge method illustration, and (b,c) experimental normalised beam profile spectra obtained from the knife-edge method. Figure taken from [SF2].

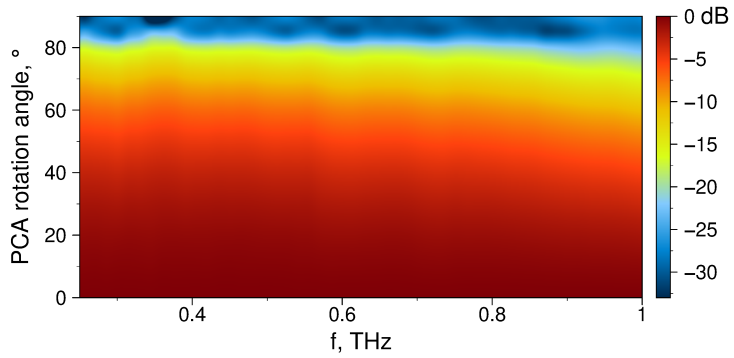

Figure 2.15: Polarisation sensitivity spectrum of the PCA detector chip. Figure taken from [SF2].

A decrease of ∼30 dB is measured from the co-polar to cross-polar measurement across all frequencies. The frequency dependent non-zero field cross-polar measurement was taken into account to correct the registered co- and cross-polar profiles. If we denote the co- and cross-polar PCA sensitivity as $\eta_{\parallel}$ and $\eta_{\perp}$, correspondingly, the measured PCA signals $\tilde{E}_x$ and $\tilde{E}_y$ can be written as:

$$\begin{cases} \tilde{E}_x = \eta_{\parallel} E_x + \eta_{\perp} E_y \\ \tilde{E}_y = \eta_{\parallel} E_y + \eta_{\perp} E_x \end{cases}, \tag{2.5}$$

where the actual field values E_x and E_y can be retrieved by solving the system of equations 2.5 as follows:

$$\begin{cases} E_x = \dfrac{\eta_{\parallel} \tilde{E}_x - \eta_{\perp} \tilde{E}_y}{\eta_{\parallel}^2 - \eta_{\perp}^2} \\ E_y = \dfrac{\eta_{\parallel} \tilde{E}_y - \eta_{\perp} \tilde{E}_x}{\eta_{\parallel}^2 - \eta_{\perp}^2} \end{cases}. \tag{2.6}$$

This correction method was applied to the experimental data to obtain true values of co- and cross-polarised terahertz fields presented in Figs. 2.7 and 2.8.

2.5.5 Appendix E: Far-field CST simulations

The transient solver of CST Microwave Studio was used to simulate the response of the emitter chip with the geometrical dimensions given in Appendix 2.5.1. The stripline and the optical fibre were not modelled to reduce computational effort. The lossless index of refraction of silicon and InGaAs/InAlAs was assumed to 3.42 and 3.41, respectively [54]. The software-defined discrete port was used to model the emission from the photocurrents as a horizontal short dipole at the bottom edge of the InGaAs/InAlAs substrate. Given the twofold symmetry of the problem, a vertical electric and a horizontal magnetic mirror planes were applied to consider only a quarter of the emitter chip. The software-defined open add space boundary conditions (equivalent to a perfectly matched layer) were used for the

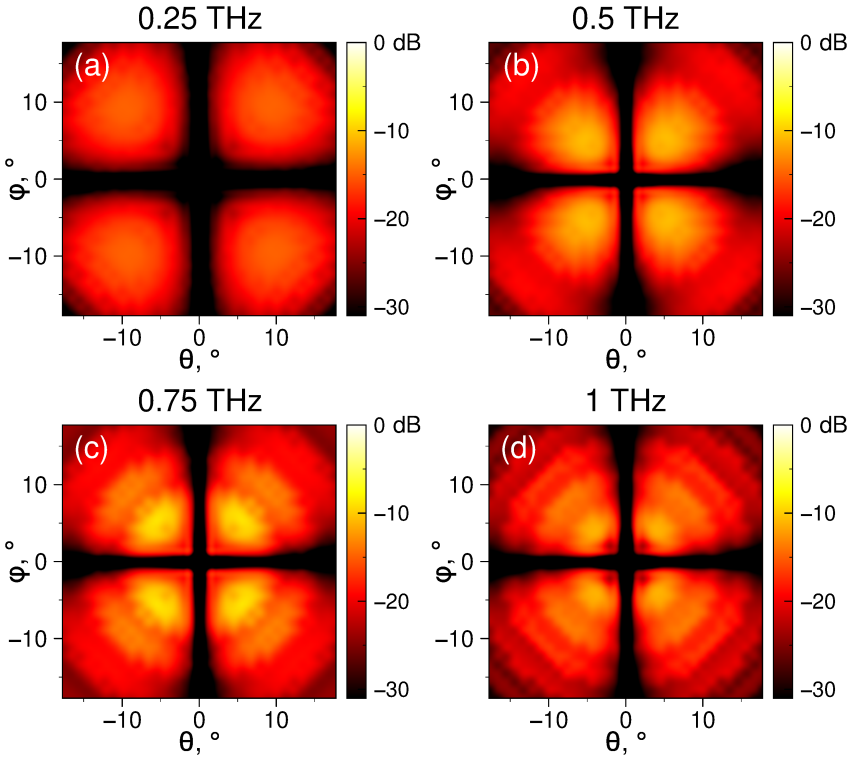

Figure 2.16: Far-field cross-polarisation terahertz beam maps simulated in CST Microwave Studio for (a) 0.25 THz, (b) 0.5 THz, (c) 0.75 THz and (d) 1 THz. Figure taken from [SF2].

simulation box boundaries. Two stopping criteria were considered to either account or not account for the Fabry-Pérot effects arising from wave reflections within the Si lens. For the former, the simulation time stopped when the residual energy in the simulation box volume was 60 dB lower than its peak value. For the latter, the simulation time was truncated when the leading pulse exited the simulation box volume. The far-field cross-polarisation radiation pattern computed using the temporally truncated simulation is shown in Figure 2.16.

Chapter Three

Dielectric Imaging for Biomedicine

The text in this chapter reproduces the following articles:
S. Freer, *et al.*, 'A hybrid reflection retrieval method for terahertz dielectric imaging of human bone,' *Biomedical Optics Express*, 14(8), 4807-4820, 2021 [SF1].
S. Freer, *et al.*, 'Temperature Dependent Hyperspectral Terahertz Imaging of Human Bone for Disease Diagnosis,' *SPIE Photonics West*, 2022 [87].

3.1 Overview of terahertz TDS for biological application

The explosion of interest in biological terahertz imaging stems from numerous spectral biological spectral fingerprints found in the terahertz regime [88]. These features, alongside terahertz hydration sensitivity, have been utilised for both sensing and imaging [89, 90, 91]. Characterisation of human bone has drawn particular interest for detection of metastatic defects and osteoporosis, extending to prostheses design [37, 38, 39, 92]. Existing methods for hydration measurements of bone samples involve calorimetry and require preparation processes which cause significant limitations such as modification of tissue composition [93]. In this study, terahertz TDS imaging is applied to glass-backed heterotopic ossification (HO)

human bone slices, presented in Figure 3.1, for prospective characterisation of disease with reduced sample preparation, as a complimentary technique to existing methods such as nuclear magnetic resonance imaging.

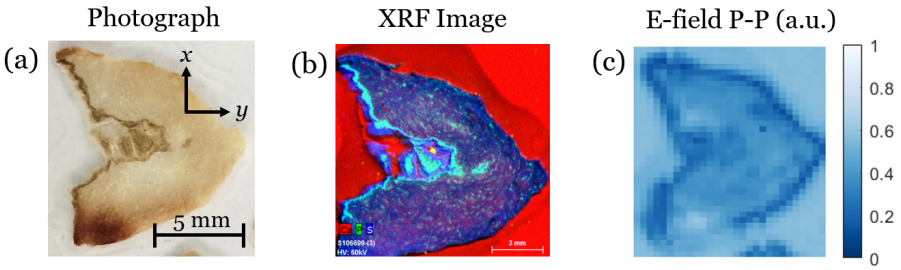

Figure 3.1: (a) Photograph, (b) X-ray fluorescence (XRF) image, with spatial resolution of the order of microns and (c) peak-to-peak value of the temporal reflected terahertz E-field of the glass-backed ∼100 µm heterotopic ossification (HO) bone sample (embedded in resin, found to be transparent at terahertz frequencies through spectroscopic measurements) under investigation. The XRF image illustrates the elemental distributions of the bone slice, where calcium, phosphorus and sulphur (representing collagen) are represented by red, green and blue, respectively. The yellow regions indicate the colocalisation of calcium and phosphorus (representing CaP). Figure taken from [87].

The large focus on terahertz for biological imaging puts significant pressure on the reliability of the extraction of meaningful biometric information. Typically, the dielectric biometric properties of a material are probed through interactions with an E-field, upon either transmission or reflection. A common method of this in the terahertz regime is TDS, where a terahertz field is incident on a material and the modification of the amplitude and phase of the field is detected. Typical high water concentrations of biological materials, alongside the highly absorbing properties of water at terahertz frequencies, makes reflection TDS far more favourable than the transmission configuration. This, in turn, brings additional challenges to biometric extraction, as discussed below.

TDS in reflection configuration involves the measurement of both the amplitude and phase of a terahertz pulse reflected from a sample and reference (glass), see Figure 3.2. Accurate retrieval of the amplitude and phase of the reflected terahertz field, and hence the dielectric properties of materials, relies heavily on two critical factors. The first is accurate alignment of the sample and reference planes [94, 95]. Sub-micrometer accuracy is required, which is an immense practical challenge for manual alignment and with the use of translation stages alike. The second is the ability to resolve Fabry-Pérot reflections that occur within the material structure [40, 42, 96, 97]. As structure thicknesses become optically thin, the reflections within the structure become unresolvable. In this section, a hybrid retrieval algorithm is presented, developed to overcome measurement misalignment and unresolvable reflections, through application of the Kramers-Kronig relations and Fabry-Pérot modelling.

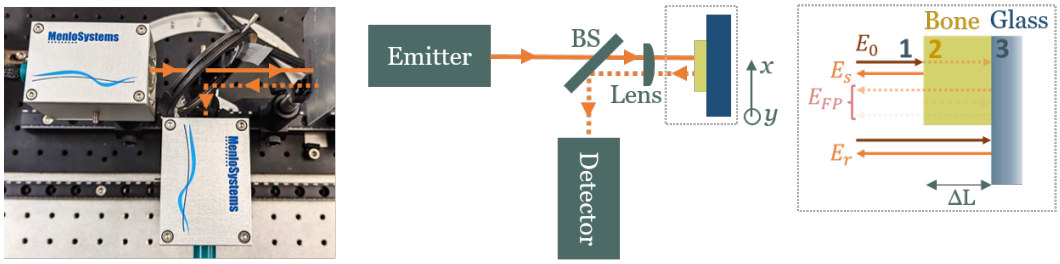

Figure 3.2: Experimental set-up of the THz-TDS in reflection geometry. The terahertz pulse generated by the photoconductive antenna (PCA) emitter passes through the Si beam splitter (BS), focused by a TXP35 lens with focal length 35 mm and is incident on the bone sample. The reflected pulse is then collimated by the same TPX35 lens and reflected by the beam splitter to be detected by the PCA detector. The imaging is performed by scanning the bone sample in the xy-plane using a translation stage. The inset illustrates the path of the E-field, with E_0, E_s, E_r and E_{FP} denoting the incident, sample (bone), reference (glass) and Fabry-Pérot field terms.

3.2 Kramers-Kronig phase retrieval

In practice, retrieval of the E-field phase is challenging. Displacement of the sample position from the reference position ΔL induces an accumulation of phase $\Delta\theta(\omega) = \omega n(2\Delta L/c)$, where n is the refractive index of air and ω and c are the angular frequency and vacuum speed of the wave. Experimental efforts have been made to overcome the sensitive dependence of phase on sample positioning [98, 99, 100]. Limitations of these approaches, such as limited sensitivity, mean researchers have turned their efforts to post processing numerical alternatives, with particular focus on the principle of causality and its expression in the Kramers-Kronig relations.

The Kramers-Kronig relations are bidirectional mathematical equations that describe a fundamental relation between the real and imaginary part of a linear complex function that is analytic in the upper half-plane (positive imaginary part). This is when the principle of causality stands, i.e. the response of a system is zero until an impulse is applied to it. For an analytic function $\chi(\omega) = \chi_1(\omega) + i\chi_2(\omega)$, where ω is a complex variable, the Kramers-Kronig relations are given by

$$\chi_1(\omega) = \frac{1}{\pi} P \int_{-\infty}^{\infty} \frac{\chi_2(\omega')}{(\omega' - \omega)}\, d\omega' \tag{3.1}$$

and

$$\chi_2(\omega) = -\frac{1}{\pi} P \int_{-\infty}^{\infty} \frac{\chi_1(\omega')}{(\omega' - \omega)}\, d\omega', \tag{3.2}$$

where P is the Cauchy principle value, i.e., the integration is performed for any ω' except for $\omega' \neq \omega$.

The refractive index of a material is a complex function which can be described in this way, where dispersion and absorption are described by the real part and imaginary parts, respectively. Hence, if one measures the dispersion of a field propagating through a material, it is possible to obtain the absorption, and vice versa. This fundamental relationship between

the two has proven to be highly valuable in applications in linear [101, 102, 103] and non-linear optics [104, 105, 106].

From Eqs. 3.1 and 3.2, one might notice that the spectrum must be known across a semi-infinite frequency range. In practice, this is unfeasible [107]. Various methods have been studied to overcome this, such as interpolation. Inconsistencies between results undermine these methods. Hence, researchers have looked elsewhere for solutions. Singly subtractive Kramers-Kronig (SSKK) relations and multiply subtractive Kramers-Kronig (MSKK) relations have been exploited for better convergence of the integrals. Hence, the limitations due to the measured finite frequency range are relaxed [105, 106, 108].

This fundamental relationship enforces consistency between the real and imaginary parts of the refractive index of a material, or the amplitude and phase of the interacting electromagnetic field. In this way, one can detect discrepancies between the two. This can be exploited for solving the phase offset problem encountered in TDS in reflection configuration. Any inconsistency between the real and imaginary parts of the detected field can be used to extract and correct for a phase offset, as previously described. A significant advantage of this approach is it is completely general since is not based on a theoretical model of the spectra. Hence, its application can be broad.

This work implements an algorithm developed by V. Lucarini and colleagues [109], through application of SSKK relations. SSKK relations are chosen due to the faster convergence of integrals. The dispersion integrals are given by

$$\ln|r(\omega)| - \ln|r(\omega_1)| = \frac{2(\omega^2-\omega_1^2)}{\pi} P\int_0^\infty \frac{\omega'\theta(\omega')}{(\omega'^2-\omega^2)(\omega'^2-\omega_1^2)}\,d\omega', \tag{3.3}$$

$$\frac{\theta(\omega)}{\omega} - \frac{\theta(\omega)}{\omega_1} = \frac{2(\omega^2-\omega_1^2)}{\pi} P\int_0^\infty \frac{\ln|r(\omega')|}{(\omega'^2-\omega^2)(\omega'^2-\omega_1^2)}\,d\omega', \tag{3.4}$$

where $r(\omega)$ is the complex reflection coefficient, ω_1 is an anchor frequency, P is the Cauchy principle value and θ is the phase. An optimisation approach can be applied to obtain this

error.

The optimisation algorithm, presented in Figure 3.3, involves the iterative application of the SSKK relations to the measured amplitude $\ln|r(\omega)|$ and a corrected phase $\theta(\omega) = \theta(\omega)_{measured} + \Delta\theta(\omega)$ for a range of estimated phase offsets $\Delta\theta(\omega)$. For each iteration, the degree of consistency between the two relations is calculated using the L2 norm $\Delta\|r(\omega)_{guess} - r(\omega)_{corrected}\|_2$. Application of the relations is repeated until the incremental improvement in consistency is less than ϵ (=0.01). Subsequently, the self-consistent reflectivity is calculated, from which the phase offset is extracted.

The application of the algorithm is demonstrated on TDS measurements of the ∼100 µm thick glass-backed HO bone samples, see Figure 3.1. This induces a ∼100 µm offset between sample and reference planes, illustrated in Figure 3.2 (ΔL). Figure 3.4 presents the phase response and extracted dielectric properties of the sample, pre- and post-application of the Kramers-Kronig algorithm. One can observe a large change in phase with frequency in the left panel prior to the phase offset retrieval attributed to the additional phase acquired over distance ΔL, illustrating the sensitivity of the phase. This manifests as a low frequency oscillation in the extracted dielectric properties, presented in the right panel. Upon application of the algorithm, the corrected phase is shown to have a much lower frequency dependence, enabling the reliable extraction of the dielectric properties.

Figure 3.5 presents the L2 norm as a function of anchor frequency ω_1 and estimated phase offset $\Delta\theta(\omega)$. The minimum of the L2 norm is robust, independent of the anchor frequency selection, given that it is within the measured frequency range, demonstrating the stability of the algorithm to the choice of the anchor point. The uncertainty of the calculated phase is largely dependent on the input phase increment, while the run time of the algorithm is limited by both the number of input offsets and anchor frequencies. Calculations of errors of the Kramers-Kronig algorithm can be found in Ref [110]. It is

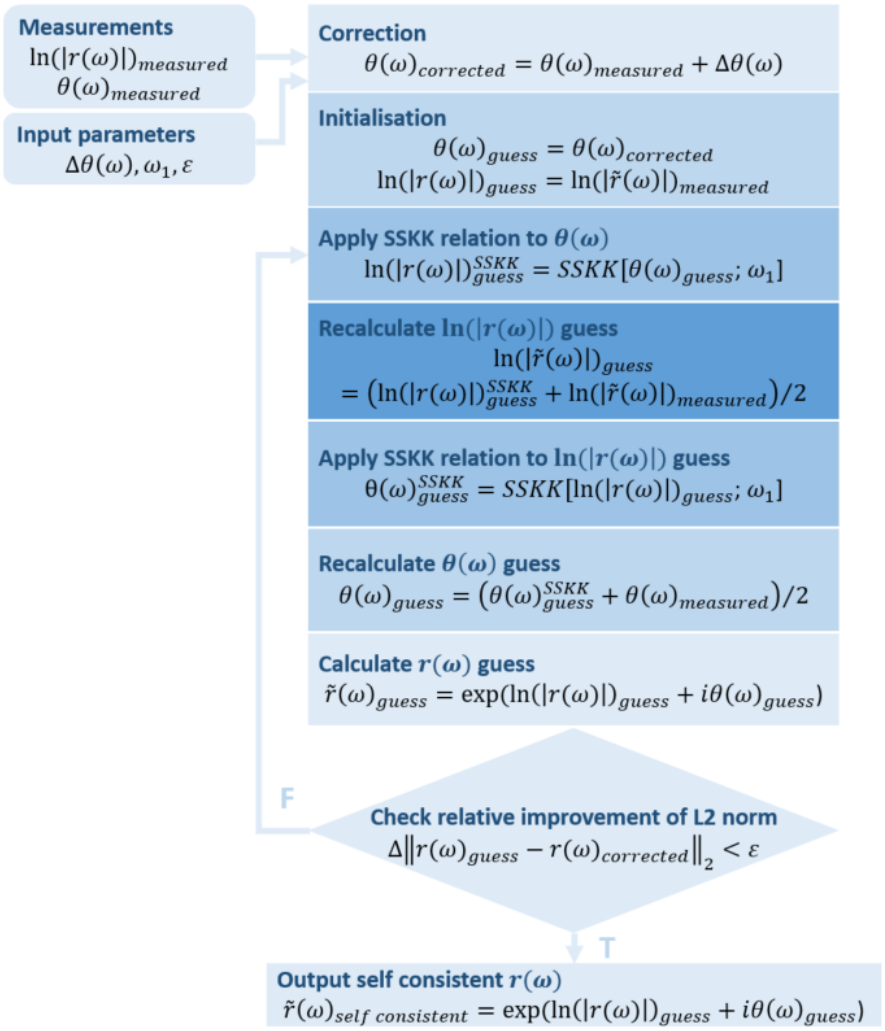

Figure 3.3: Flow diagram of the Kramers-Kronig phase retrieval algorithm. Figure taken from [87].

worth noting that while the algorithm is applied to cases of normal incidence, application can be extended to oblique incidence (not demonstrated in this study), accounting for the additional path length travelled by the field due to the additional angle θ, where the effective path length is given by $L_{eff} = \Delta L/\cos\theta$, illustrated in Figure 3.6.

The retrieval of the phase offset naturally enables the retrieval of the sample thickness. The bone topography was mapped using lasing profiling, for comparison. Profiling details can be found in Appendix C. The thicknesses obtained through lasing profiling and the Kramers-

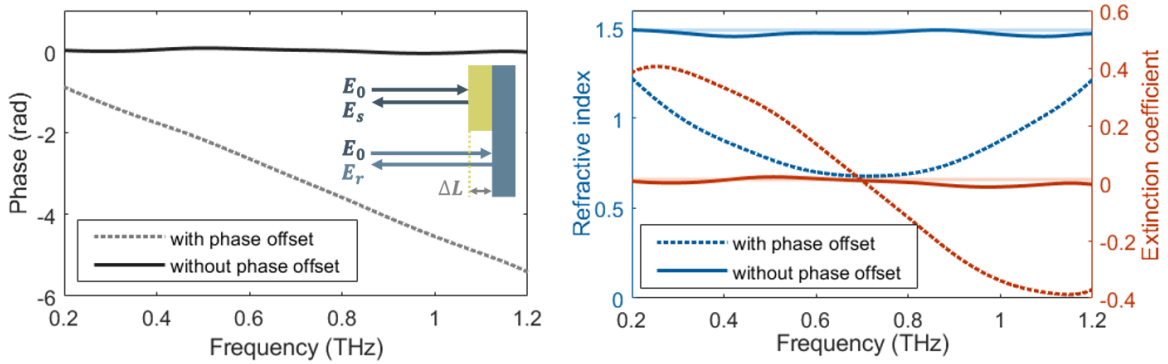

Figure 3.4: Phase response (left) and extracted dielectric properties (right) of a material obtained with a sample-reference plane offset of ∼100 µm, before and after the Kramers-Kronig retrieval algorithm is applied. The inset shows an illustration of a general reference-sample setup, with an offset between the sample and reference planes. E_0, E_s and E_r are the incident, sample and reference E-field amplitudes, respectively. The faded lines illustrate the literature dielectric properties of the sample material, paraffin wax [97]. Figure taken from [87].

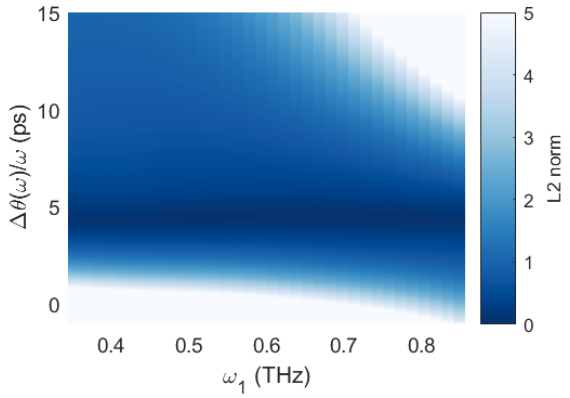

Figure 3.5: L2 norm as a function of normalised estimated phase offset $\Delta\theta(\omega)/\omega$ and anchor frequency ω_1.

Kronig algorithm are presented in Figure 3.7. One can observe good consistency between the two within the bulk region of the sample, confirming the reliability of the algorithm. The deviations at the bone edges are attributed to differences in scattering of the optical and

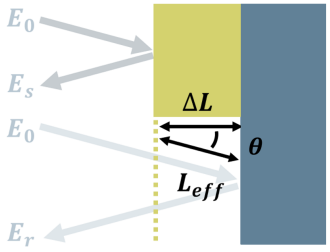

Figure 3.6: Illustration of the effective path length $L_{eff} = \Delta L / \cos\theta$ travelled by the E-field, where θ is the angle of incidence. E_0, E_s and E_r are the incident, sample and reference E-field amplitudes, respectively.

terahertz probing beams, together with the smaller spot size of the laser beam compared to the terahertz beam, which results in a spatially averaged terahertz measurement. The ability to obtain the the sample thickness from the phase correction is crucial for optically thin structures, defined as smaller than the wavelength of light in the medium, where Fabry-Pérot reflections come into play.

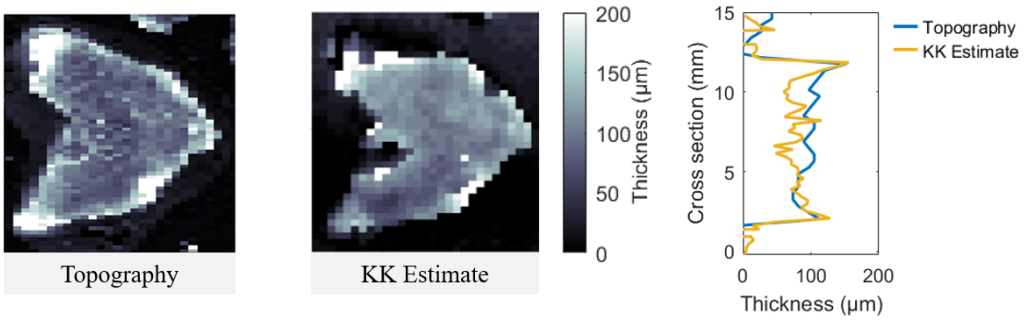

Figure 3.7: Images of the thickness of the bone slice shown in Figure 3.1, obtained through mapping the topography of the bone through lasing profiling and through calculation of the phase offset through application of the Kramers-Kronig relations. The graph on the right shows a comparison of a vertical cross-sectional thickness from each extraction method.

3.3 Modelling Fabry-Pérot reflections

Boundaries between materials of different dielectric properties generate cavities. Within these cavities, multiple reflections of EM waves occur. These are known as Fabry-Pérot reflections. Fabry-Pérot reflections are often exploited in spectroscopy to improve instrument sensitivities by enhancing field-matter interactions. In TDS measurements of optically thin samples, however, they can become problematic [40]. Extraction of dielectric properties of materials crucially relies on the accurate measurement of EM amplitude and phase, and hence the ability to temporally resolve reflected pulses. For TDS measurements of optically thick samples this is straightforward, where the picosecond terahertz pulses exiting the cavity are temporally spaced out. As the sample thickness decreases, the pulses exit the cavity closer together in time, until they are overlap and become unresolvable.

Figure 3.8 demonstrates the effect of Fabry-Pérot reflections on the spectral response of a material obtained through Fourier transformation. The reflected temporal responses were simulated using the transient solver of CST Microwave Studio for structures of different thicknesses, illustrated in the inset. The temporal waveform of the optically thick sample exhibits no Fabry-Pérot reflections within the measurement window. The spectral response is therefore accurately extracted. By reducing the sample thickness, Fabry-Pérot reflections arrive early enough to be be captured by the measurement window. This results in the emergence of oscillations in the spectral response, with decreasing frequency for decreasing thicknesses. These oscillating artifacts are subsequently induced in the extracted dielectric properties.

For the structure with intermediate thickness, the Fabry-Pérot reflection at $\sim$13 ps can be resolved from the initial reflection by standard time-windowing, removing artifacts in the spectral response. For the optically thin sample, however, the initial and subsequent reflections overlap completely. Separation of the terahertz pulses is a non-trivial challenge well

known in the TDS terahertz community for transmission measurement. Efforts have been focused on overcoming this through post-processing techniques such as analytical modelling of reflections [40, 41, 42, 111, 112, 113]. The translation of these methods can be exploited to overcome the same challenges presented in reflection measurements.

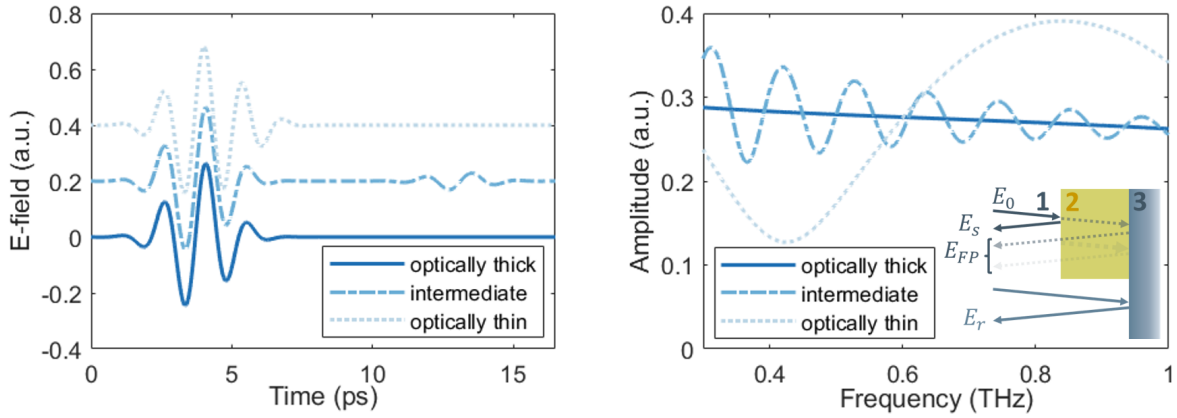

Figure 3.8: Time domain (left) and frequency domain (right) response of optically thick, thin and intermediate structures, simulated using the transient solver of CST Microwave Studio. The temporal waveforms are offset along the y-axis with respect to each other by 0.2 a.u. for clarity. The inset illustrates the sample configuration, for which the sample (layer 2) sits on a reference layer (layer 3). E_0, E_s, E_r and E_{FP} are the incident, sample, reference and Fabry-Pérot E-fields, respectively. Figure taken from [87].

This work presents an alternative field modelling approach to those reported in the literature [40, 42, 41, 111, 112, 113], with particular focus on reduced computational complexity and high generality for simple and broad application. The approach uses three main assumptions: the field is a plane wave with linear polarisation, normally incident on the sample. Given this, the interactions of the field with dielectric layers can be modelled using the Fresnel coefficients. TDS measurements typically require normalisation to extract dielectric information of a sample. This involves a measurement of the reflected field for both a reference material with known dielectric properties and the investigated sample. Here, the field is modelled for a thin sample (layer 2) fixed to a reference sample (layer 3), illustrated

in the inset of Figure 3.8. From the Fresnel coefficients, the sample and reference fields are given by

$$E_{ref}(\omega) = P_1^2 R_{13} E_0, \tag{3.5}$$

$$E_{samp}(\omega) = A_{wo,1} R_{12} E_0 + \underbrace{\{A_{wo,2} T_{12} P_2^2 R_{23} T_{21} + A_{wo,3} T_{12} P_2^4 R_{23}^2 R_{21} T_{21} + ...\} E_0}_{\text{Fabry-Pérot terms}}, \tag{3.6}$$

where ω is the angular frequency, E_0 is the incident E-field, T, R and P are the transmission, reflection and propagation coefficients and $A_{wo,m}$ is a complex factor dependent on frequency and angle-of-incidence that takes into account the walk-off effect of the Fabry-Pérot reflections that results in a different coupling of each reflected sample signal to the detector compared to the reference signal. This factor is inherently difficult to quantify formally, but it can be empirically estimated through calibration [114]. $A_{wo,m} \approx 1$ for optically thin samples, such as layer 2 and $A_{wo,m} = 1$ for normal incidence. The reflection coefficients for each polarisation (s/p) of the incident field are given by

$$R_{ij,s}(\omega) = \frac{\tilde{n}_i \cos\theta_i - \tilde{n}_j \sqrt{1 - \left(\frac{\tilde{n}_i}{\tilde{n}_j} \sin\theta_i\right)^2}}{\tilde{n}_i \cos\theta_i + \tilde{n}_j \sqrt{1 - \left(\frac{\tilde{n}_i}{\tilde{n}_j} \sin\theta_i\right)^2}}, \tag{3.7}$$

$$R_{ij,p}(\omega) = \frac{\tilde{n}_i \sqrt{1 - \left(\frac{\tilde{n}_i}{\tilde{n}_j} \sin\theta_i\right)^2} - \tilde{n}_j \cos\theta_i}{\tilde{n}_i \sqrt{1 - \left(\frac{\tilde{n}_i}{\tilde{n}_j} \sin\theta_i\right)^2} + \tilde{n}_j \cos\theta_i}, \tag{3.8}$$

with $(ij) = (12)$, (13), (23) and (21), where 1, 2 and 3 are material labels, and $\tilde{n}$ is the complex refractive index. The transmission coefficients can be derived from the reflection coefficients, given by

$$T_{kl,s}(\omega) = 1 + R_{kl,s}, \tag{3.9}$$

$$T_{kl,p}(\omega) = (1 + R_{kl,p}) \frac{\cos\theta_1}{\cos\theta_2}, \tag{3.10}$$

with $(kl) = (12)$ and (21), where θ_2 is the angle of refraction and incidence inside material

2, and is defined by $\theta_2 = \sin^{-1}\left((\tilde{n}_1/\tilde{n}_2)\sin\theta_1\right)$. The propagation coefficient is given by

$$P_q(\omega, L) = \exp\left(-i\tilde{n}_q\omega(L/\cos\theta_q)/c\right), \tag{3.11}$$

where q is the material label for layers 1 and 2. The transfer function, defined as the ratio of the sample and reference fields, is therefore given by

$$H(\omega) = \frac{1}{P_1^2 R_{13}}[A_{wo,1}R_{12} + \underbrace{\{A_{wo,2}T_{12}P_2^2R_{23}T_{21} + A_{wo,3}T_{12}P_2^4R_{23}^2R_{21}T_{21} + ...\}}_{\text{Fabry-Pérot terms}}]. \tag{3.12}$$

Given the dielectric response of the reference material, the properties of the sample can be retrieved through a comparative approach. Here, layer 3 is thick enough such that Fabry-Pérot reflections are outside the temporal measurement window. The terms within the layer therefore do not need to be considered. The versatility of field modelling, however, means that this approach can be applied to a range of configurations, for example, where layer 3 is optically thin.

The optimisation algorithm, illustrated in Figure 3.9, involves a frequency dependent two-dimensional scan of a dielectric parameter space. The transfer function $H(\omega)_{guess}$ is calculated for a range of estimated sample refractive indices n and extinction coefficients κ, using the sample thickness L extracted from the Kramers-Kronig algorithm. It is important to note that the phase sensitivity of the dielectric response means that the performance of the Kramers-Kronig algorithm prior to Fabry-Pérot modelling is crucial for reliable dielectric retrieval. The transfer function is discretised with respect to frequency and the error between the measured and estimated transfer functions, $H(\omega)_{meas}$ and $H(\omega)_{guess}$, is then calculated from the combined L2 norm of the amplitude and phase. The location of the minimum L2 norm subsequently provides the output frequency dependent refractive index and extinction coefficient.

Prior to application to samples of unknown dielectric properties, the Fabry-Pérot modelling algorithm was applied to simulated reflected fields from structures with known di-

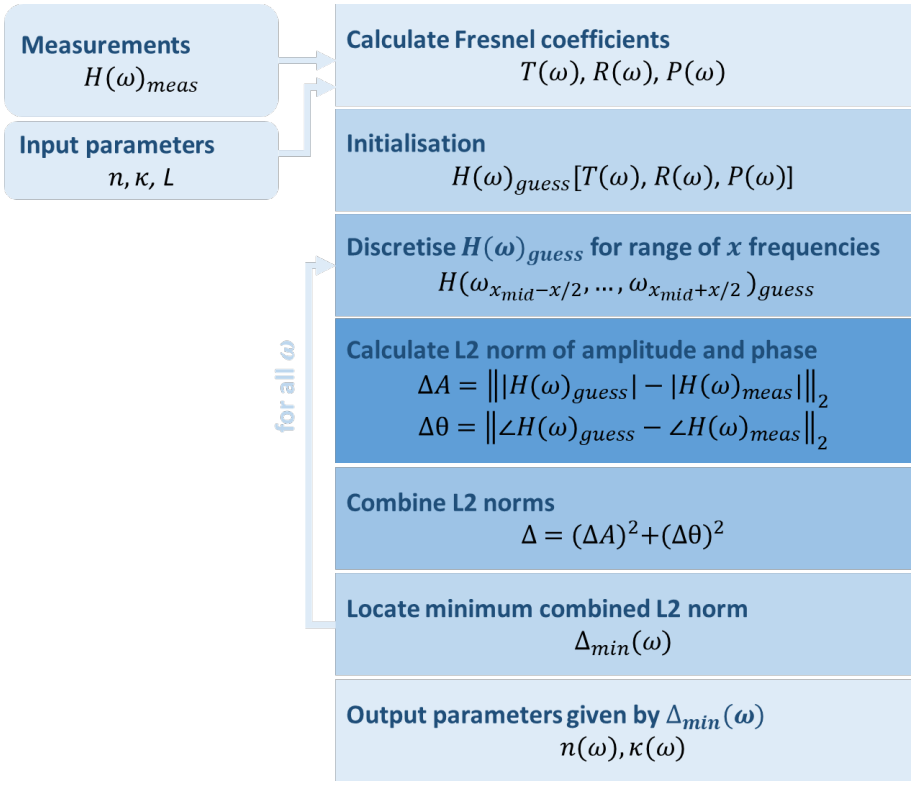

Figure 3.9: Flow diagram of the Fabry-Pérot dielectric extraction algorithm. Figure taken from [87].

electric properties, to demonstrate its success. Reflected temporal waveforms were simulated using the transient solver of CST Microwave Studio for normal incidence (i.e. $\theta_1 = \theta_2 = 0$, and $A_{wo,m} = 1$). The structure was designed to have dielectric properties comparable to the glass-backed HO bone (see sample configuration in the inset of Figure 3.8). The simulated and modelled transfer functions, pre- and post-algorithm are presented in Figure 3.10. One can observe low frequency oscillations attributed to the Fabry-Pérot reflections within the structure. The algorithm successfully models the reflections, providing good agreement between the measured and modelled transfer function. This enables the removal of these oscillating artefacts, which propagate through to the refractive index and extinction coefficient results. The right panel of Figure 3.10 presents the corrected results. Consistency with the simulation input refractive index and extinction coefficient demonstrates the successful

extraction of the correct dielectric properties.

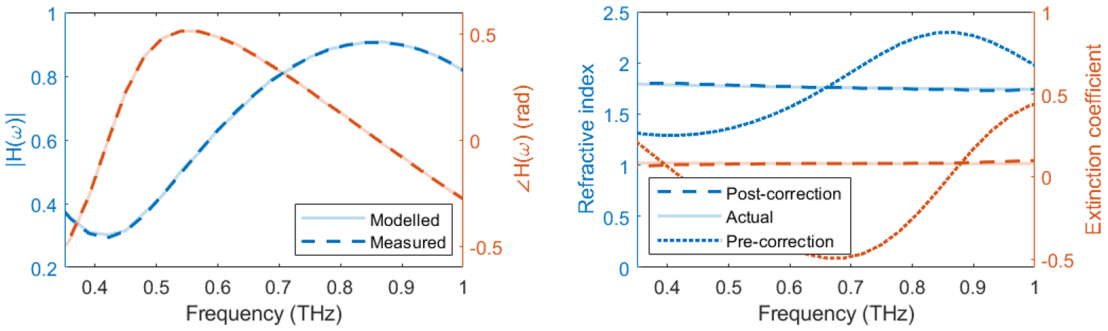

Figure 3.10: (Left) Amplitude and phase of the transfer function $H(\omega)$ for the structure presented in Figure 3.8, simulated using the transient solver of CST Microwave Studio. Layer 1 was modelled as air, while layers 2 and 3 were modelled as bone and glass, respectively. The dashed lines illustrate the measured transfer function, while the transparent lines illustrate the transfer function modelled using the Fabry-Pérot algorithm. (Right) Refractive index and extinction coefficient of the structure pre- and post-application of the Fabry-Pérot modelling algorithm, indicated by the dotted and dashed lines, respectively. The transparent lines illustrate the input dielectric properties in CST Microwave Studio [38]. Figure taken from [87].

Figure 3.11 presents the application of the algorithm to a single reflection measurement of the ∼100 µm thick HO bone sample (see sample configuration in the inset of Figure 3.8). Low frequency oscillations originating from the Fabry-Pérot reflections within the structure are evident in the dielectric properties pre-application. The algorithm successfully removes these artifacts through modelling the reflections and locating the minimum error, or L2 norm, calculated for estimated dielectric properties, as presented in Figure 3.12. Accurate extraction of the dielectric properties is achieved.

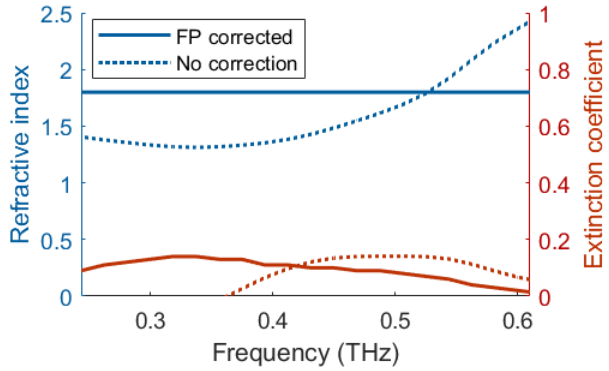

Figure 3.11: Refractive index and extinction coefficient of a ∼100 µm thick sample pre- and post-application of the Fabry-Pérot modelling algorithm. Figure taken from [87].

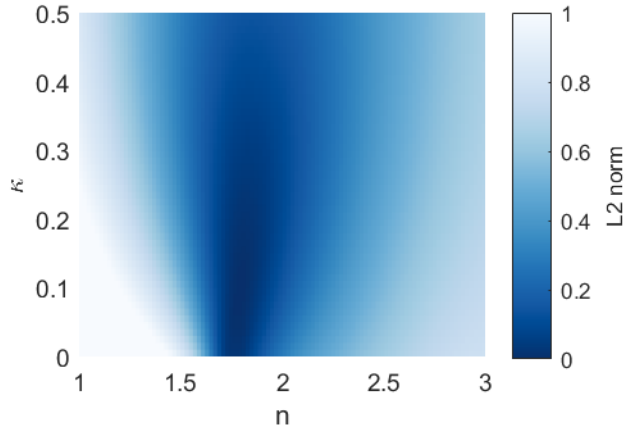

Figure 3.12: Calculated L2 norm as a function of estimated refractive index and extinction coefficient.

3.4 Hyperspectral dielectric imaging

3.4.1 Results and discussion

To demonstrate the hyperspectral dielectric imaging capability of the hybrid algorithm it is applied to reflection TDS images of the optically thin (∼100 µm) HO bone samples which exhibit an offset between the sample and reference planes. The measurements consist of

a reference measurement taken from a slide pixel, which sits further back from the bone (see the inset of Figure 3.8), inducing a phase offset, while the structure thickness results in unresolvable initial and subsequent reflections.

To better understand the composition of the bone material, spectral measurements of the constituent compounds of bone structures, including collagen and HA, were undertaken and presented in Figure 3.13. The responses reveal reasonably featureless dielectric properties in the probing frequency range for all compounds. The absence of spectral fingerprints in this regime means that identification of compounds relies entirely on broadband differences in the refractive index and extinction coefficient. It is worth noting that this is limited by changes in sample preparation factors such as sample hydration.

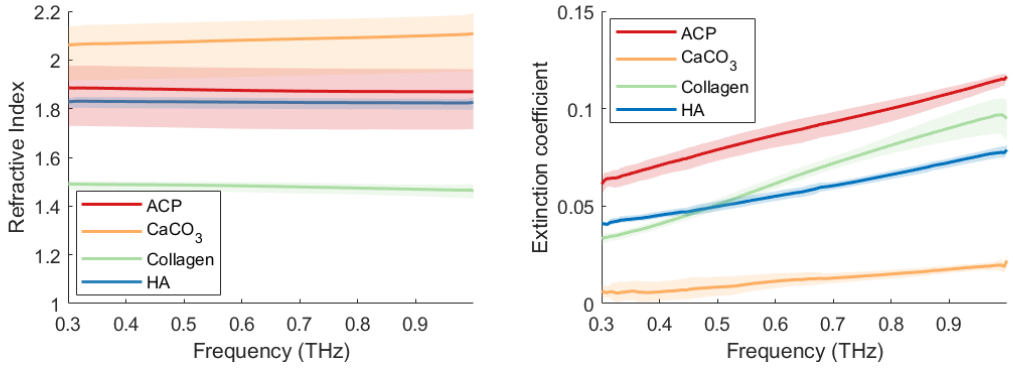

Figure 3.13: The refractive index and extinction coefficient of constituent compounds of bone structures: ACP, $CaCO_3$, collagen and HA, measured using terahertz transmission TDS. Figure taken from [87].

Figure 3.14 presents the imaged refractive index and extinction coefficient at 0.3 THz, 0.4 THz and 0.5 THz, respectively, pre- and post-application of the hybrid algorithm. The dielectric images pre-application exhibit unphysical and highly variable values as a function of frequency. This is consistent with observations of phase accumulation and Fabry-Pérot reflections presented in Figure 3.4 and Figure 3.11, respectively. After passing the images through the hybrid algorithm, one can observe fairly uniform dielectric properties across the

bone slice, with minimal frequency dependence. This is supported by the XRF image, which identifies the bulk of the sample as collagen (blue), with small islands of hydroxyapatite (HA), a form of calcium phosphate (yellow) (see Figure 3.1), and measurements of dielectric properties of the constituent compounds of bone structures, presented in Figure 3.13. From these spectral measurements, collagen is found to have n_{collagen} ∼1.5, with low frequency dependence, and κ_{collagen} ∼0.04 – 0.09, from 0.3 – 1 THz. The small deviation from the retrieved values of n_{bone} ∼1.8 and κ_{bone} ∼0.1 is attributed to an increased hydration level in the bone structures, to which terahertz is highly sensitive to.

The regions of HA are undetectable in the dielectric images due to field scattering at the edges of the structure and insufficient resolution of 0.5 mm. Increased resolution could be achieved through higher frequency illumination. Marginal improvement of resolution with excitation with higher frequency radiation is demonstrated in the dielectric images at 0.3 THz and 0.5 THz. Pushing towards higher frequencies is limited, however, due to the low SNR of the TDS system in use.

The output dielectric images demonstrate the success of the hybrid Kramers-Kronig Fabry-Pérot algorithm for biometric imaging and its ability to deal with complex sample configurations. This ability is essential for practical biological application with limited controllability. The free-standing sample set-up (i.e. not sandwiched between two windows, as commonly configured [97]) is a versatile configuration, which is far more practical for application in clinical environments. This configuration is, however, affected by surface roughness and subsequent scattering, an important consideration when dealing with structures of high roughness with feature dimensions comparable to the terahertz wavelength. Plane wave excitation and a linear EM material response should also be considered for application of the algorithm. The former assumption is important for excitation using TDS systems, where beam divergence is large, most significantly at low frequencies, and beam profiles deviates from typical Gaussian distributions [115].

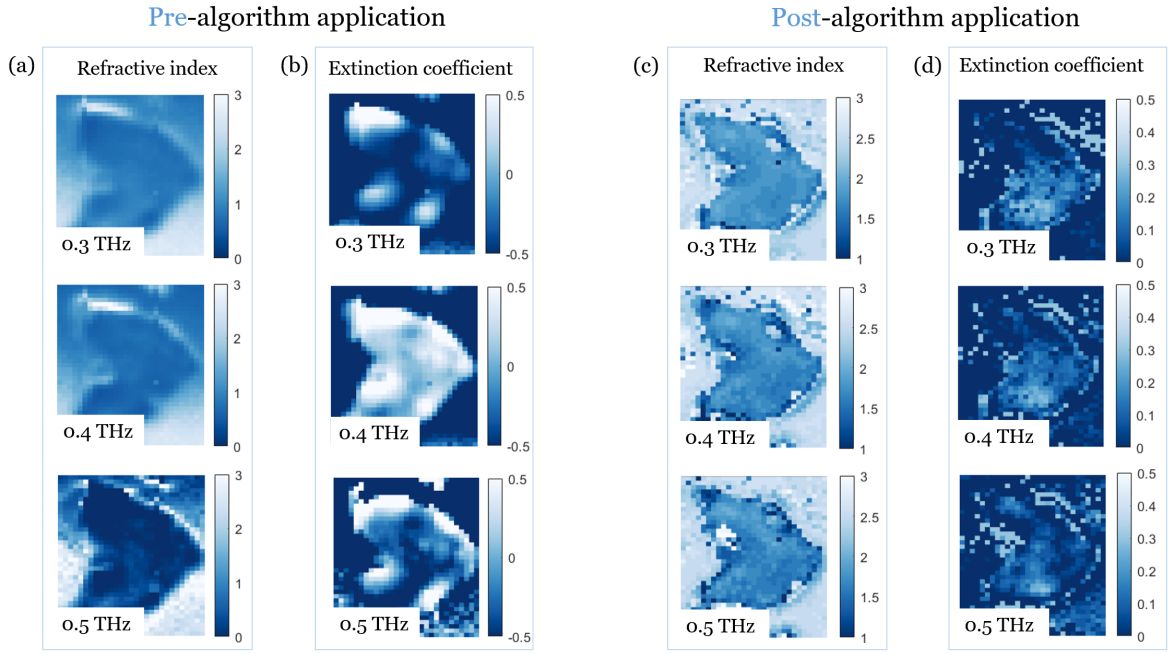

Figure 3.14: Images of the extracted (a,c) refractive index and (b,d) extinction coefficient values of the HO bone slice at 0.3 THz, 0.4 THz and 0.5 THz, pre- and post-application of the retrieval algorithm. Note the different limits of the colour bar. Figure taken from [87].

Application of this novel hybrid Kramers-Kronig and Fabry-Pérot based algorithm becomes highly valuable in the retrieval of biometric information of biological materials, where samples exhibit high terhertz absorption and sample placement and thickness are difficult to control. The causal basis of the Kramers-Kronig approach and lifted limitation of sample thickness attributed to the Fabry-Pérot approach grants great flexibility of measurements, and hence wide application to biological materials. In the following sections, the processing platform created by this algorithm is used to perform further investigations into the bone samples, including hydration mapping, for disease detection, and growth direction.

3.5 Temperature dependent imaging for hydration mapping

The molecular formation of a material, including molecular bonds, determine how it interacts with an EM field, and hence its dielectric properties. The formation of molecular structures changes with respect to temperature. Temperature dependent spectral features can be used to gain valuable insight into the composition of structures, particularly those with anisotropic distribution of water, as is often the case in biomedical systems.

Aided by high terahertz field-water interactions, modification in tissue hydration due to disease can therefore be monitored through temperature dependent terahertz spectroscopy. This study aims to take advantage of the sensitive dependence of molecular dynamics of water to environmental temperature, to monitor changes in the composition of tissue, with particular focus on bone, for prospective disease identification.

The hydration of the HO bones was studied through temperature dependent spectroscopic measurements using the time-domain terahertz spectrometer in reflection configuration, illustrated in Figure 3.2. The samples were heated from $\sim$18°C to 26°C through freezing the sample and bringing to room temperature. Sample temperature was monitored using an IR thermometer. Here, the dependence of the terahertz complex permittivity of HA and collagen [116], the two main constituent materials of bone, and the glass substrate with respect to temperature is negligible compared to water. This indicates that any temperature dependent dielectric changes observed are indeed due to the bone.

3.5.1 Results and discussion

Figure 3.15 presents the temporal response of the HO bone for increasing temperature. One can observe an increase in reflected peak-to-peak E-field amplitude and reduction in arrival time with increasing temperature. This is consistent with the behaviour of water at terahertz frequencies [117], whereby the refractive index and extinction coefficient increase as a function of temperature, attributed to formation and breakage of hydrogen bonds, translational and rotational motions of dipoles and structural rearrangement, which all occur at different energies [118]. Higher thermal energy, or kinetic energy of water results in longer relaxation times of the polar molecules, characterised by the time taken to align with the polarisation of the transmitting E-field. This results in both an increase in refractive index and extinction coefficient. The observable loss of high frequency components for lower temperature is arguably due to the reflection reduction (i.e. the refractive index contrast between air and bone decreases with temperature, resulting in a smaller Fresnel reflection coefficient) that causes high frequencies to fall below the noise level of the system.

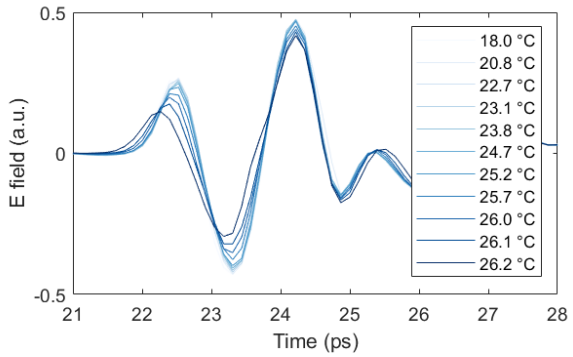

Figure 3.15: Reflected temporal response of the HO bone sample with increasing sample temperature. Figure taken from [SF1].

To extract the amplitude and phase of the reflected E-field, a Fourier transformation was applied to the temporal waveforms in Figure 3.15. Figure 3.16 presents the frequency dependent spectra, where the amplitude and phase are normalised to the amplitude and

phase of the lowest temperature measurement, respectively. This is consistent with the oscillations observed in Figure 3.11. One can observe an increase in both amplitude and phase with increasing temperature, consistent with the increase in dielectric properties observed from the temporal results. The notable variation in increase in both amplitude and phase are attributed to Fabry-Pérot reflections frequency oscillations in the frequency domain [87]. The removal of these artifacts was achieved through application of the hybrid Kramers-Kronig Fabry-Pérot modelling algorithm presented in section 3.4.

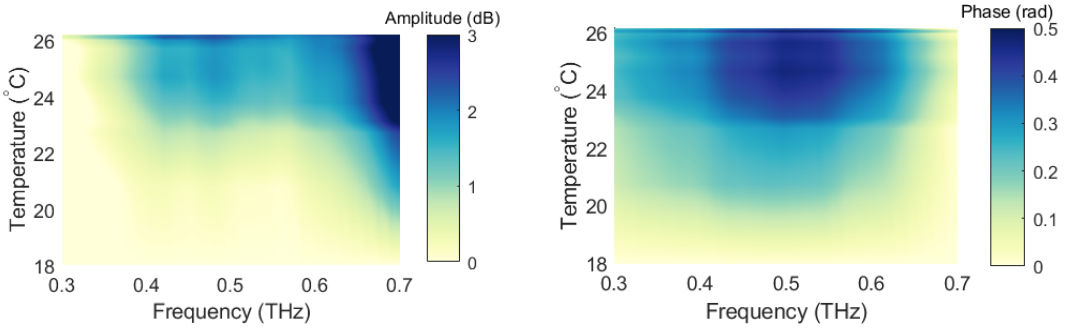

(a) (b)

Figure 3.16: (a) Amplitude and (b) phase spectra for the HO bone structure as a function of temperature pre-application of the Fabry-Peérot modelling algorithm. The amplitude and phase are normalised to the amplitude and phase of the lowest temperature measurement, respectively. Figure taken from [SF1].

To reveal the characteristic dielectric behaviour of water, exclusively, as a function of temperature, the TDS measurements were repeated in transmission configuration for deionised water within a temperature-controlled 500 µm thick cell. The complex permittivity was subsequently calculated for both the HO bone sample and free water, using the Fabry-Perot algorithm and Teralyzer (a material parameter extraction software by Menlo Systems), respectively. Figures 3.17 and 3.18 present the change in the frequency dependent real and imaginary parts of the permittivity as a function of temperature to reveal the water content, given by $\mathrm{Re}(\epsilon) = n^2 - \kappa^2$ and $\mathrm{Im}(\epsilon) = 2n\kappa$, respectively. The assumption that no

other compound has a significant temperature dependence was applied. Each spectrum is normalised by the spectrum of lowest temperature.

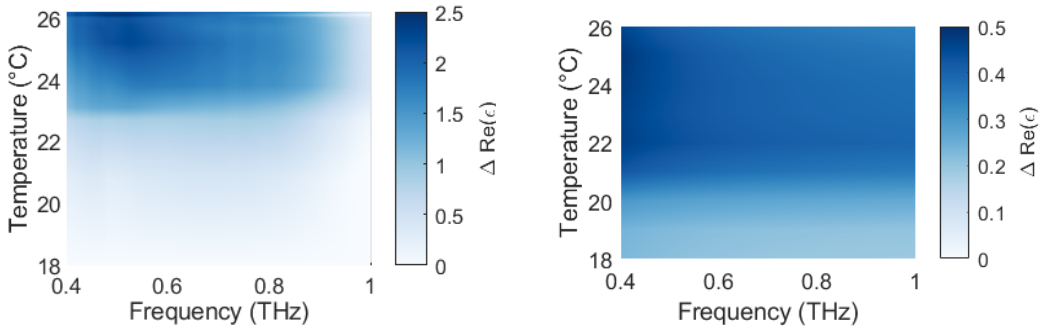

(a) (b)

Figure 3.17: Change in the real part of the permittivity of the HO bone (left) and water (right) as a function of frequency and temperature. Each spectrum is normalised by the spectrum of lowest temperature. Figure taken from [SF1].

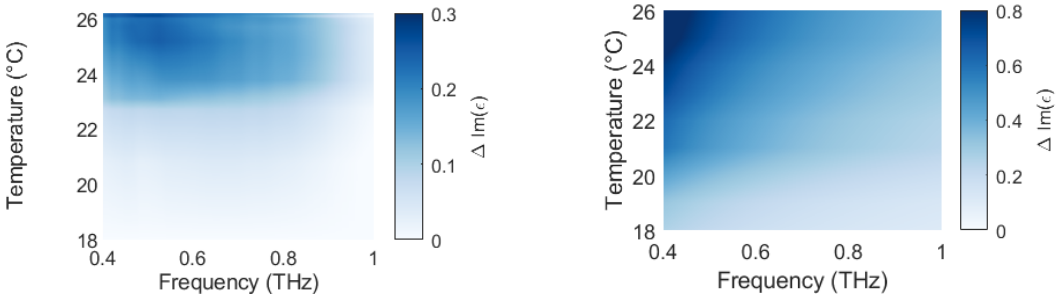

(a) (b)

Figure 3.18: Change in the imaginary part of the permittivity of the HO bone (left) and water (right) as a function of frequency and temperature. Each spectrum is normalised by the spectrum of lowest temperature. Figure taken from [SF1].

The figures illustrate an increase in both real and imaginary permittivity with temperature, both of which are more pronounced for lower frequencies. The consistency between the bone and water samples indicates the presence of water in the bone structure. The increase in permittivity with increasing temperature and decreasing frequency can be attributed to the

relaxation mechanisms of molecules that determine the permittivity of water, specifically the reorientational dynamics of dipole moments. This is characterised by the reorientation time of hydrogen-bond structures. Water exhibits two relaxation mechanisms modelled by Debye theory: slow and fast relaxation, occurring at ∼10 ps and sub-picosecond (THz) timescales, respectively. The slow relaxation time is highly dependent on temperature and is increasingly pronounced for lower frequencies [119]. This is further illustrated by Figures 3.19 and 3.20, which present the real and imaginary permittivity as a function of temperature, for fixed frequencies. The permittivity characterises a material's ability to permit the E-field and the loss of the field within the material. The difference between the change in the actual values of permittivity for bone and water are thought to be attributed to the difference in mobility of the water molecules in each sample [120]. In the bone structure, water is expected to exist as bound water, which is typically found in tissue molecular components. In the deionised water, however, the water exists as free water. The difference between the dynamics of the two results in a difference in the change of the dielectric properties with temperature. Further study of the temperature dependence of different water states must be carried out to characterise this.

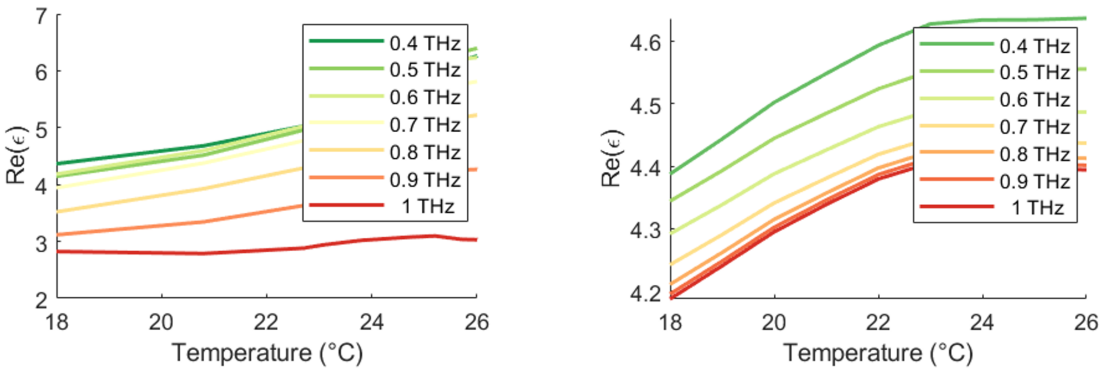

Figure 3.19: Real permittivity of the HO bone (left) and water (right) as a function of temperature, for fixed frequencies. Figure taken from [SF1].

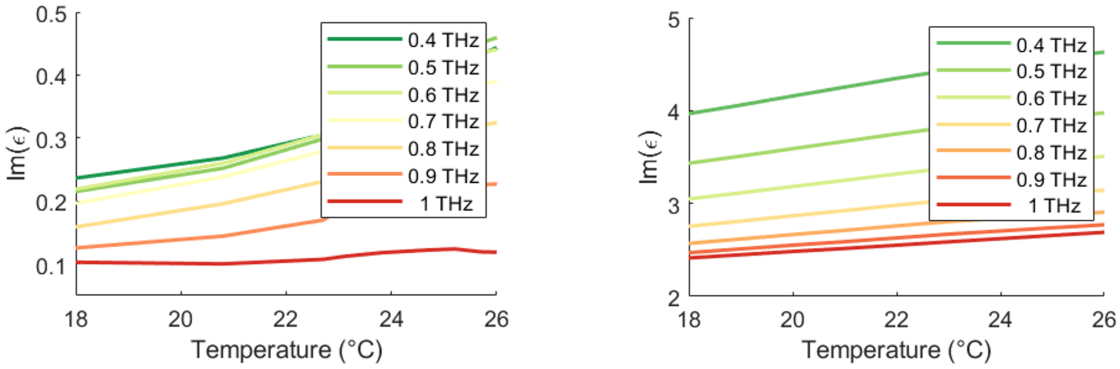

(a) (b)

Figure 3.20: Imaginary permittivity of the HO bone (left) and water (right) as a function of temperature, for fixed frequencies. Figure taken from [SF1].

3.5.2 Summary

Terahertz temperature dependent spectra have been taken to probe the hydration of HO bone samples. The observation of increasing permittivity with increasing temperature and decreasing frequency is identified as a signature of the presence of water. Future work aims to use this as a hydration mapping tool, for probing changes in tissue hydration, for prospective disease monitoring.

The ability to detect water provides great insight into biological system functionality, particularly in the development of disease. In this work, the high interaction of terahertz radiation with water, paired with the dependence of the dynamics of water molecules with varying temperature, has been utilised to monitor changes in the composition of bone tissue. Changes in the dielectric properties of HO bone samples and deionised free water were found to be comparable, showing great promise for the application of this technique as a hydration mapping tool for disease detection. The prevalence of water within biological systems means that this technique is open for application across a multitude of biological systems. Building upon this understanding of sensing biological systems, Chapter 4 scales

down from bulk sensing to the micrometer scale, addressing the mismatch between the wavelength of terahertz and biological cells through field enhancement.

3.6 Cross-polar imaging towards bone growth direction

Human tissue growth often occurs with specific geometries and preferential directions [121]. Terahertz has proved to be an invaluable tool in probing the morphology of biological structures, such as the helical structure of human sweat glands [122]. Given that the structures have resonances at terahertz frequencies, one can gain an insight into anisotropy and orientation of growth of different tissues. Here, the bone structures are investigated to unveil whether bone growth has a preferential direction.

The linear polarisation of the field produced by the TDS, characterised in Chapter 2, is utilised for cross-polar imaging of the bone samples. This involves imaging the bone samples with fixed polarisation, as before, and then re-imaging with orthogonal polarisation. Changes in the detected field between the two measurements indicate isotropy within the structure. Figure 3.21 presents the cross-polar images of the glass-backed HO bone. There is no observable difference for imaging with difference polarisation. This indicates that the is no preferential growth direction in the sample, that is detectable at terahertz frequencies.

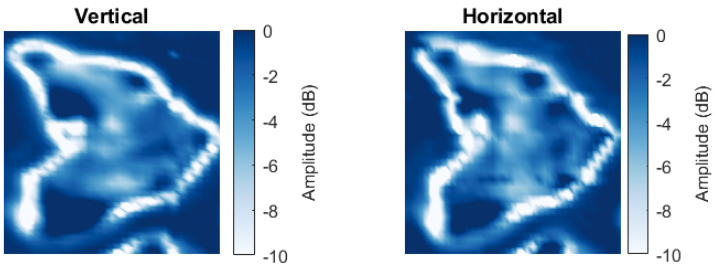

Figure 3.21: Reflected E-field amplitude at 0.5 THz for the HO bone sample, for incident radiation with horizontal and vertical polarisation.

3.7 Chapter conclusion

This chapter has addressed experimental challenges afflicting the TDS community through the development of a hybrid Kramers-Kronig Fabry-Pérot modelling algorithm. Its success is evident through application to HO bone samples, extending to hydration mapping and investigations of bone growth direction. The unique combination of the Kramers-Kronig and Fabry-Pérot modelling offers great versatility for application to complex samples, while the reduced computational complexity over existing modelling approaches allows for easier implementation.

Future work will involve adapting these algorithms for application to complex multilayer biological samples. This will make them significantly valuable to the Birmingham group, and indeed the wider community, for dielectric retrieval, while making them more practical for prospective use in a clinical environment.

3.8 Appendices

3.8.1 Appendix A: Preparation of bone samples

Heterotopic ossification (HO) samples, supplied by Cong Sui, were obtained from consented patients undergoing routine excision surgery at University Hospital Birmingham in United Kingdom. The HO samples were frozen immediately after excision surgery and stored at -80 °C. Samples were thawed at ambient temperature for 1 h before use, and then embedded in optimal cutting temperature compound (VWR Chemicals, Leuven, Belgium) under vacuum (20 kPa) using a Struers CitoVac (Struers Ltd, Rotheram, United Kingdom). The embedded samples were equilibrated to -18 °C after refreezing at -80 °C overnight, and sectioned into 100 µm sample slices using a Leica microtome with a tungsten carbide blade. The obtained sample slices were mounted on a glass microscope slide and dried in ambient conditions for 72 h. Tissue transfer and handling was conducted under approval of the National Research Ethics Service (15/NW/0079) and in accordance with the Human Tissue Act 2004.

3.8.2 Appendix B: TDS imaging method

The samples were characterized using an all fiber-coupled THz time-domain spectrometer TERA K15 from Menlo Systems with lock-in detection. The time-constant was set to 300 µs. The temporal length of the waveforms was 52 ps, providing a spectral resolution of 15 GHz. A standard reflection configuration was setup with a Si beam-splitter. The field was normally incident with accuracy of 0.3 deg and focused on the sample using a TPX35 lens with 35 mm effective focal length. To generate the images, a single pixel imaging technique was used, through translation of the sample fixed to an xy-translation stage, with steps of 0.5 mm.

3.8.3 Appendix C: Laser profiling method

The FV system employed in the experiments is an Alicona InfiniteFocus G5 system. It is equipped with x5, x10, x20 and x50 objective lenses that provide lateral resolution of 1.76 µm, 0.88 µm, 0.44 µm and 0.18 µm and vertical resolution of 0.41 µm, 0.1 µm, 0.05 µm and 0.02 µm, respectively. The measurement repeatability of the system is 0.12 µm, 0.03 µm, 0.01 µm, 0.003 µm and 0.001 µm for x5, x10, x20, x50 and x100 objective lenses, respectively.

Chapter Four

Surface Waves for Enhanced Sensing

4.1 Introduction to surface waves

Terahertz EM fields promise great potential for sensing of biological materials on the super-micron-scale (of the order of tens to hundreds of microns): cells, bacteria, micro-organisms and some organelles [123]. To unlock access to the super-microscopic biological world from a terahertz perspective, the disparity between the wavelength of terahertz EM waves, of the order of hundreds of micrometers, and super-micron dimensions of biological materials must be addressed. Dimension mismatches result in low field-matter interactions, and hence low sensing capabilities of terahertz fields. The local field enhancement, and hence high sensitivity to dielectric environments of evanescent fields, coupled with their subwavelength modal size [124], present a promising solution for enhanced terahertz sensing. Inspiration for evanescent field illumination has been taken from the optical regime — specifically, surface plasmons.

Surface plasmons are localised surface waves that exist at the interface between two materials with opposite permittivities, for example, a metal-dielectric interface. At optical frequencies, an EM wave can interact with the plasma of electrons in a metal surface,

exciting oscillations which propagate along the interface. The evanescent field produced is highly localised and confined to the interface, receiving large amounts of attention for their vast range of applications, from scanning near-field optical microscopy (SNOM) probes [125] to nanoscopic waveguides [126]. To utilise these interactions in the terahertz regime, however, requires more complex engineering. Surface plasmons cannot exist in metals at low frequencies such as terahertz. Instead, artificial surface plasmons — spoof surface plasmons (SSP) — can be created through metamaterial design, often corrugated metallic structures. Metamaterials are materials engineered to manipulate EM waves, by absorption, control of propagation direction and enhancement of EM fields. They are designed in such a way as to mimic the E-field distribution and dispersion behaviour of surface plasmons [32, 33]. The tunability of the design dimensions allows control over the frequency of the spoof surface plasmon, or surface wave. This is invaluable in sensing, where molecular interactions occur at different frequencies, and the ability to control the probing frequency opens up terahertz sensing to a vast range of applications.

This chapter initially focuses on the development and behaviour of surface waves as leaky waves, classified in Table 4.1, in the context of a phenomenon known as extraordinary transmission (ET). This is followed by an investigation of different geometric designs to generate surface waves of tunable properties. Fabrication quality plays a fundamental role in surface wave propagation. In metamaterials, while the importance of this is understood in the literature [127, 128], characterisation of this effect is limited. Large focus of this section is on the study of fabrication technique and its attenuation of the surface wave. In a final effort to push instrument sensitivity, investigation of enhancing coupling efficiencies of terahertz radiation to surface wave modes is investigated, with inspiration taken from the microwave regime for fabrication of highly efficient coupling structures.

Table 4.1: Surface wave classification for time dependence $e^{i\omega t}$. β_r and α are in-plane wavevectors and p and α_t are the out of plane wavevectors, where the E-field is expressed as $E(x,z) = e^{-ipx-i\beta z}$ (z is in-plane and x is out of plane), $p^2 + \beta_r^2 = k^2$, $p = p_r - i\alpha_t$ and $\beta = \beta_r - i\alpha$. Blue and yellow represent proper and improper waves, respectively. Y/N/M denote yes/no/maybe and indicate whether the complex wave is considered a spoof surface plasmon in the literature.

Wave type	β_r	α	p_r	α_t	SSP
Fast wave (waveguide modes)	+	0	+	0	N
Backward leaky wave	+	−	+	+	Y
Trapped surface wave	+	0	0	+	M
Zenneck wave	+	+	−	+	N
Plane-wave	+	0	−	0	N
Untrapped surface wave	+	0	0	−	Y
Forward leaky wave	+	+	+	−	Y

4.2 Surface waves for Extraordinary Transmission

This section is based on the following articles:

S. Freer, *et al.*, 'Revealing the underlying mechanisms behind TE extraordinary THz transmission,' *Photonics Research*, 2020 [SF3].

S. Freer, *et al.*, 'Study of Leaky Waves Responsible for Terahertz TE Extroardinary Transmission,' *12th UK-Europe-China Workshop on Millimeter Waves and Terahertz Technologies (UCMMT)*, 2019 [129].

In the late 1990s Bethe's aperture theory faced contradiction when Betzig *et al.* observed enhanced transmission through subwavelength apertures beyond previous observations [130, 131]. This remarkable effect was termed extraordinary optical transmission (ET). The underlying physics of the phenomenon drew large interest in the optics community and was initially attributed to surface plasmons supported at an air-metal interface and diffraction modes by Ebbesen *et al.* [132, 133, 134]. These are transverse magnetic (TM) (p-polarised) modes. Observations of TM ET at microwave and terahertz frequencies demanded further explanation [135, 137, 136, 138], since metals behave as perfect electric conductors (PECs) in this regime, and hence surface plasmons do not exist [139]. The effect at these frequencies was instead found to stem from diffraction [140] - the periodic perturbations of structures enabled them to support surface modes, termed leaky-type modes [137], sometimes referred to as grating or lattice modes [141]. The study of leaky modes had already been developed by Ulrich [142] in the context of metal meshes in the far infrared as the mechanism responsible for strong peaks observed in the transmittance. The emergence of these peaks was related to the resonant Wood's anomalies of reflection gratings [142, 143, 144], resulting from the interference of the direct and leakage beams. Despite large focus on TM ET, leaky modes can exist as both TM and transverse electric (TE) (s-polarised) waves, opening up the possibility for TE ET. This phenomenon was first theorised by Vitaliy

Lomakin [143, 145].

This section focuses on dielectric-backed subwavelength slit arrays which exhibit ET attributed to grounded dielectric slab modes of leaky-type [139]. Grounded dielectric slab modes are surface waves which can be excited along a grounded dielectric slab (see Figure 4.1). They exhibit a characteristic exponential decay of field away from the dielectric surface, into the medium, and remain tightly confined to the interface. Classically, there exists a momentum mismatch between free space and grounded dielectric slab modes, and hence free space energy cannot couple to the structure. The introduction of periodic perturbations (e.g. slits), however, transforms the mode in the structure into an infinite number of space harmonics, termed Floquet modes [146] (see Figure 4.2). Providing one of the Floquet modes falls within the fast-wave region (i.e. radiation light cone), the mode can be described as leaky, enabling coupling to free space (see Appendix B). This is the underlying phenomenon from which ET is born.

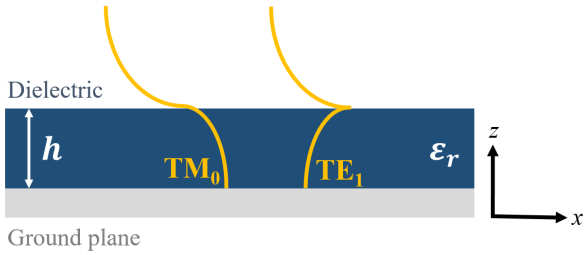

Figure 4.1: Geometry of a grounded dielectric slab: dielectric (blue) of thickness h and dielectric constant ϵ_r with metallic backing (grey). The yellow lines illustrate the absolute value of the E-field for the TM_0 and TE_1 modes, as a function of z. The structure is invariant along y and infinite along x.

The narrowband nature of ET, alongside the high field confinement, mean that the mechanism can be utilised for applications such as quasi-optical filtering devices [147, 148, 149] and sensing [43]. For any application, a rigorous understanding of the underlying mechanism is necessary, including all possible practical nuances, such as the effect of illumination

(Gaussian or plane-wave, etc.). Research has been largely focused on TM leaky-modes after initial observations of ET stemming from p-polarised plasmon modes [147, 150]. TE ET was later measured accidentally [151], however literature on TE transmission [152] remains far more sparse than for TM, despite exhibiting some advantages over TM ET in applications such as sensing, where they provide higher sensitivities [43].

In this section, a rigorous study of TE ET is undertaken through quasi-optical terahertz time-domain measurements, full wave simulations and method of moments analysis, in order to gain a greater understanding of the somewhat overlooked TE phenomenon. This work provides the foundation for the utilisation of TE ET in prospective applications such as high-performance THz components and sensing systems. To support the campaign of measurement and the understanding of results, the following section reviews the basic concepts of grounded dielectric slab modes.

4.2.1 Grounded dielectric slab modes

A grounded dielectric slab supports both TM and TE modes. A fundamental difference between TM and TE grounded dielectric slab modes is that at least one TM mode can be supported by a ground plane without a dielectric, whereas a dielectric of defined thickness is required for at least one TE mode to be supported [153, 154, 155] (see Figure 4.1). This stems from a cutoff frequency, below which the structure cannot support a mode. This can be determined from solutions of the transcendental equations which can be derived from the wave equations in the dielectric and air regions (see Appendix A). It is worth noting that the dielectric is assumed to be lossless - a reasonable assumption since a low loss dielectric (polypropylene) is used in the experiments. For the TM modes, the transcendental equations are found to be

$$k_c^2 + (qh)^2 = (\epsilon_r - 1)(k_0 h)^2, \tag{4.1}$$

$$k_c h \tan(k_c h) = \epsilon_r q h, \tag{4.2}$$

where k_c and q are the dielectric and free space cutoff wavenumbers, h is the dielectric thickness and ϵ_r is the dielectric constant (see Figure 4.1). By solving these numerically (see Appendix A), one can extract the cutoff frequency of the TM_n mode as

$$f_c = \frac{nc}{2h\sqrt{\epsilon_r - 1}},\ n = 0, 1, 2, ..., \tag{4.3}$$

where n is the mode number and c is the speed of light in vacuum. For $n = 0$ the cutoff frequency is zero, and hence the TM_0 mode can propagate without a dielectric. This dielectric free case is equivalent to a plane wave propagating along the ground plane or incident at a grazing angle.

Similarly, the TE transcendental equations are found to be

$$k_c^2 + (qh)^2 = (\epsilon_r - 1)k_0^2, \tag{4.4}$$

$$-k_c h \cot(k_c h) = qh, \tag{4.5}$$

with cutoff frequency of the TE_n mode

$$f_c = \frac{(2n-1)c}{4h\sqrt{\epsilon_r - 1}},\ n = 1, 2, 3, ..., \tag{4.6}$$

from which it can be determined that the first propagating mode TE_1 has a non-zero cutoff frequency. The TM and TE transcendental equations are graphically presented in Appendix A (Figure 4.29) for a dielectric slab with ϵ_r= 2.25.

The solutions to both the TM and TE transcendental equations are presented as dispersion curves in Figure 4.2, where the shaded regions illustrate the cutoff regions for the TM_0, TE_1 and TM_1 modes. Here, the low thickness regime is studied, probing the development of the TE_1 mode with increasing dielectric thickness (labelled in Figure 4.2). The introduction of periodic perturbations (with lattice period 0.6 mm) for the TE_1 grounded dielectric slab mode is presented in the right panel of Figure 4.2. One can observe the transformation of the TE_1 mode into the Floquet modes, as previously described.

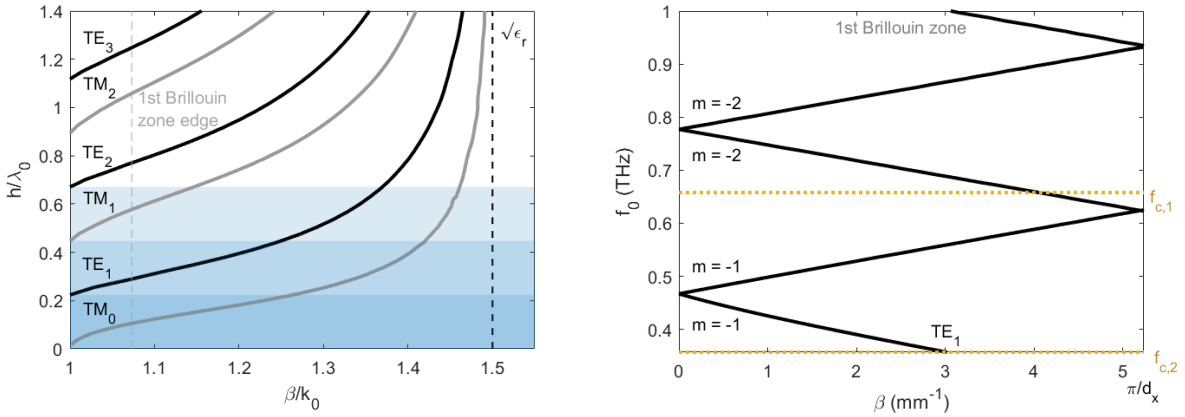

Figure 4.2: (Left) Dispersion relations of the TM and TE modes supported by a grounded dielectric slab with $\epsilon_r = 2.25$. λ_0 and k_0 are the free space wavelength and wavenumber, respectively, and $\beta = \sqrt{q^2 + k_0^2}$ is the propagation constant along x. The shaded regions illustrate the cutoff regions for the TE_1, TM_1, and TE_2 modes for a dielectric thickness $h_2 = 188$ µm. (Right) Dispersion relation of the TE_1 mode in the first Brillouin zone with periodic patterning of the ground plane. The zone edge is defined by the periodicity: $\beta = \pi/d_x$. The yellow lines indicate the cutoff frequencies f_c for the structures experimentally measured in section 4.2.2, where $h_1 = 102$ µm, $h_2 = 188$ µm and $d_x = 600$ µm. The space harmonics are labelled accordingly (illustrated in Appendix B, Figure 4.30).

4.2.2 Anomalous TE Extraordinary Transmission

The basic structure under investigation is an aluminium (Al) truncated subwavelength slit array with slit width $w = 0.22$ mm, lattice period $d_x = 0.6$ mm, slit length 70 mm and number of slits n (see Figure 4.3). The slit width and lattice period are designed such that the ET frequency is approximately at the dynamic range peak of the TDS system, around 0.5 THz (see Figure 2.13). The slit length was designed to be significantly larger than the excitation area, enabling the sample to behave as a 2D structure (i.e. invariant along y) and avoiding scattering at the edges of the slit. The metallic array was patterned onto polypropylene (PP) ($\epsilon_r = 2.25$) using contact photolithography [156, 157, 158], performed

by Sergei A. Kuznetsov, Novosibirsk State University. In order to characterise the behaviour of the leaky mode and the development of the grounded dielectric slab mode, the structures have varying number of slits (n = 1, 3, 7, 15, 30 and 107) and dielectric thicknesses (h = 102 µm and 188 µm), corresponding to the horizontal lines in Figure 4.2.

Understanding the influence of quasi-optics on the excitation of modes is fundamental for effective use in applications. An ideal collimated beam has an incident wavevector perpendicular to the structure surface. A leaky wave in a simple periodic structure cannot have a wavevector normal to the surface. Hence, a focused illumination will have higher coupling efficiency to the leaky mode. In reality, the incident field is not perfectly collimated, as revealed in Chapter 2, and thus some coupling will occur. To study this, both collimated and focused illuminations are used in this chapter.

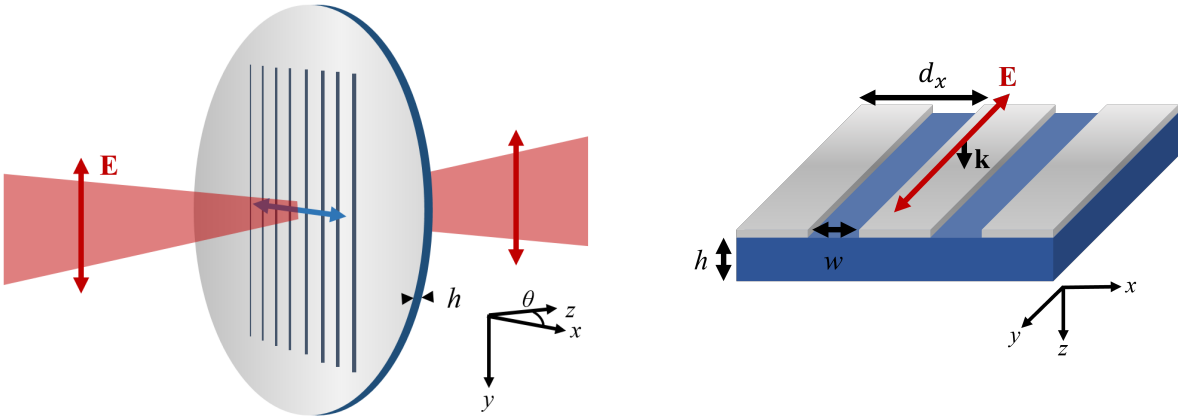

Figure 4.3: Schematic of the dielectric backed aluminium subwavelength slit array with slit width w = 0.22 mm, lattice period d_x = 0.6 mm and slit length 70 mm. The dielectric is polypropylene (PP) (ϵ_r = 2.25), with thicknesses of h 102 µm and 188 µm for the two structures. The structure is illuminated by a focused Gaussian beam with propagation along z and polarisation parallel to the slits, illustrated by the red arrow. The propagation of the leaky waves along the slits is illustrated by the blue arrows.

Normal Transmission and ET Saturation

Experiment: A common method of probing the behaviour of the leaky waves in both TM ET [34, 158, 159, 160] and TE ET [154, 161] is to measure transmission as a function of number of slits. This is effective in providing insight into the propagation of the waves along the structure. Additionally, as discussed in section 4.2.1, it is necessary for the structure to have a dielectric thickness above a threshold for the structure to support at least one grounded dielectric slab mode. This threshold thickness can be determined from Eq. 4.6 and was calculated to be 150 µm for the structures under investigation. Hence, the development of the mode can be studied through measuring samples with dielectric thicknesses below and above this threshold. In this study, transmission through structures with increasing number of slits and dielectric thicknesses above and below threshold are measured using a TDS system for normal incidence and detection (see Appendix D).

Spectra were obtained from the Fourier transformation of the time-domain response measurements and presented in Figure 4.4. The spectrum in Figure 4.4 (b) for the above threshold dielectric thickness and 107 slits has a peak in transmission followed by a dip, associated with the first Rayleigh-Wood's anomaly [152, 162] at ~ 0.47 THz, also known as the open stopband in leaky wave formalism [162]. This dip is suppressed in the spectra of the structure with dielectric thickness below threshold (Figure 4.4 (a)) [143, 145, 163, 164, 165], alongside a reduction in transmission. This provides some insight into the development of the TE_1 mode. Below threshold thickness, the mode is in cutoff (i.e. evanescent in the direction of propagation). As the dielectric thickness is increased above threshold, the structure is able to support grounded dielectric slab space harmonics and hence saturated ET is observed.

The transmission of energy through the structure is assumed to be through two channels: direct transmission through the slits and energy transfer mediated by the leaky grounded dielectric slab mode. With increasing number of slits (from 1 to 15) there is an

increase in direct transmission across all frequencies attributed to the array area being larger than the beam area. This transmission saturates at 15 slits, when the array area is equal to the illumination area. The enhanced transmission at ∼0.4-0.5 THz further increases beyond 15 slits, attributed to the $m = -1$ space harmonic of the TE_1 grounded dielectric slab mode (see Appendix B), as later identified. The transmission above 0 dB for $n = 107$ in Figure 4.4 (b) is due to collimation at broadside, a result of the contribution of both the leaky wave and direct transmission. This effect has previously been observed for TM ET [34] and will undergo further analysis using full-wave simulations of the truncated structures.

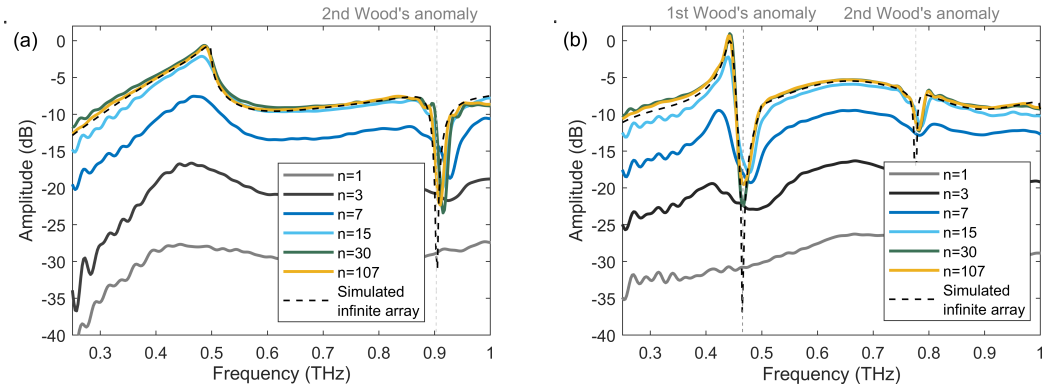

Figure 4.4: Normal transmission spectra for substrate-thin (a) and -thick (b) samples with $n = 1$, 3, 7, 15, 30 and 107 number of slits, measured under collimated illumination. For comparison, the black dashed lines illustrate the spectra simulated using CST Microwave Studio using unit cell boundary conditions and Floquet ports. The grey dashed line indicate the emergence of the Wood's anomalies. Figure taken from [129].

To further investigate the effect of the leaky wave mechanism on ET, independent of illumination beam size, ET amplitude is recorded as a function of array length (nd_x), normalised by the illumination beam diameter ($2\omega_x$) (see Figure 4.5). The beam waist was measured as ∼7.8 mm and ∼3.0 mm for collimated and focused illumination configurations (see Appendix D). From Figure 4.5, one can observe that saturation in transmission is achieved for array lengths larger than the beam diameter ($n \sim 30$), for both dielectric

thicknesses. This corresponds to $nd_x/2\omega_x \sim 6$, indicating that for saturation in transmission to be achieved, the leaky wave requires a large enough number of corrugations to propagate along, this being larger than $2\omega_x$. Additionally, comparing Figure 4.5 (a) and (b), it is evident that a higher saturation amplitude is reached for the substrate-thick structure, revealing the development of the mode.

One can observe faster saturation for the collimated configuration for both substrate thicknesses. This is attributed to the coupling efficiency of the incident field to the grounded dielectric slab leaky mode. An ideal collimated beam has an incident wavevector perpendicular to the structure surface. A leaky wave in a simple periodic structure cannot have a wavevector normal to the surface. This is known as the open stopband condition. Hence, a collimated incident field will favour coupling to the free space wave and take the direct transmission channel.

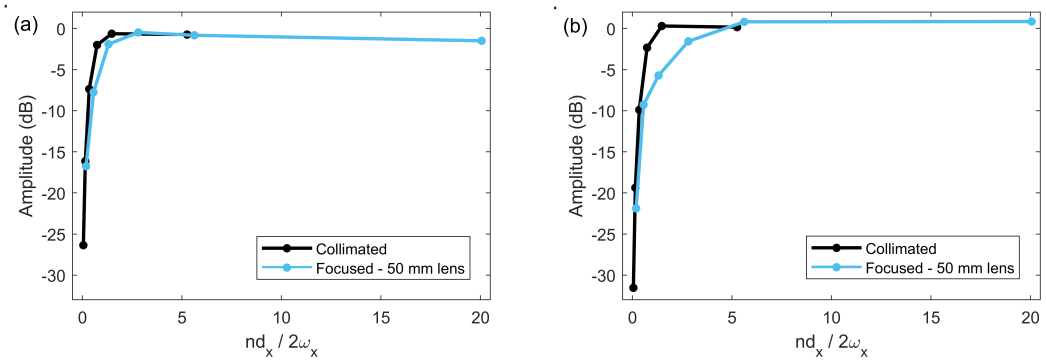

Figure 4.5: Transmission amplitude extracted at ET frequencies of 0.48 THz for the substrate-thin structures (a) and 0.44 THz for the substrate-thick structures (b), as a function of array length (nd_x), normalised by the illumination beam diameter ($2\omega_x$). Results from both collimated and focused configurations are presented. Figure taken from [129].

Simulations: To support the experimental study of the development of the grounded dielectric slab mode and propagation of the leaky waves, full-wave simulation of substrate-

thin and -thick structures (h = 102 µm and 188 µm) with 7 and 107 slits are presented in this subsection. The simulations were performed in the transient solver of CST Microwave Studio with Gaussian beam illumination. Figure 4.6 presents the E-field in the xz-plane. The development of the $m = -1$ mode is evident through comparison of Figure 4.6 (a) and (c). One can observe an increased coupling of energy to the $m = -1$ space harmonic for the structure with dielectric thickness exceeding the threshold, resulting in higher ET. Additionally, through comparison of Figure 4.6 (b) and (c) for which the mode is fully developed, an increase in coupling efficiency to the leaky grounded dielectric slab mode can be observed for the structure with larger number of slits. For the structure with 7 slits, beyond the truncation of the corrugations (indicated by the dashed line), the field is highly confined to the structure. Due to the lack of periodicity, the energy travels as a guided (non-leaky) grounded dielectric slab wave, remaining confined to the structure and hence not contributing to the ET. For the structure with 107 slits, however, the field decays along the structure. The periodicity transforms the grounded dielectric slab mode into a leaky wave, and hence the energy can recouple to free space as it propagates along the structure, contributing to ET.

These findings are supported by the simulated absolute E-field presented in Figure 4.7. Figure 4.7 (a) shows the E-field along thin- and thick-substrate structures with 107 slits, while (b) shows the E-field along substrate-thick structures with increasing number of slits. From Figure 4.7 (a), there is a significant increase in coupling of energy to the leaky grounded dielectric slab mode for the substrate-thick structure, attributed to the fully-developed leaky mode. The energy travels along the structure as a leaky wave, contributing to the ET. Additionally, the energy decays before the end of the periodic region, reradiating the energy associated with the leaky mode. From Figure 4.7 (b) it is evident that for structures with less slits, less energy couples to the leaky mode, instead travelling along the structure as a slow, non-leaky wave. The small reduction in field beyond the truncation of the slit region

is a result of absorption by the dielectric.

It is worth noting that the rate of field decay along the array is different for each structure, the slope being determined by the leakage constant of the surface mode. Simulations show that the attenuation constant, including both leakage and ohmic and dielectric absorption, is 0.84 mm^{-1} and 0.24 mm^{-1} for the thick- and thin-substrate structures, respectively. The lower attenuation constant for the thick-substrate structure indicates that the energy couples efficiently to the fully developed mode. The thin-substrate structure, however, does not fully support a propagating mode. The energy instead couples to a pseudo-mode which leaks energy more rapidly.

4.2.3 Temporal dependence of transmission

Temporal analysis of transmission provides greater insight into the behaviour of the underlying leaky wave mechanism responsible for ET. The propagation of the leaky wave can be studied through time-resolved measurements. Propagation of energy along the array results in a delay in transmission and hence delayed detection of the field. Here, spectrograms have been obtained through short-time Fourier transformation of waveforms following transmission through each structure. Figure 4.8 (a) presents normalised spectrograms for a substrate-thin structure with 7 slits and substrate-thick samples with 7 and 107 slits. Direct transmission through the slits can be observed at $\sim$25 ps. Beyond this, there is a delayed emission of energy at $\sim$0.45 THz attributed to the leaky mode. The energy propagates along the structure for some time before recoupling to free space to be detected. The maximum time delay of the leaky wave contribution is dependent on two factors: the coupling efficiency to the $m = -1$ mode and the array length. For the 7 slit structure, the development of the mode is evident through longer ringing of energy as the dielectric thickness is increased above cutoff. This indicates that more energy couples to the mode, and hence can travel along the

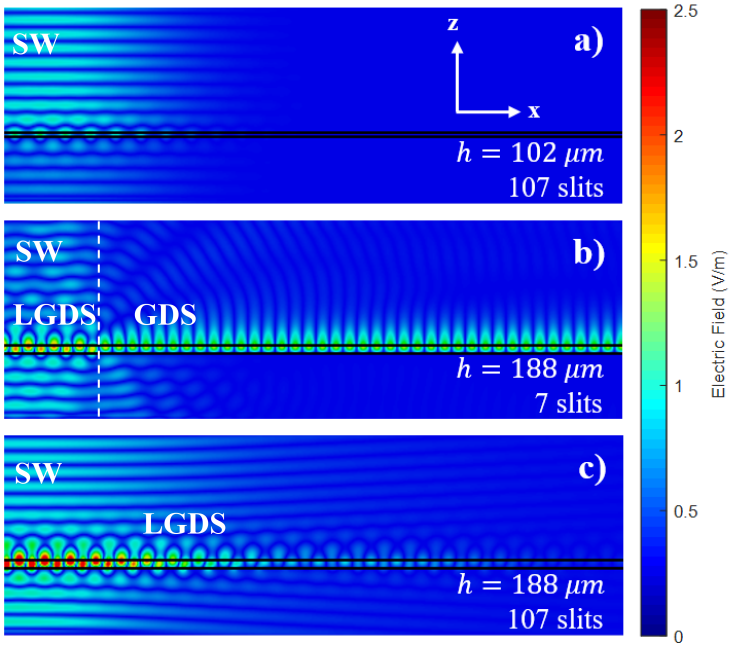

Figure 4.6: Simulated absolute value of the E-field in the xz-plane, calculated using the transient solver of CST Microwave Studio. The fields are calculated at the ET frequency 0.48 THz for the substrate-thin structure (a) and 0.44 THz for the substrate-thick structure (b,c), for 7 and 107 slits. A Gaussian source is used with direction of propagation along the z-axis and polarisation along the y-axis. The truncation of the 7 slit region is indicated by the dashed line. The space waves, $m = -1$ confined grounded dielectric slab (GDS) waves and $m = -1$ leaky grounded dielectric slab (LGDS) waves are labelled, with the LGDS wave only present in the periodic region of the structures. Figure taken from [SF3].

structure for longer before being reradiated. The longest ringing of energy, however, is for the substrate-thick structure with 107 slits. To study this further, the time for 1/e of the signal to decay has been obtained for each sample at the appropriate ET frequency (see Figure 4.9). As the number of slits is increased, the leaky wave explores a larger number of periods, and hence energy is retained in the system for longer. Additionally, all the energy associated with the leaky mode is reradiated before reaching the non-perforated region, enhancing ET.

To support these temporal findings, simulations were carried out in CST Microwave

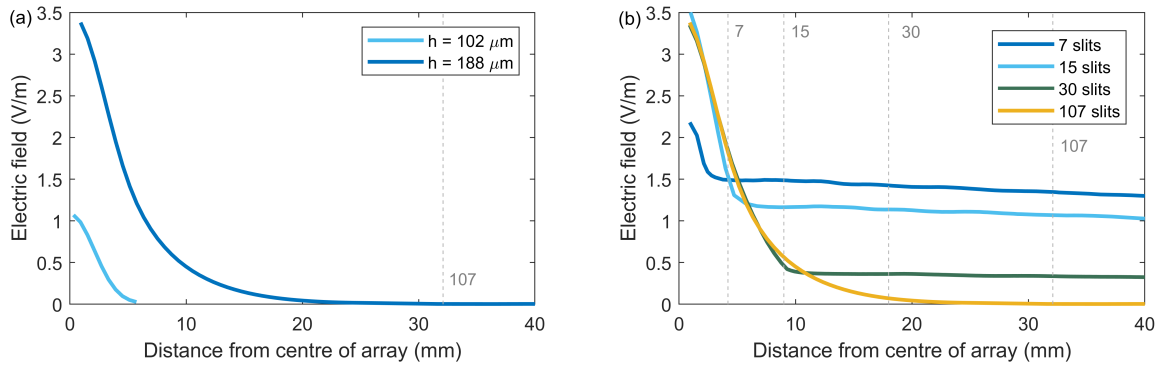

Figure 4.7: Simulated absolute E-field along one half of the array for (a) structures with dielectric thicknesses above and below threshold with 107 slits and (b) structures with increasing number of slits with dielectric thickness above threshold. The fields were calculated using CST Microwave Studio at ET frequencies of 0.48 THz and 0.44 THz for h is 102 µm and 188 µm, respectively. The incident beam radius is 1.5 mm. The dashed lines indicate the truncation of the slit regions from the centre of the array.

Studio for the substrate-thick structure with 107 slits using Gaussian beam excitation. The spectrogram presented in Figure 4.8 (b) was obtained through short-time Fourier transformation and normalised for comparison. Figure 4.8 (c) presents a comparison of the temporal decay of the field at the ET frequency 0.44 THz, showing fairly good agreement between experimental and simulated results. The symmetric-like Gaussian temporal pulse arriving at 20 ps is the direct transmission of the incident Gaussian field. The shoulder arriving at ∼30 ps present in both the experiment and simulation results is the leaky wave contribution. The time delay between direct transmission and leaky wave contributions is attributed to the time for the propagation of the leaky wave before reraditating, as discussed. The long tail in transmission is a result of the leakage further from the centre taking longer decreasing leakage amplitude.

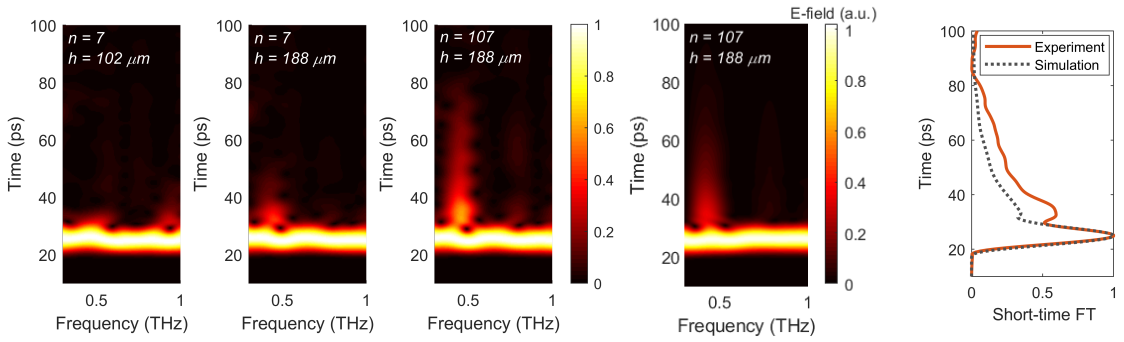

(a) Experiment (b) Simulation (c) Comparison

Figure 4.8: (a) Experimental and (b) simulated spectrograms of the time-domain waveforms. The short-time Fourier transformed field has been normalised for each frequency. Experimental waveforms were measured in collimated configuration for a thin dielectric sample with 7 slits and thick dielectric samples with 7 and 107 slits. Simulations were carried out in CST Microwave Studio for a structure with n=107 slits and thick dielectric. (c) Comparison of the experimental and simulated temporal E-field amplitude decay at ET frequency 0.44 THz for the structure with n=107 slits and thick dielectric structure.

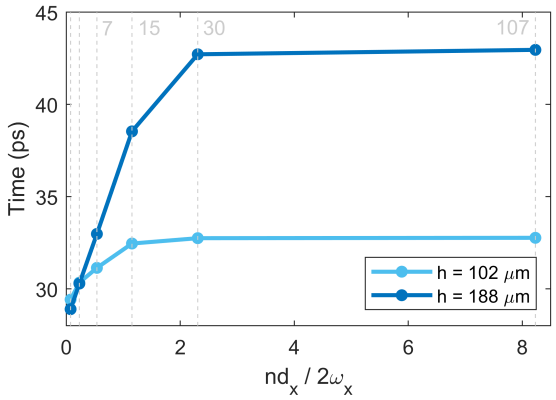

Figure 4.9: 1/e energy decay as a function of array length (nd_x), normalised by the illumination beam diameter ($2\omega_x$), for substrate-thin (h = 102 µm) and substrate-thick ($h = 188\mu$m) structures. The truncation of each array region is indicated by the dashed lines labelled by the number of slits.

4.2.4 Angular dependence of transmission

While normal transmission measurements provide some insight into the the physical mechanism of ET, a complete understanding of the origin of emission can be obtained through angular dependence measurements. This stems from the dispersion of the Floquet modes within the periodic region. Here, the radiating properties of the leaky waves are investigated through monitoring the angular dependence of transmission for samples with increasing number of slits, as previously studied for TM ET [34, 158, 161, 162, 166, 167, 168] and TE ET [154] for single slit structures flanked by corrugations [169]. This study focuses on a different geometry and its own nuances, such as mode development and the dependence on substrate thickness.

Figure 4.10 presents the angle-resolved transmission amplitude in the H-plane (xz-plane) at ET frequency for substrate-thin and -thick samples. As the number of slits is increased, one can observe a narrowing of the beamwidth of the main lobe, with reduction in amplitude beyond 10 deg. This narrowing saturates at $\sim$30 slits, consistent with the saturation observed in Figure 4.5. The interference fringes present are a result of the interference of all the illuminated slits, with the number of nodes per angular displacement increasing with number of slits. Comparing the angular transmission of the 107 slit samples, one can observe the maximum in transmission at 0 deg, or broadside, for the substrate-thin sample (Figure 4.10 (a)), whereas the maximum emerges at 1 deg for the substrate-thick sample (Figure 4.10 (b)). For the substrate-thick sample, the mode is fully developed, and hence the leaky wave associated with the TE_1 mode primarily contributes to the ET. The contribution of the $m = -1$ space harmonic is suppressed at broadside (0 deg), however, due to the open stopband, consistent with the leaky wave formalism [162].

To gain further insight into the modes contributing to ET, in addition to the quasi-optical effects on measurements, angle-resolved transmission spectra were obtained for substrate-

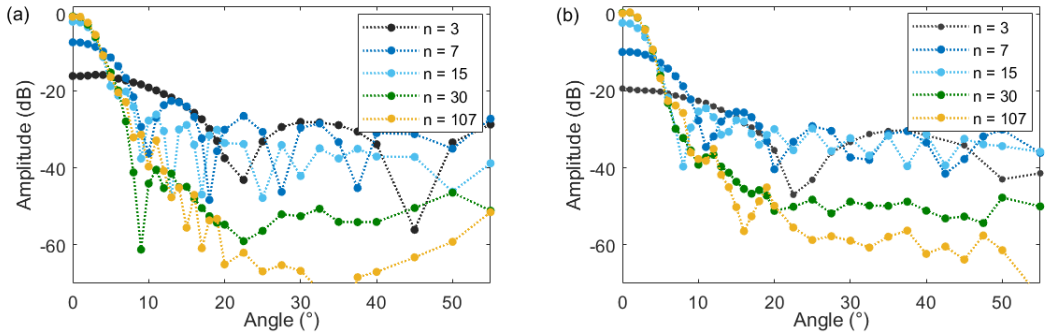

Figure 4.10: Radiation diagrams for substrate-thin (h = 102 µm) (a) and substrate-thick (188 µm) (b) structures at ET frequencies of 0.48 THz and 0.44 THz, respectively.

thin and -thick samples for collimated and focused setup configurations (see Methods), presented in Figure 4.11. ET is present at 0.4-0.5 THz for small angles, consistent with the $m = -1$ leaky mode. The development of the mode is evident from the increase in ET as the dielectric thickness is increased above threshold, in addition to the development of the Wood's anomaly from Figure 4.11 (a) to (b). The diffraction lobe at large scattering angles results from the scattered fields of the incident beam. This is related to the incident field and periodicity, not the dielectric slab mode.

The influence of quasi-optics on measurements and which modes are excited is revealed in the angle-resolved transmission obtained for the focused setup configuration (see Figure 4.11 (c) and (d)). Additional space harmonics are observable, which do not appear in the collimated measurements. Exciting the sample at larger angles allows coupling to higher order modes ($m = -2$ and $m = -3$). The angular dependencies of the modes obtained through method of moments calculations (indicated by the white dashed lines) are in good agreement with the measurements. All method of moments results presented in this chapter are provided by Miguel Camacho, University of Essex. These results are supported by simulations of the 107 slit thick-substrate structure under collimated and focused Gaussian illumination carried out in the transient solver of CST Microwave Studio. The ratio of

leaky wave to direct transmission was extracted from the transmitted time domain signal. The leaky wave contribution was found to be 0.69 and 0.72 for the collimated and focused configurations, respectively. This demonstrates that excitation at larger angles allows more efficient coupling to the structure and coupling to higher order modes.

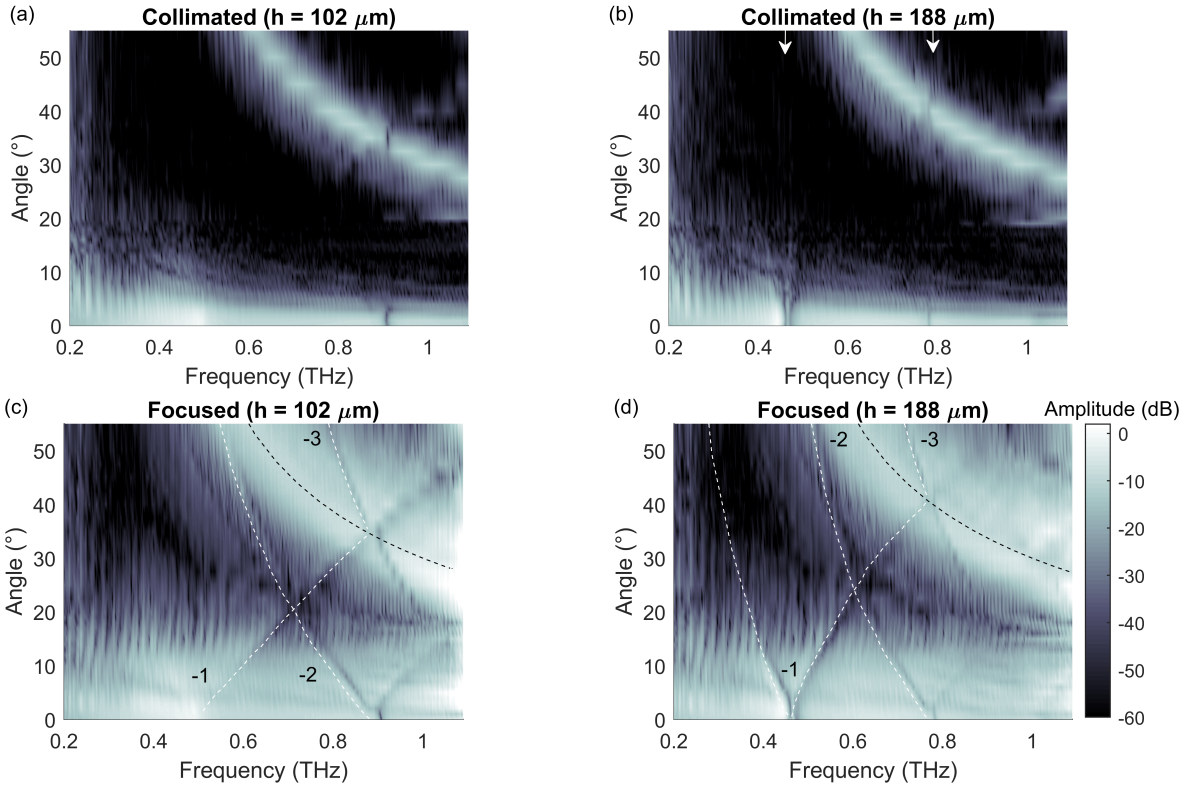

Figure 4.11: Colour maps of transmission amplitude in dB as a function of detection angle for substrate-thin and -thick samples with collimated ((a) and (b)) and focused (50 mm lens) ((c) and (d)) setup configurations. The arrows in (b) indicate the frequency of the first and second Wood's anomalies. The black dashed line in (c) and (d) presents the calculated emission for the diffraction or grating lobe, while the white dashed lines present the space harmonics calculated using the method of moments.

To support these results, simulations of the far field transmission for an infinite array were undertaken in CST Microwave Studio, presented in Figure 4.12 for different angles of the sample with respect to the beam path. The two high transmission regions branching from

0.46 THz at 0 deg observed in both the experiment and simulation results are attributed to the $m = -1$ leaky mode. They exhibit a larger angular dependence for the focused configuration (Figure 4.11 (d)) since the field is incident at larger angles to the surface normal, while the lens after the sample increases the numerical aperture of the detector. This is consistent with the simulations in Figure 4.12. Additionally, a narrow resonance emerges between these two branches, with negligible angular dispersion. This is thought to be attributed to the $m = -1$ asymmetric mode [142, 156]. This is known as the odd mode in the circuit model formalism, observable only in thick screens with low ohmic losses [136].

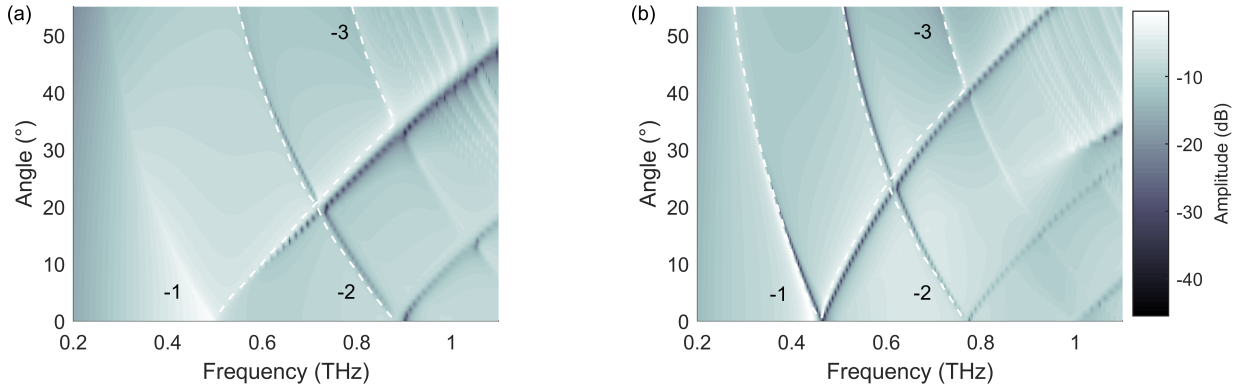

Figure 4.12: Simulation of transmission through infinite periodic arrays with dielectric thicknesses 102 µm (left) and 188 µm (right) using unit cell boundary conditions and Floquet ports, calculated using CST Microwave Studio. The space harmonics calculated using Method of Moments are illustrated by the white dashed lines.

4.2.5 Summary

This work presents a detailed understanding of the leaky wave mechanism responsible for ET and its dependence on structural and illumination conditions. This understanding lends itself to utilising high field confinements of the order of hundreds of microns for sensing applications, whereby dielectric properties of analytes can be probed with high sensitivities.

For effective sensing, knowledge of spatial distribution and energy transport is fundamental. The next section moves towards generating surface waves along a platform, for ease of analyte deposition, with focus on fabrication and surface wave attenuation.

4.3 Surface wave structures

The work presented in this section is based on the article S. Freer, *et al.*, 'Time-Frequency Characterization of Laser Micromachined Terahertz Surface Waves', *in preparation.*

The focus of this section lies with three core aspects of metamaterial design: geometric design, structure fabrication and characterisation of surface wave attenuation. Metamaterial design fundamentally relies on fabrication quality of surfaces. Imperfections in design result in scattering of the electromagnetic fields, and hence, increased attenuation. Common metamaterial fabrication techniques for millimeter wave and terahertz include electroforming [170], 3D printing [35, 171] and laser machining. Electroforming generates structures of high precision, however, it is an expensive technique, while 3D printing is limited at scales matching the dimensions of terahertz wavelengths. Laser micro-processing, however, is an attractive, non-conventional manufacturing technology for the fabrication of a wide range of micro-components. This is attributed to its intrinsic processing attributes for: (i) non-contact machining that can be used to structure/process a wide range of materials and producing complex free-form (3D) structures that incorporate multi-length scale features with complex geometrical designs; and (ii) in-situ selective functionalisation of free-form surfaces. It therefore shows promise for quality machining when pushed to sub-micro scales, with the additional advantage of being relatively inexpensive. Despite this, laser machining as a fabrication tool remains somewhat unexploited in the terahertz regime.

The third focus, characterisation of surface wave attenuation, leads on from fabri-

cation, encompassing both Ohmic and scattering losses of the EM field. Regardless of the immense capability of surface waves for not only sensing [172, 173, 174], but also for waveguiding control [175, 176, 177, 178], on-chip spectroscopy and communication [179], rigorous studies of surface wave characteristics, specifically attenuation, is limited in the literature. Knowledge of the attenuation of surface waves is fundamental for specific application. Sensing requires an understanding of the field-analyte interaction, and hence field distribution along the structure. Communication requires an understanding of attenuation to predict information transmission lengths. This knowledge gap, coupled with the promise of laser machining, motivates this study of the attenuation of surface electromagnetic waves generated through laser micro-processing and its characterisation for different geometries.

4.3.1 Geometric design: Dispersion characterisation

The surface wave structures under investigation are aluminium surfaces with three different geometric patterning: grating, array of holes and array of nails. Dimensions of the periodic structures were designed such that they supported a surface wave with frequency between 0.3 THz – 0.75 THz, to coincide with the peak signal of the TDS excitation system. The unit cell of each geometry is presented in Figure 4.13, with periodicity, p, pattern height, h, and width, w presented in Table 4.2. One can determine the dispersion of the surface waves, much like the grounded dielectric slab modes in the previous section, through analytical modelling and simulations of EM fields. The following section outlines modelling of the modes supported by all three geometries.

Analytical and Simulated Mode Calculations

The EM modes supported by a one-dimensional PEC grating, array of holes and array of nails can be modelled through calculating the reflectance of an incident incident plane wave

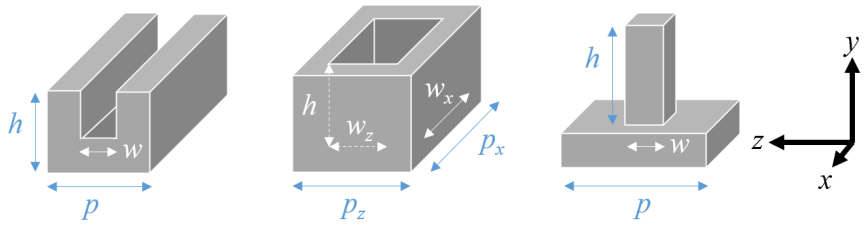

Figure 4.13: Unit cell diagrams of the corrugated platforms: grating, blind holes and nails (left to right). The pattern height, width and periodicity is denoted by h, w and p, respectively.

with parallel momentum $k_{||}$ for the case where the plane wave is evanescent, $k_{||} > \omega/c_0$ [180]. The locations of the divergences in the reflectance gives the dispersion relation of the surface mode, given by

$$\frac{\sqrt{k_{||}^2 - k_0^2}}{k_0} = \frac{w}{p}\tan(k_0 h), \tag{4.7}$$

$$\frac{\sqrt{k_{||}^2 - k_0^2}}{k_0} = \frac{S^2 k_0}{\sqrt{\pi^2/a^2 - \epsilon_h k_0}} \frac{1 - e^{-2|q_y|h}}{1 + e^{-2|q_y|h}} \tag{4.8}$$

of the grating and holes, respectively, where S is the overlap integral of the plane wave and fundamental mode inside the hole, ϵ_h is the permittivity of the environment, and q_y is the propagation constant $q_y = \sqrt{\epsilon_h k_0^2 - \pi^2/a^2}$. The reflectivity of the array of holes is given by [181, 182]:

$$R = -\frac{k_h k_p^2 \tan(k_h h) - k_{||}^2 \gamma \tanh(\gamma h) + \epsilon_h \gamma_0 (k_p^2 + k_{||}^2)}{k_h k_p^2 \tan(k_h h) - k_{||}^2 \gamma \tanh(\gamma h) - \epsilon_h \gamma_0 (k_p^2 + k_{||}^2)} \tag{4.9}$$

where $\gamma = \sqrt{k_p^2 + k_{||}^2 - \beta_0^2}$ and $\gamma_0 = \sqrt{k_{||}^2 - k_0^2}$ are the surface and free space propagation constants and $k_p^2 = \frac{2\pi/d}{\ln(\frac{d}{2\pi r}) + F(r)}$ ($F(r) = 0.5275$ for a square grid [183]).

These models assume that the structures are subwavelength and the material is a perfect electric conductor. To verify the analytical models and the significance of this assumption, the unit cell of each was modelled in the Eigenmode Solver in CST Microwave Studio to determine the eigenmodes and dispersion relations of each. Figure 4.14 presents

		h	w (x/z)	p (x/z)
Grating	Designed	0.08	0.05	0.10
	Measured	0.08	0.04	0.10
Nails	Designed	0.08	0.05	0.10
	Measured	0.05	0.08	0.16
Holes	Designed	0.20	0.21/0.06	0.31/0.16
	Measured	0.14	0.25/0.09	0.31/0.16

Table 4.2: Designed and measured unit cell dimensions of each structure design. The x/z dimensions of the holes are different. The dimensions were measured using an Olympus measurement microscope, with measurement uncertainty 0.01 mm.

a comparison of the dispersion for the grating, array of holes and array of nails. One can observe fairly good agreement between the analytical and simulated results, with small deviation close to the frequency cutoff due to assumptions of the analytical model, such as subwavelength periodicity. At high frequencies, the wavevector for all three structures deviates from the wavevector of light. This results in slow propagation and high confinement of the mode to the structure. At these frequencies the mode is no longer subwavelength.

Tolerance Characterisation

The structural ability to support surface waves of the intended frequency fundamentally relies on the precision of the fabrication process. To demonstrate the design tolerance of the structures, the grating unit cell was modelled in the Eigenmode Solver in CST Microwave Studio for varying structural dimensions. The calculated dispersion relations can be found in Figure 4.15. The frequency of the surface mode is largely determined by the height of the corrugation. The confinement is indicated in Figure 4.15 (c), where the absolute value

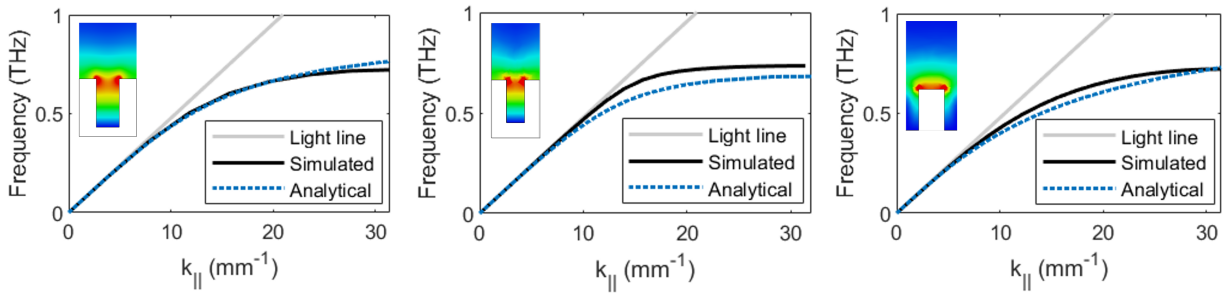

(a) Grating (b) Array of holes (c) Array of nails

Figure 4.14: A comparison of the analytical and simulated dispersion diagrams for the (a) grating, (b) array of blind holes and (c) array of nails. The insets show maps of the normalised absolute value of the E-field supported by each structure.

of the E-field decays faster for increasingly confined modes. The use of phase as opposed to wavenumber is for easy comparison of the dispersion for varying periodicity. The phase is 180 deg at the Brillouin zone boundary, where the wavenumber parallel to propagation is equal to π/p.

During fabrication, control over the taper angle on side walls of structures is limited. Alongside unit cell dimensions, taper angle has a significant influence on the dispersion of the mode supported by the structure. Figure 4.16 illustrates the dependence of the dispersion on the taper for taper angles θ, defined in the inset. A significant dependence can be observed, highlighting the importance of accounting for it in the design process of structures.

4.3.2 Fabrication and topography

The aluminium structures were fabricated by Pavel Penchev using a state-of-art laser micro-processing system Lasea LS4. Details of the system can be found in Appendix 4.6.5. The structure platform dimensions were 40 × 50 mm in the xz-plane. The three-dimensional profiles of the structures were measured using Focus Variation (FV) technology optical mi-

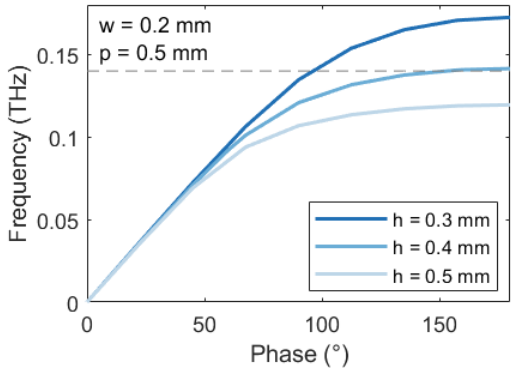

(a) Corrugation height

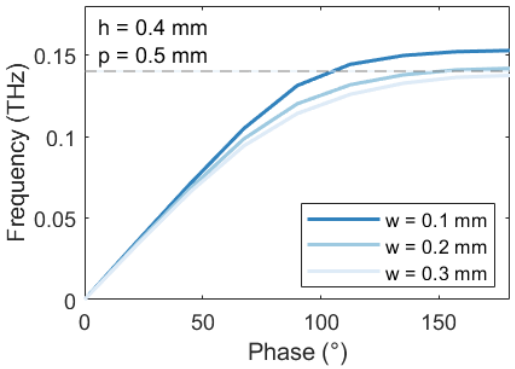

(b) Corrugation width

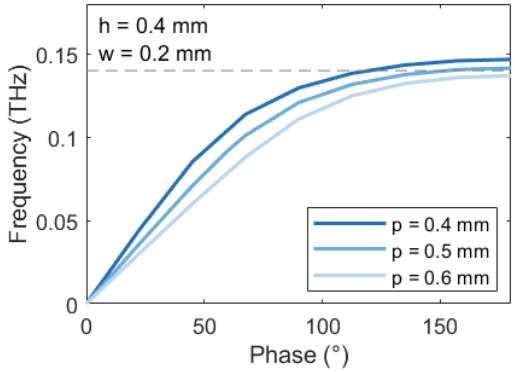

(c) Corrugation period

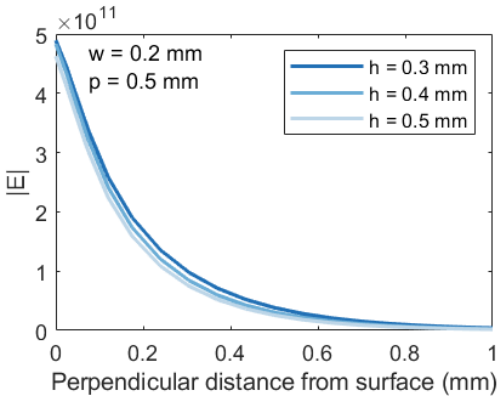

(d) Corrugation height

Figure 4.15: Dispersion diagrams of the grating structure for varying (a) corrugation height, (b) width and (c) periodicity. The structure was designed to have cutoff frequency 0.14 THz. Panel (d) presents the decay of E-field along the y-axis for varying corrugation height (from the top of the unit cell). The inset in (b) presents the labelled unit cell. The phase is 180 deg at the Brillouin zone boundary, where the wavenumber parallel to propagation is equal to π/p. (The use of phase is for easy comparison of the dispersion for varying periodicity.)

croscope, namely Alicona InfiniteFocus (IF) G5. Profiling measurement details can be found in Appendix 4.6.6. The 3D profiles of each structure are presented in Figure 4.17. One can observe notable surface roughness in the profiles, resulting from laser processing. This will naturally increase scattering of the surface wave, affecting the transmission along the

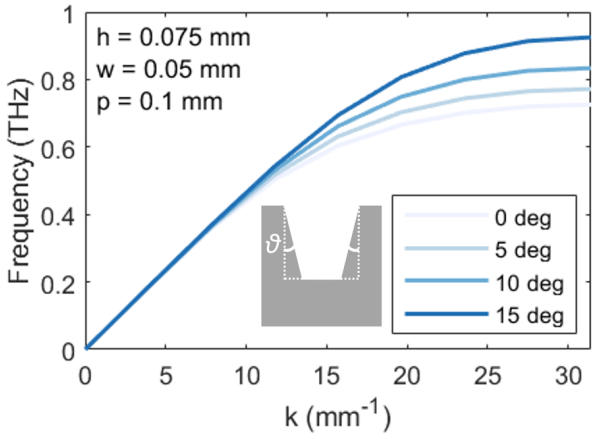

Figure 4.16: Dispersion relation of the grating structure with varying taper angles, defined by θ in the inset.

structure. This is important to consider for applications such as communication and sensing, highlighting the importance of the study of field attenuation.

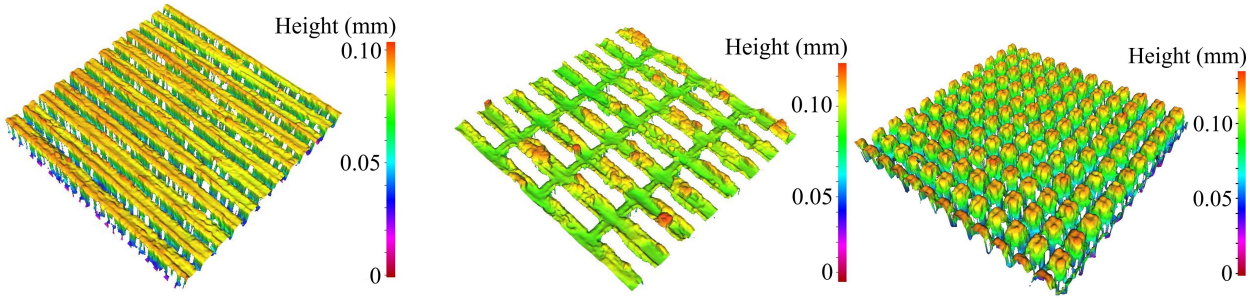

(a) Grating (b) Holes (c) Nails

Figure 4.17: Three-dimensional profiles of the (a) grating, (b) array of holes and (c) array of nails.

4.3.3 Dispersion

The EM responses of the three surface wave structures were experimentally investigated in both the time and frequency domain, through excitation using a TDS system. This provides invaluable dispersion information of the waves. The first experimental challenge

faced in exciting surface wave structures is achieving coupling of radiation to the structure. A surface wave has a wavenumber greater than that of free space. A momentum mismatch therefore exists between free space waves and surface waves, inhibiting the coupling of the two. To overcome this mismatch, the terahertz radiation emitted by the TDS PCA was scattered using a razor edge, see Figure 4.18.

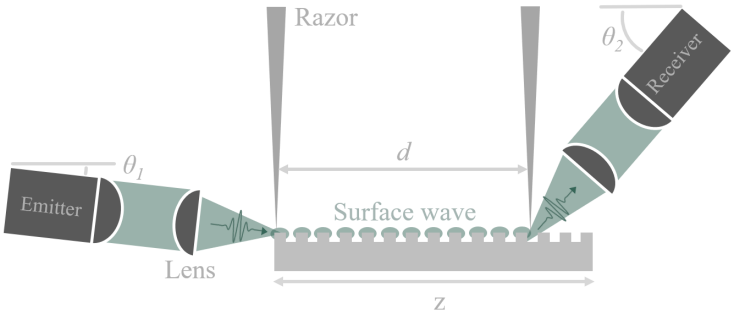

Figure 4.18: Illustration of the razor coupling scheme. Photoconductive antennas (PCAs) are used for emission and detection of the terahertz pulses. TPX50 lenses (focal length 50 mm) are used to focus and collect the radiation. The propagation distance of the surface wave d is defined as the distance between the two razors. The emitting and receiving PCAs are rotated from the horizontal axis by approximately $\theta_1 = 5°$ and $\theta_2 = 40°$, respectively, to achieve optimal coupling. This was determined experimentally.

The energy couples to the structure as a surface wave, propagates along the patterned surface, before undergoing scattering by the second razor-edge, to be detected by the receiving PCA. Figure 4.19 presents both the temporal waveform and frequency spectrum of the surface wave supported by the grating, array of holes and array of nails. To illustrate the temporal response of discrete spectral components, and hence the dispersion of the wave, the spectrogram can be calculated from the waveform, as shown in the figure. One can observe consistency with the dispersion of the surface waves presented in Figure 4.14, whereby the array of holes exhibits a sharper frequency cutoff than the grating and array of nails. The array of nails appears to exhibit increased confinement over the grating and holes, consistent

with the calculated dispersion, whereby the wavenumber diverges from the light line (grey line in Figure 4.14) at lower frequencies.

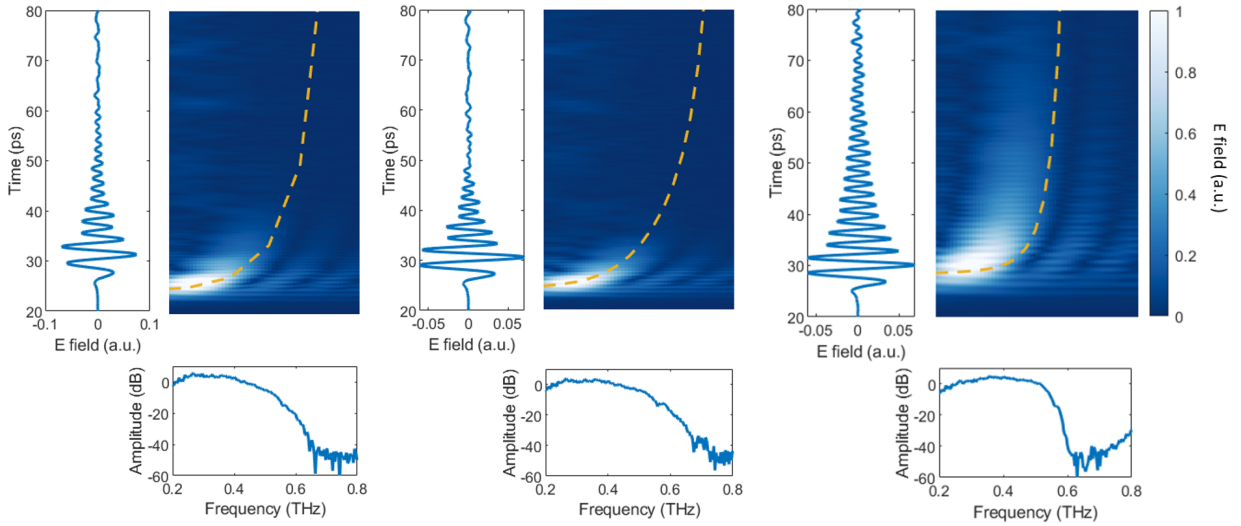

(a) Grating (b) Holes (c) Nails

Figure 4.19: Spectrograms of the absolute value of the transmitted E-field along the (a) grating, (b) array of holes and (c) array of nails. The temporal and frequency responses of each are presented alongside the y and x axes of each spectrogram, respectively. The yellow dashed lines illustrate the analytical dispersion calculated for the measured structure dimensions found in Table 4.2. Note a taper angle of 15° was used for the grating geometry.

4.3.4 Attenuation

Knowledge of the attenuation of a surface wave, as discussed, is imperative for surface wave application. It is broadly defined as

$$\alpha_{SW} = -\frac{\ln\left(|E(\omega)_{D2}|^2/|E(\omega)_{D1}|^2\right)}{\Delta D} \tag{4.10}$$

where $E(\omega)_D$ is the E-field amplitude at position D along the structure and ΔD is the difference between two positions $D1$ and $D2$. This characterises 'path loss', defined in

the field of telecommunications. Surface waves typically suffer from Ohmic losses, scattering losses due to surface roughness and propagation divergence (i.e. in-plane spreading). Lack of distinguishing attenuation and path loss in the terahertz surface wave literature is somewhat problematic for the few reported attenuation values [184, 185, 187, 186, 188]. Despite the significance of surface roughness on surface wave attenuation, its study has been neglected until now.

Figure 4.20 presents the attenuation, calculated from Eq. 4.10. The second (detecting) razor edge was positioned at two different distances along the structure ($D1$ and $D2$) and the transmitted E-field was measured for each. Five distances were used and the detecting razor and PCA were moved as a unit.

The path loss of all three surface waves increases with frequency due to increased confinement and decreased group velocity. Increased confinement enhances scattering effects due to surface roughness, while slower group velocity results in greater interaction times between the surface wave and metal surface, resulting in higher Ohmic losses. Above 0.6 THz, such large losses result in low signal-to-noise ratio (SNR) of the detected field and hence higher frequencies are not presented. One can observe increasing attenuation of the E-field for the grating to array of holes to array of nails. This result is inconsistent with two-dimensional full-wave simulations, attributed to propagation divergence. The two-dimensional simulations do not account for in-plane spreading of the surface wave (non-zero x-propagation), computing attenuation, rather than path loss. This is not the case for the grating, however, in which boundary conditions prohibit propagation along x.

Table 4.3 presents the simulated (α_{sim}^{ideal}, α_{sim}^{rough} and $\alpha_{sim}^{eff.cond.}$) and measured (α_{meas}) path loss (i.e. attenuation only) of the grating geometry at multiple frequencies, while Figure 4.21 presents the simulated and measured attenuation for all three structures. α_{sim}^{ideal} and α_{sim}^{rough} denote the simulated attenuation for structures without and with surface roughness

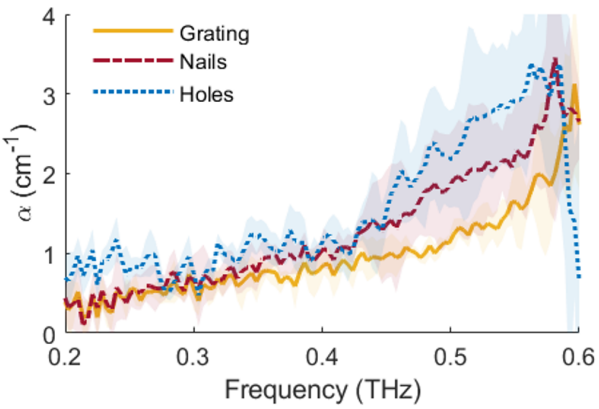

Figure 4.20: Attenuation of the transmitted E-field along the grating, array of nails and array of holes.

of 6.5 µm (root-mean-square). The simulations were undertaken in the transient solver of CST Microwave Studio for a structure without and with surface roughness of 6.5 µm (root-mean-square). The discrepancy between the path loss along the grating calculated through modelling the surface roughness through modified electric conductivity and measured path loss, $\alpha_{sim}^{eff.cond.}$ and α_{meas}, highlights the drawback of the common modelling method of assigning an effective conductivity to a metal to account for roughness for application to surface waves at higher frequencies. For an accurate estimate of the attenuation of surface waves, it is fundamental to physically model the roughness through modelling a 2D surface in MATLAB. The underestimation of simulated attenuation for the holes and nails in Figures 4.21(b) and (c) is a result of the omission of in-plane spreading, i.e. only the attenuation is simulated, rather than path-loss, as in the experiments.

Freq (THz)	$\alpha_{sim}^{ideal}(cm^{-1})$	$\alpha_{sim}^{rough}(cm^{-1})$	$\alpha_{sim}^{eff.cond.}(cm^{-1})$	$\alpha_{meas}(cm^{-1})$
0.3	0.16	0.15 ± 0.14	0.42	0.56 ± 0.21
0.4	0.19	0.44 ± 0.22	0.74	0.79 ± 0.21
0.5	0.53	1.38 ± 0.39	2.35	1.13 ± 0.11
0.6	0.85	2.22 ± 0.10	4.33	2.65 ± 0.96

Table 4.3: Simulated ($\alpha_{sim}^{ideal}/\alpha_{sim}^{rough}/\alpha_{sim}^{eff.cond.}$) and measured ($\alpha_{meas}$) attenuation of the grating structure at several frequencies. α_{sim}^{ideal} and α_{sim}^{rough} denote the simulated attenuation for structures without and with surface roughness of 6.5 µm (root-mean-square). The simulations were undertaken in the transient solver of CST Microwave Studio for a structure without and with surface roughness of 6.5 µm (root-mean-square).

4.3.5 Sensing

Simulation

Here, the sensing capabilities of the structures are investigated through simulation of the surface wave for different dielectric environments. Simulations of the platforms were carried out in both the eigenmode solver and the transient solver of CST Microwave Studio. Simulation in the eigenmode solver is an efficient method of calculating the dispersion relation of the eigenmodes supported by a unit cell, while the transient solver provides temporal information about the propagation of the E-field. Initially, a study of the thickness of the dielectric layer was undertaken, to determine the minimum sample thickness required for sensing independent of sample volume. This also provides information about the field distribution of the evanescent field along the y-axis, away from the surface.

Figure 4.22 (a) presents the change in surface wave dispersion and for the grating geometry, simulated in the Eigenmode Solver in CST Microwave Studio, for increasing sample

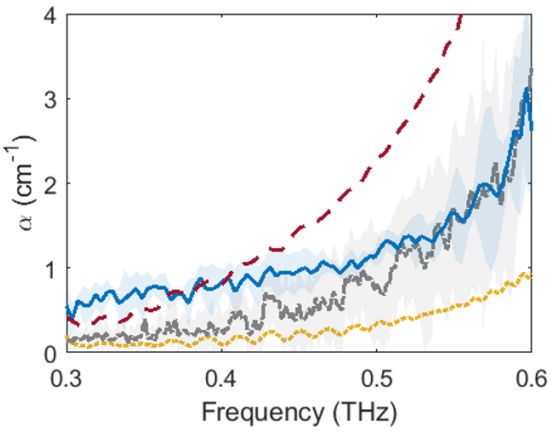

(a) Grating

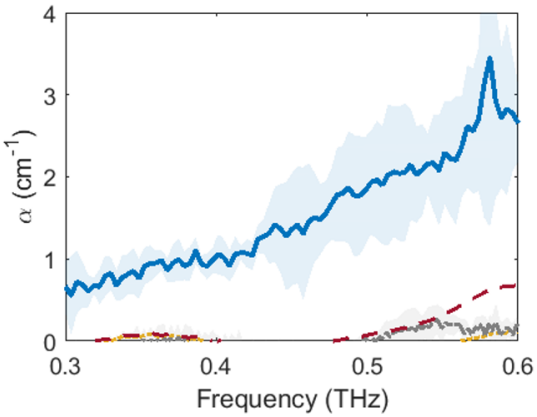

(b) Holes

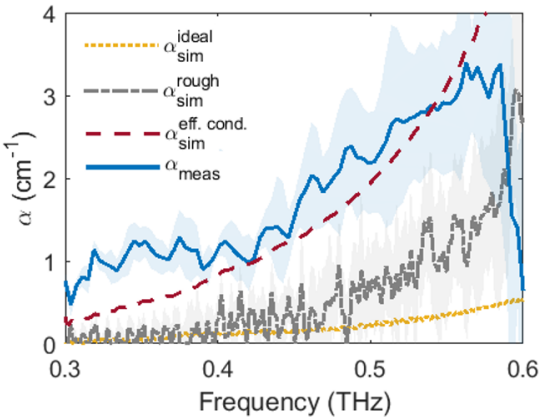

(c) Nails

Figure 4.21: Simulated ($\alpha_{sim}^{ideal}/\alpha_{sim}^{rough}/\alpha_{sim}^{eff.cond.}$) and measured ($\alpha_{meas}$) attenuation of the (a) grating, (b) array of nails and (c) array of holes. The simulations were undertaken in the transient solver of CST Microwave Studio for a structure without and with surface roughness of 6.5 µm (root-mean-square).

thickness, defined from the lowest point in the grating. One can observe a delay in confinement of the surface wave with increasing sample height. The cutoff frequency was extracted from the dispersion and presented in Figure 4.22 (b). This is proportional to the inverse of the square root of the sample height, illustrated by the $1/\sqrt{h_s}$ fit.

To determine the surface wave sensitivity on its dielectric environment, a semi-infinite

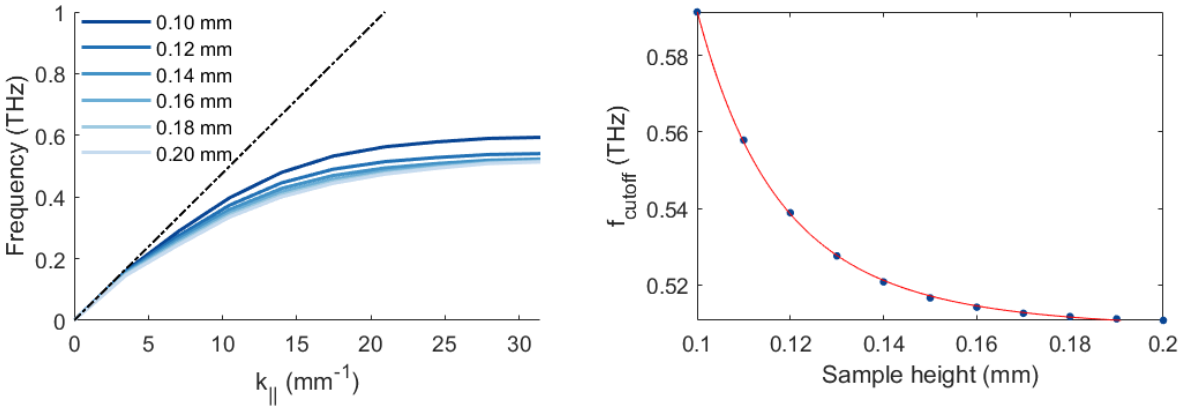

(a) (b)

Figure 4.22: (a) Dispersion diagram and (b) cutoff frequency of the surface wave supported by the grating geometry, simulated in the Eigenmode Solver in CST Microwave Studio, for increasing sample thickness, defined from the lowest point in the grating. Sample permittivity was defined as Re(ϵ)=2 and Im(ϵ)=0.02. Cutoff frequency was defined as the mode frequency at wavenumber 28 mm^{-1}.

dielectric environment was modelled in a two-dimensional simulation, with variable real and imaginary permittivity. Figure 4.23 presents the change in cutoff frequency and time of arrival of the E field for samples with increasing real permittivity. The phase velocity is related to the propagation constant and frequency $\sim q_y/f$. Given the propagation constant $q_y = \sqrt{\epsilon_h k_0^2 - \pi^2/w^2}$, one would expect the cutoff frequency to be proportional to $1/\sqrt{\epsilon}$. This was confirmed by the second order power fit illustrated in red.

Experiment

To investigate the experimental sensitivity of the structures, the analyte anhydrous lactose was procured to modify the dielectric environment of the surface wave. This was chosen due to its resonance at 0.53 THz [189, 190], attributed to lactose-active modes from molecular rotations in the crystal structure, confirmed by first-principle calculations [191]. The

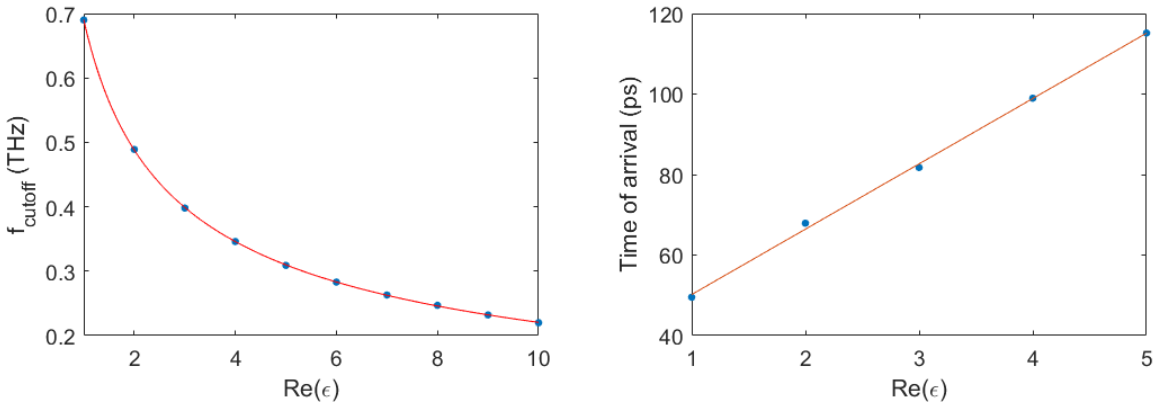

(a) (b)

Figure 4.23: (a) Cutoff frequency and (b) arrival time of E field for increasing real sample permittivity.

initial study investigates the effect of increasing analyte mass deposited on the surface of the structure. Anhydrous lactose powder was deposited on the surface of each structure as uniformly as possible using a syringe, in mass increments of ∼5 g. After each deposition, the transmitted E-field was measured. The excitation and detection razor edges were positioned ∼15 mm apart. Figure 4.24 presents the temporal E-field amplitude transmitted across the grating surface wave structure for increasing analyte mass, alongside the spectra post-Fourier transformation. One can observe an increase in time of arrival of the terahertz signal with increasing analyte mass, paired with a decrease in E-field amplitude. This observation is consistent with an increase in permittivity of the dielectric environment at the structure surface. The exponential behaviour of each is attributed to the exponentially decaying E-field distribution of the surface wave away from the surface. Once the analyte fills the surface wave region, increasing the analyte mass is inconsequential.

The resonance at 0.53 THz cannot be observed in the spectra. This is attributed to the low SNR near the cutoff frequency of the surface wave. Efforts were made to increase this SNR through decreasing the dimensions of the unit cell. Despite increasing the cutoff

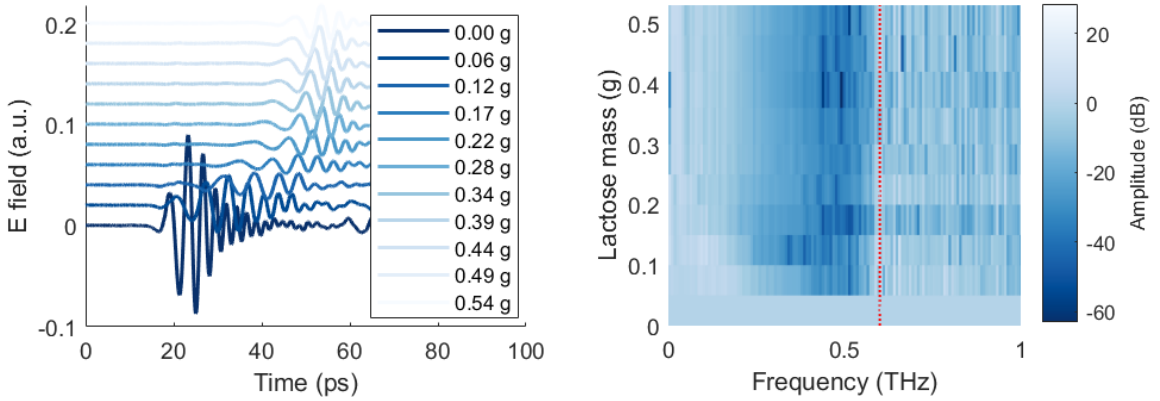

Figure 4.24: (a) Temporal E-field amplitude and (b) spectral amplitude of the transmitted field across the grating surface wave structure for increasing powdered lactose mass. The spectral amplitude is normalised to the amplitude measured for no lactose present. The red dashed line illustrates the cutoff frequency of the structure.

frequency to ∼0.9 THz, low SNR remained a limitation.

A method of increasing the SNR of the terahertz surface wave is to increase the amount of energy coupling to the surface. This can be achieved through two routes: increasing the power of the source, with the caveat that high power may destroy the analyte, and increasing the coupling efficiency from the source to structure. Section 4.4 investigates this for improved device sensitivity.

4.4 Enhanced coupling efficiency

High instrument sensitivity relies on high field-matter interactions, and naturally, efficient coupling to the surface wave mode. The current razor scattering approach achieved coupling efficiencies of $\sim 5\%$, calculated in CST Microwave Studio. This section looks towards improving these efficiencies through graded guiding of the terahertz waves.

Metasurfaces can be designed to allow a transition from free space wave to spoof surface plasmon, overcoming the momentum mismatch. Gradual changes in groove depth and metallic flares are commonly used to provide a gradient index, and hence efficient coupling [33]. Large amounts of work has gone into designing structures for efficient coupling, largely for microwave antenna applications [46]. This work aims to extend this technology into the terahertz regime, for efficient coupling from a continuous wave TeraSense IMPATT diode waveguide port, operating at 0.14 THz, to a metallic grating platform.

4.4.1 Design

To support a highly-confined surface mode at 0.14 THz, the grating geometry was designed with periodicity $p = 0.5$ mm, corrugation height $h = 0.4$ mm and width $w = 0.2$ mm, using the eigen-mode solver of CST Microwave Studio. Inspired by microwave transition structures [46, 192], a coupling transition of length $\sim 2.6\lambda_0$ (where λ_0 is the free-space wavelength at 0.14 THz) was designed. This consisted of a graded grating section and a smooth upper flare, illustrated in Figure 4.26. In the graded grating section, the corrugation height was increased exponentially from $h = 0$ mm to $h = 0.4$ mm, while the upper flare had an exponential profile, selected from multiple designs such as upward and downward linear and cylindrical profiles, for optimal coupling [46, 192]. Each component was optimized in the transient-solver of CST Microwave Studio. Drawings of the structure are presented in Figure 4.25. To enable the

measurement of transmission across the structure using vector network analyzers (VNAs), in addition to avoiding reflection of the surface wave, the transition section mirrored, promoting recoupling to the waveguide mode.

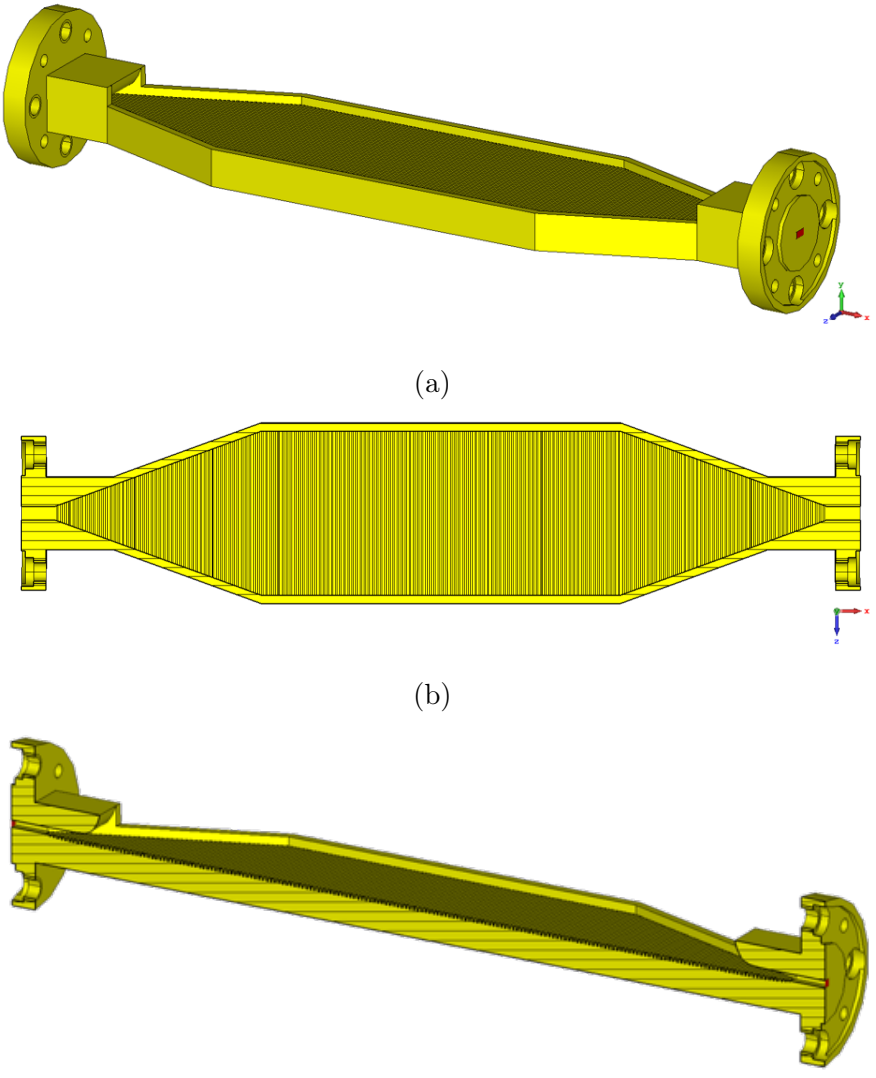

(a)

(b)

(c)

Figure 4.25: Drawings of the surface wave launcher, generated in CST microwave studio.

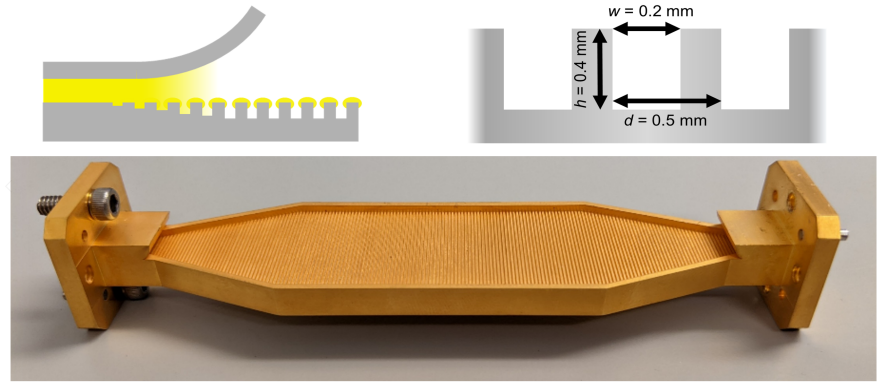

(a)

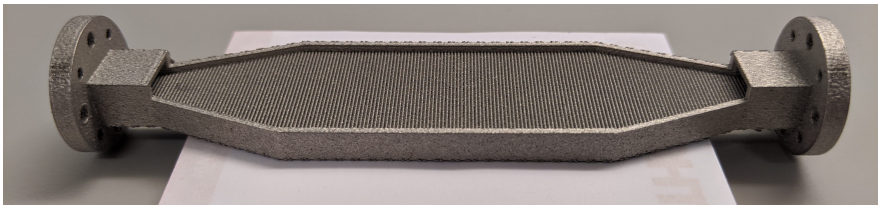

(b)

Figure 4.26: (a) Image of the surface wave launcher, fabricated by electroforming by TK Instruments. The diagrams illustrate the graded transition structure (left) and grating dimensions (right). (b) Image of the surface wave launcher fabricated by 3D printing.

4.4.2 Fabrication

Given the dimensions of the structure, the high precision generated by electroforming was necessary for fabrication [170]. Figure 4.26(a) presents images of the aluminium structure, produced by TK Instruments. To illustrate the importance of fabrication technique, Figure 4.26(b) presents an image of the structure fabricated using 3D printing. The visible high surface roughness of the 3D printed structure demonstrates the superiority of electroforming as a fabrication technique. To reduce losses due to scattering of fields, studied in Section 4.3.4, the structure produced using electroforming is used for the following work.

4.4.3 Simulation and experiment

To characterise the surface wave launcher, and determine the coupling efficiency of the transition structure, the propagation of the E-field across the transition structure was simulated in CST Microwave Studio. Figure 4.27 presents the absolute value of the E-field. One can observe the confined surface wave propagating along the structure. The attenuation across the structure is attributed to Ohmic losses and scattering, discussed in Section 4.3.4. To determine the coupling efficiency, the transmission parameter was extracted from CST, presented in Figure 4.28. The cutoff of the surface wave is evident at 0.14 THz, as designed.

Measurements of both the reflection and transmission were undertaken using a VNA system. Figure 4.28 presents a comparison of the experimental and simulated parameters. For each, there is fairly high transmission up to the cutoff frequency, with a coupling efficiency of 99%, calculated through S11 measurements, a vast improvement on the 5% achieved through razor-edge scattering. The shift in frequency of the cutoff is thought to be due to the mismatch in dimensions between the simulated and real structure. Profiling measurements of the structure dimensions, alongside simulations, confirmed this discrepancy. The fluctuations in transmission observed in the experimental measurements is attributed to reflections of the field along the structure.

4.5 Chapter conclusion

This chapter has presented a rigorous study of the design, behaviour and excitation of surface waves. Section 4.2 discussed the development of surface waves in the form of grounded dielectric slab modes, through analytical work, simulations and TDS measurements. It illustrates the importance of spatial distribution and energy transport for sensing application, through monitoring the ET of the field.

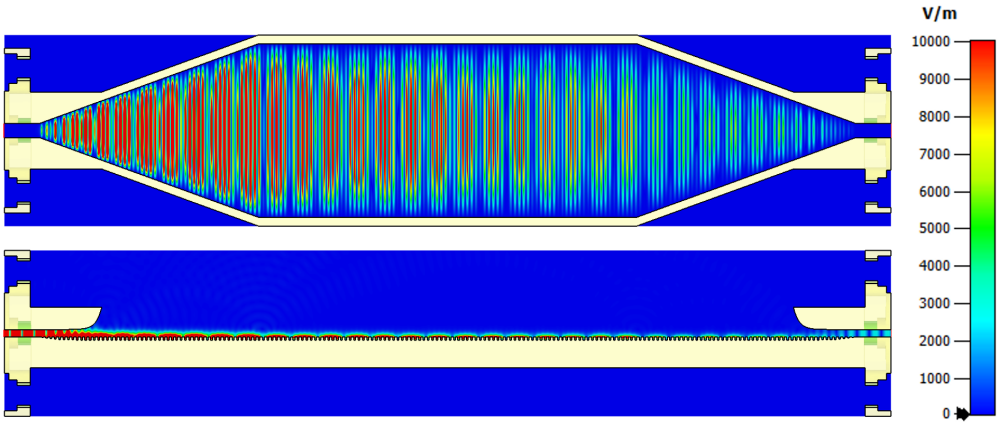

Figure 4.27: Absolute value of the E-field supported by the aluminium surface wave launcher at 0.14 THz, simulated in CST Microwave Studio.

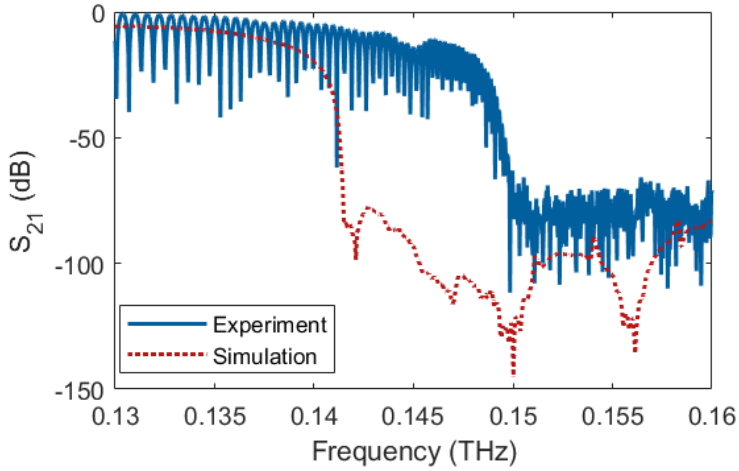

Figure 4.28: Experimental and simulated transmission S-parameter (S21) of the surface wave launcher. Measurements were taking using a VNA. Simulations were performed in CST Microwave Studio.

Section 4.3 expands on this work through investigation of different geometric patterns designed to support surface waves. The dispersion of a surface wave determines its spatial distribution and confinement. Different geometries provide different surface wave behaviour, which can be tuned for specific sensing application. Knowledge of the attenuation of the surface wave is imperative for application, not only for sensing, but also communica-

tion. Despite this, the study of attenuation is largely omitted in the literature. A rigorous characterisation of the attenuation of the surface waves was performed using TDS measurements, supported by simulations. Surface roughness, an unavoidable result of fabrication, was characterised for laser machined devices. This is fundamental to consider when selecting fabrication techniques.

Section 4.4 focuses on the excitation mechanism of surface waves. Inspiration was taken from the microwave regime, where microwave transition structures aid the coupling of energy to surface wave structures. A coupling efficiency of 99% was achieved through VNA excitation, a vast improvement on the 5% achieved through the standard razor-edge scattering approach.

Future work aims to utilise these structures for sensing biological analytes, such as blood glucose. The highly confined fields supported by these structures, together with the highly efficient coupling mechanism, provides promise for the surfaces as sensitive, portable, on-chip sensing devices.

4.6 Appendices

4.6.1 Appendix A: Calculating the propagation constants of grounded dielectric slab modes

Fig. 4.1 presents a dielectric of thickness d and dielectric constant ϵ_r with a metallic backing. To determine the eigenvalue equations of the modes supported by the grounded dielectric slab, one must solve the wave equations at the air-dielectric interface. This will be demonstrated for the TE modes. Propagation along the z-axis is assumed, with propagation factor $e^{i\beta z}$.

The E_z field satisfies the wave equations in the air and dielectric regions

$$\left(\frac{\partial^2}{\partial x^2} + k_c^2\right) h_z(x,y) = 0, \qquad \text{for } 0 \leq x \leq h, \tag{4.11}$$

$$\left(\frac{\partial^2}{\partial x^2} - q^2\right) h_z(x,y) = 0, \qquad \text{for } h \leq x < \infty, \tag{4.12}$$

where $H_z(x,y,z) = h_z(x,y)e^{i\beta z}$. k_c^2 and q^2 are defined as the cutoff wavenumbers for the air and dielectric region,

$$k_c^2 = \epsilon_r k_0^2 - \beta^2, \tag{4.13}$$

$$q^2 = \beta^2 - k_0^2, \tag{4.14}$$

where β is the propagation constant in both regions.

The general solutions to Eq. 4.11 and Eq. 4.12 are

$$h_z(x,y) = A\sin k_c x + B\cos k_c x, \tag{4.15}$$

$$h_z(x,y) = Ce^{qx} + De^{-qx}. \tag{4.16}$$

From the condition that states that the field must be finite at an infinite distance from the source, $C = 0$. From

$$E_y = \frac{i\omega\mu}{k_c^2}\frac{\partial H_z}{\partial x}, \tag{4.17}$$

$A = 0$ for $E_y = 0$ at $x = 0$. Hence, for continuity of E_x at $x = h$,

$$\frac{-B}{k_c}\sin k_c h = \frac{D}{h}e^{-qh}. \tag{4.18}$$

For continuity of H_z at $x = h$

$$B\cos k_c h = De^{-qh}. \tag{4.19}$$

Eq. 4.18 and Eq. 4.19 can be solved simultaneously to give the determinantal equation

$$-k_c \cot k_c h = q. \tag{4.20}$$

From the wavenumber definitions in E. 4.13 and 4.14,

$$k_c^2 + q^2 = (\epsilon_r - 1)k_0^2. \tag{4.21}$$

Eq. 4.20 and Eq. 4.21 can be solved simultaneously to find k_c and q. The equations can be represented in the $k_c h, qh$-plane, as presented in Fig. 4.29. Eq. 4.21 is represented by the circle of radius $\sqrt{\epsilon_r - 1}k_0 h$. This is proportional to the electrical thickness of the dielectric slab. From the intersection of the circle and Eq. 4.20, one can calculate the propagation constants of each mode. These constants were found using a bisection root finding algorithm and presented in Fig. 4.2. Excluding negative values of q, one can see that there is not a solution until the radius of the circle is greater than $\pi/2$. Hence, the first TE mode does not propagate below a cutoff frequency (Eq. 4.3). As the electrical thickness of the dielectric (i.e. radius of the circle) increases, the circle intersects more branches of the tangent function, and hence more modes can propagate. For TM modes, there exists

a solution for all non-zero radii, demonstrating that for any dielectric slab with non-zero thickness and permittivity ϵ_r greater than one, at least one mode can propagate, i.e. there is no cutoff frequency for the first TM mode.

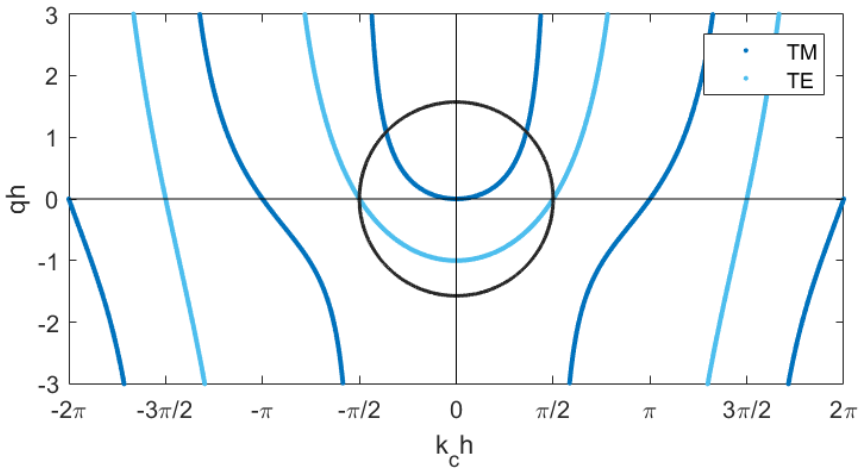

Figure 4.29: Graphical solution of the transcendental equation for the cutoff frequencies of the TM and TE grounded dielectric slab modes.

4.6.2 Appendix B: Dispersion relation of periodically patterned grounded dielectric slab modes

Figure 4.30(a) presents the dispersion relation of space harmonics of a periodically patterned grounded dielectric slab. Physically, the space harmonics should have a positive group velocity, since propagation of energy is away from the source. Fig. 4.30(b) presents these allowed space harmonics. Modes which fall in the the light cone, illustrated by the shaded region, can couple to free space. Hence, they are described as leaky waves. When the phase and

group velocities are of opposite sign, the waves are referred to as backward waves.

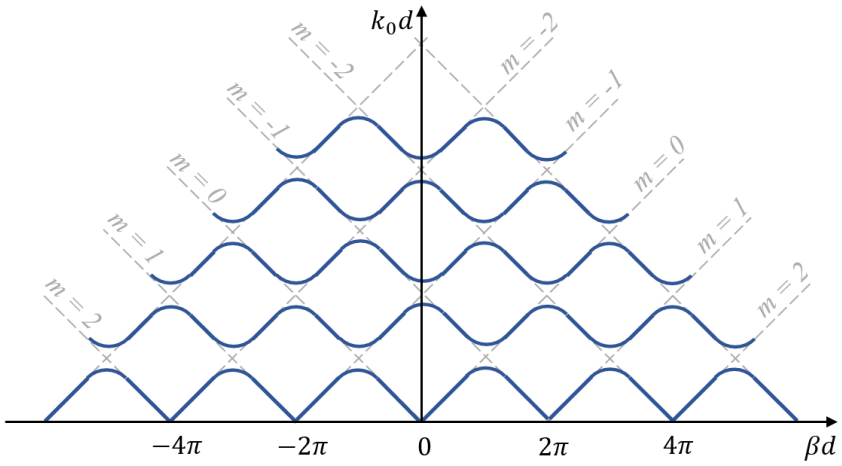

(a)

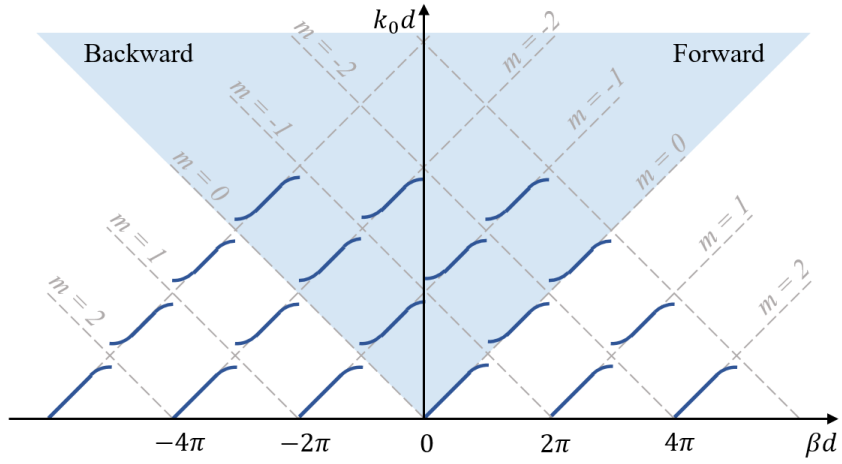

(b)

Figure 4.30: Dispersion relation of space harmonics (denoted by n) of a periodically patterned grounded dielectric slab. (a) Dispersion relation of all space harmonics. (b) Dispersion relation of space harmonics with positive group velocities only, i.e. for propagation of energy away from the source. The shaded region illustrates the light cone. Modes which fall in this region can couple to free space, and hence are described as leaky. When the phase and group velocities are of opposite sign (β is negative), the waves are referred to as backward waves.

4.6.3 Appendix C: Study of array dimensions

The dimensions of the period structure are fundamental in determining the propagation of the leaky wave and spectral properties of the ET [155]. Here, simulations of the structures with dielectric thicknesses 102 µm and 188 µm were carried out in CST Microwave Studio. The slit width is tuned to control the leakage of the mode, while the periodicity is tuned to ensure the ET frequency is approximately at the peak of the measurement system. Fig. 4.31 and 4.32 illustrate the spectral dependence and field decay along the structure on the slit width, respectively. It is evident that as the slit width is increased, the ET broadens towards lower frequencies, while the leakage per unit cell increases, hence the leaky wave propagates for longer along the corrugations before completely decaying.

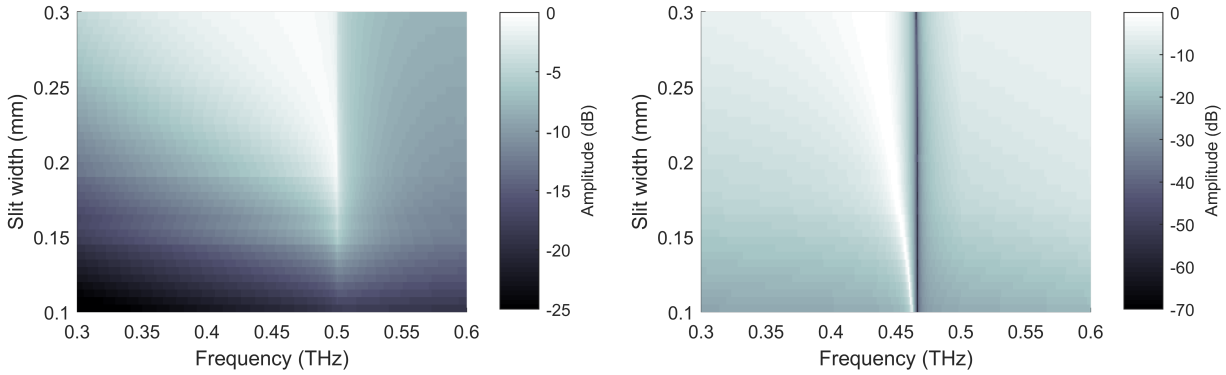

(a) (b)

Figure 4.31: Colour maps presenting the simulated spectral dependence of transmission on the slit width s for structures with dielectric thicknesses 102 µm (a) and 188 µm (b). Simulations were carried out in CST Microwave Studio using unit cell boundary conditions and Floquet ports. Note the different amplitude scales.

Fig 4.33 illustrates the spectral dependence on periodicity for structures with dielectric thicknesses 102 µm and 188 µm. It is evident that the ET frequency is highly dependent on the periodicity of the corrugations, with a shift towards lower frequencies for larger periods.

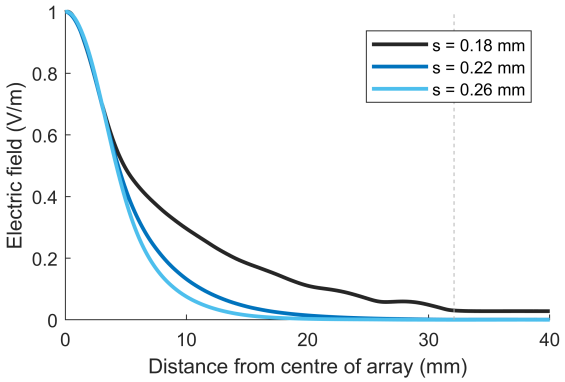

Figure 4.32: Normalised decay of the electric field from the centre of the structure with dielectric thickness 188 µm for different slit widths, simulated in CST Microwave Studio. The dashed line illustrates the truncation of the periodic region.

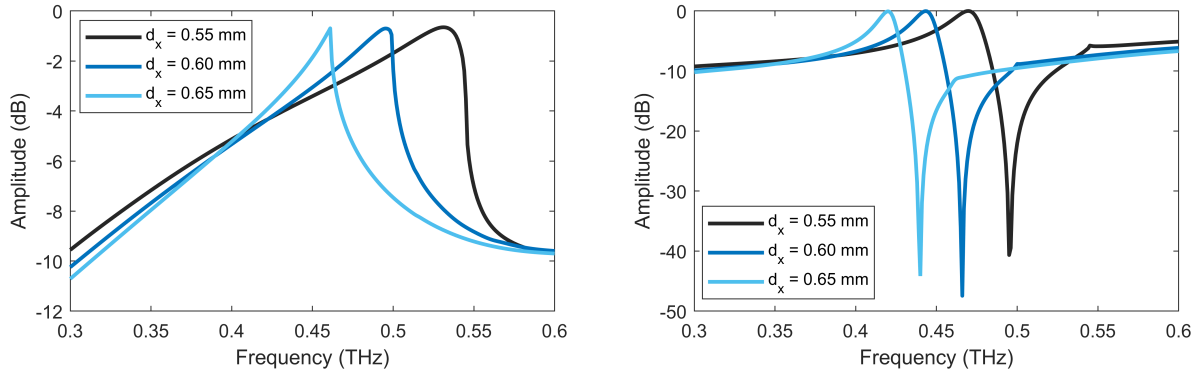

(a) (b)

Figure 4.33: Simulated spectral dependence of transmission on the structural periodicity d_x for structures with dielectric thicknesses 102 µm (a) and 188 µm (b). Simulations were carried out in CST Microwave Studio using unit cell boundary conditions and Floquet ports. Note the different amplitude scales.

4.6.4 Appendix D: Methods

Section 4.2 methods

Experimental details: All sample characterisation was done using the all fibre-coupled terahertz time-domain spectrometer TERA K15 with lock-in detection (with time constant 300 ms) from Menlo Systems. The waveforms were 261 ps in length, giving a spectral resolution of 4.8 GHz. The detector was mounted in a scatterometry type setup [34], where the detector could be rotated around the sample for angle-resolved measurements. Scans were taken for increasing angles in the H-plane (xz-plane) in steps of 1 deg up to 20 deg, 2.5 deg up to 40 deg and 5 deg up to 55 deg. The distance between the emitter and sample and sample and detector was $\sim$110 mm. Two setup configurations were used for the measurements: collimated (Fig. 4.34 (a)) and focused (Fig. 4.34 (b)). The collimated configuration provided a frequency dependent beam diameter ($2\omega_x$) of 7.8 mm at 0.5 THz at the sample position. It it worth noting that true collimation cannot be achieved with photoconductive antennas. Instead, a slightly diverging beam is produced. The focused configuration used TPX50 lenses with effective focal length 50 mm to focus the beam down to a beam diameter of 3.0 mm at the sample position. The field produced by the photoconductive antennas was vertically linearly polarised, aligned along the slits. It should be noted that use of lenses in the system may have caused degradation of the polarisation purity, which was not accounted for. A linear polariser along the beam path would increase the purity of the polarisation.

Simulation details: Simulations of semi-infinite and infinite arrays were undertaken in the transient and frequency solvers of CST Microwave Studio. In a number of the simulations, a two-dimensional Gaussian beam with frequency components from 0.05 - 1 THz was normally incident upon the sample. Top and bottom electric walls were defined and open (add space) boundary conditions were set in the x-axis. In the remaining simulations, the array was excited with a plane wave with normal and oblique (rotation around the y-axis).

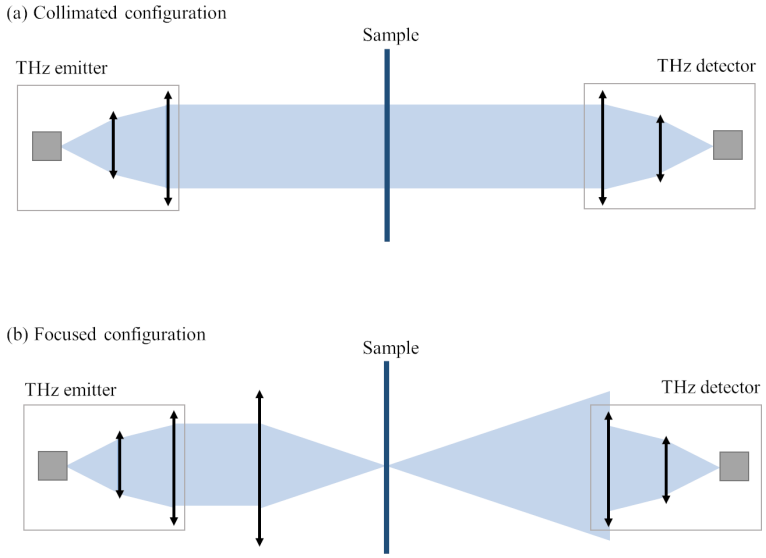

Figure 4.34: Schematic diagrams of the (a) collimated and (b) focused configurations of the TDS setup. Figure taken from [35].

Unit cell and periodic boundary conditions were used in the simulations used to produce Figs.4.12, 4.31 and 4.33.

The modelled metal had conductivity $\sigma = 3.56 \times 10^7$ S/m, except for the study of array dimensions, in which a perfect electric conductor is modelled. The PP dielectric had $\epsilon_r = 2.25$ and loss tangent $tan\delta = 10^3$, except for the study of array dimensions, in the dielectric is modelled as lossless.

Section 4.3 methods

Experimental details: Structures were characterised using the terahertz TDS TERA K15 with lock-in detection (with time constant 300 ms) from Menlo Systems. The waveforms were 156 ps in length, giving a spectral resolution of 8.0 GHz.

Simulation details: The eigenmode and transient solvers of CST Microwave Studio were used to simulate the E-field response of the surface wave platforms. For the eigenmode

solver calculations, periodic boundary conditions were implemented in the z-direction and electric and magnetic walls were defined in the y and x directions. Periodic boundary conditions were defined in the x- and z-directions for the hole and nail geometries. In the transient solver, the platforms were modelled as 2D structures, with razor blade excitation using discrete ports. Solver-defined open add space boundary conditions were set in y and z, with top and bottom magnetic walls in x. The metal was modelled as aluminium, with conductivity $\sigma = 3.56 \times 10^7$ S/m. For the surface roughness characterisation, the surface material was modelled as lossy.

Section 4.4 methods

Experimental details: The surface wave launcher was characterised using a Rohde and Schwarz vector network analyser (VNA) (10 MHz – 67 GHz). The frequency band of the VNA heads was 110 – 170 GHz. 1000 points were sampled and the intermediate frequency (IF) bandwidth was 1 kHz. Match, short, line calibration was performed.

Simulation details: The transient solver of CST Microwave Studio was used to simulate the E-field response of the surface wave launcher. In the transient solver, the platforms were modelled as 3D structures, with port excitation. Solver-defined open add space boundary conditions were set in y and z. The metal was modelled as aluminium, with conductivity $\sigma = 3.56 \times 10^7$ S/m.

Data Processing

The time-domain waveforms were subject to Hanning time-windowing before undergoing Fourier transformation. Calibration of measurements involved removing a free space on-axis measurement in the frequency-domain, taken on the day of measurement. The results

presented in Fig. 4.4 were subject to a low-pass filter. The spectrograms in Fig. 4.8 were calculated using short-time Fourier transformation with 98% overlap integral of the zero-padding length and 512 DFT points.

4.6.5 Appendix E: Fabrication details

The fabrication trials were realized on a state-of-art laser micro-processing system Lasea LS4. The system integrates a stack of five mechanical axes for orienting the workpiece in relation the laser beam, where the three linear stages have a position resolution of 0.25 µm, while the two rotary stages possess a position resolution of 45 µrad. The laser system is equipped with 3D optical scan head, allowing to achieve maximum laser beam stirring speeds of 5 m/s, while the achievable positional accuracy and precision are better than ±5 µm across the full range of scanning speeds. The laser system integrates an Yb-doped ultrafast (ps/fs) 10W laser sources from Amplitude Systemes that operates at a central wavelength of 1030 nm, and has a pulse duration in the range of 310 fs - 10 ps and maximum pulse repetition rate of 2 MHz. The utilization of the fs laser source in the experiments allows to minimise the heat-affected zone around the processed area and thus to reduce the thermally induced cracks and damages. At the same time the optical axes are employed to realize the required laser beam movements on the work-piece in order to benefit from the high scanning speeds of the optical galvanometer scanner (up to 5 m/s) and thus to obtain high machining throughputs. Table 4.4 summarizes the predetermined laser parameter settings used for the laser processing trials.

Laser parameter	Value
Power	7 W
Frequency	100 kHz
Pulse energy	70 µJ
Scanning speed	0.5 m/s
Pulse duration	310 fs
Laser beam polarisation	Circular
Hatch style	Random
Hatch pitch	4 µm
Ablation rate per layer	5 µm

Table 4.4: Optimized laser parameter settings used for the laser processing trials.

4.6.6 Appendix F: Profiling measurement details

Details are taken from the following thesis: Pavel N. Penchev, 'Reconfigurable laser micro-processing systems: Development of generic system-level tools for implementing modular laser micro-manufacturing platforms,' University of Birmingham, 2016 [193].

Measurement characterization of laser manufactured geometires in terms of accuracy, repeatability and reproducibility is performed with Focus Variation (FV) technology optical microscope, namely Alicona InfiniteFocus (IF) G5. It is equipped with x5, x10, x20, x50 objective and x100 lenses that provide lateral resolution of 3.52 µm, 1.76 µm, 0.88 µm, 0.64 µm and 0.44 µm and vertical resolution of 0.41 µm, 0.1 µm, 0.05 µm, 0.02 µm and 0.01 µm, respectively [194]. The system is equipped with three mechanical axes with travel range of 100 mm in X, Y and Z axes for measurement envelopes bigger than the field of view of the objective lenses. The measurement repeatability of the system is 0.12 µm, 0.03 µm, 0.01 µm, 0.003 µm and 0.001 µm for x5, x10, x20, x50 and x100 objective lenses, respectively. The

system also has a set of software tools (MeasureSuite), which allow analyses of measurement data both in terms of form and surface topography [195]. All analyses conform to the relevant ISO standards: profile roughness and surface texture analyses conform to ISO 4287/4288 [196] and 3D form analyses conform to the ISO 1101 [197].

Chapter Five

Conclusion and Outlook

From the macro- (mm) to the micro-scale (tens to hundreds of microns), this thesis has presented terahertz imaging and sensing for application to the biological world. Terahertz sensitivity to water content and the abundance of spectral fingerprints of biological molecules is exploited for prospective biological sensing and quantitative imaging. To achieve micro-scale sensitivity, efforts have been focused on enhancing interactions with samples through evanescent fields.

For single pixel imaging and sensing, use of TDS systems are widespread in the terahertz community. Effective use of any spectroscopic and imaging technique fundamentally relies on knowledge of the parameters of the excitation, such as beam profile and polarisation. Chapter 2 laid the foundations for terahertz imaging and sensing through a rigorous beam characterisation of a commercial all fiber-coupled TDS system in collimated configuration. Profiling techniques included pinhole-only scanning, simultaneous pinhole and detector scanning (with and without a TPX lens), detector scanning without a pinhole or TPX lens and the knife-edge method, complemented by stepwise ASM simulations. Current assumptions of the beam profile reported in the literature were challenged, such as the beam Gaussianity and asymmetry, a result of the shortfalls of standard beam profiling technique. For exclusive

consideration of the central lobe, one could assume a Gaussian distribution. In this instance, the frequency-dependent beam waist ranged from 8.4 mm to 2.8 mm at 0.25 THz to 1 THz. Cross-polar measurements revealed a non-negligible orthogonal component of -13.0 dB to -20.6 dB at 0.25 THz to 1 THz. As the core spectroscopic tool used throughout this thesis, the characterisation of the TDS system, including the beam profile and polarisation purity, crucially paved the way for informed imaging and sensing. Knowledge of these defects is fundamental for effective use of the TDS system, for when excitation of materials and structures is heavily dependent on profile and polarisation. This work built a platform not only for this project, but for TDS studies in the Metamaterials Group at the University of Birmingham and the wider terahertz TDS community.

In Chapter 3, attention was turned to the extraction of quantitative information from images, through the development of several algorithms, to reliably retrieve the dielectric properties of complex multilayer biological samples. For materials with high water content, such as biological samples, large absorption of terahertz radiation make reflection measurements necessary. Reflection measurements rely heavily on two factors for accurate retrieval of the material dielectric properties: (i) knowledge of the sample thickness and (ii) a sample thickness large enough to enable reflected pulses to be resolvable in time. These experimental challenges were addressed through the development of a hybrid Kramers-Kronig Fabry-Pérot modelling algorithm. The unique combination of the Kramers-Kronig and Fabry-Pérot modelling offered great versatility for application to complex multilayer samples, while the reduced computational complexity over existing modelling approaches allowed for easier implementation. Its success was demonstrated through application to TDS measurements of HO bone samples, where dielectric mapping was used for prospective disease detection. This was extended to hydration mapping of the bone samples, whereby the temperature dependent behaviour of water was used as a sensing fingerprint.

These retrieval processes provided a base for developing sensitive, subwavelength

imaging and sensing techniques through evanescent fields, improving upon standard TDS methods. Future work will involve increasing generality of these algorithms for application to multilayer biological samples of increased complexity. Increased versatility promises increasing value to the Birmingham group, and indeed the wider community, for complex dielectric retrieval, improving practicality for prospective use in a clinical environment.

The dimensional mismatch between micrometer biological objects and terahertz wavelengths presents a challenge for observing the micro-world from a terahertz perspective. Chapter 4 illustrates methods of overcoming this through enhancing fields and sensing, stemming from the field of metamaterials and plasmonics. Here, with the knowledge of the actual excitation region from Chapter 2, highly efficient and broadband field coupling to a surface wave structure was demonstrated, alongside investigations of evanescent field mechanisms.

A rigorous study of the design, behaviour and excitation of surface waves was presented. The development of surface waves in the form of leaky waves was studied through analytical work, simulations and TDS measurements, illustrating the importance of surface wave spatial distribution and energy transport for sensing application through monitoring ET of the field. This was of significant contribution to the community as it unequivocally revealed underlying physical phenomena and provided the necessary framework to design practical, high-performance quasi-optical sensors.

The tunability of surface waves was exploited in Section 4.3 for manipulation of evanescent field confinement and spacial distribution through geometric design. Corrugated surfaces with different patterns were excited using the TDS system. The importance of knowledge of the surface wave attenuation for sensing and communication application was highlighted through experimental and simulated measurements, challenging common surface roughness modelling techniques. Sensing measurements were undertaken through the introduction of powdered lactose samples, with results demonstrating promising sensitivities,

but limited by inefficient energy coupling. Inspired by the microwave regime, Section 4.4 focused on enhancing coupling efficiencies provided by standard coupling approaches. Coupling structures were designed and fabricated, achieving efficiencies of 99% through VNA excitation, a vast improvement on the 5% achieved through standard razor-edge coupling techniques. The highly confined fields supported by these structures, together with the highly efficient coupling mechanism, provides great promise for sensitive, portable, on-chip sensing devices and tunable biological liquid detection, vastly improving on standard free-space approaches. Future work aims to develop this sensing technique for both bulk and microfluidic biological sensing. Each sensing platform developed in this project will be characterised regarding sensitivity and practicality for different applications from diagnostics to liquid and powdered molecular sensing, with the hope of contributing to medical, biological and pharmaceutical fields.

References

[1] C. Sirtori. "Applied physics: bridge for the terahertz gap". In: *Nature* 417 (2002), pp. 132–133.

[2] T.W. Crowe et al. "Opening the terahertz window with integrated diode circuits. In IEEE Journal of Solid-State Circuits". In: *IEEE Journal of Solid-State Circuits* 40 (2005), pp. 2104–2109.

[3] J.M. Chamberlain and R. Miles. *New Directions in Terahertz Technology*. Springer Netherlands, 1997. ISBN: 978-94-011-5760-5.

[4] R. Colombelli et al. "Long-infrared InAs-based quantum cascade lasers operating at 291 K (λ=19 μm) with metal-metal resonators". In: *Applied Physics Letters* 78 (2001), pp. 2620–2622.

[5] C. Fattinger and D. Grischkowsky. "Point source terahertz optics". In: *Appl. Phys. Lett.* 53 (1988), p. 1480.

[6] T. Kleine-Ostmann and T. Nagatsuma. "A review on terahertz communications research". In: *Journal of Infrared, Millimeter, and Terahertz Waves* 32 (2011), pp. 143–171.

[7] G. P. Gallerano and S. Biedron. "Overview of terahertz radiation sources". In: *Proceedings of the 2004 FEL Conference* (2004), pp. 216–221.

[8] R. A. Lewis. "A review of terahertz sources". In: *Journal of Physics D: Applied Physics* 47.37 (2014), p. 374001.

[9] A. Khalid et al. "A planar Gunn diode operating above 100 GHz". In: *Journal of Physics D: Applied Physics* 28.10 (2007), pp. 849–851.

[10] A. Acharyya and J. P. Banerjee. "Potentiality of IMPATT Devices as Terahertz Source: An Avalanche Response Time-based Approach to Determine the Upper Cut-off Frequency Limits". In: *IETE Journal of Research* 59.2 (2013), p. 118.

[11] J.-H. Son. *Terahertz Biomedical Science and Technology*. CRC Press, 2014. 377 pp. ISBN: 9781466570443.

[12] D. D. Arnone et al. "Applications of terahertz (THz) technology to medical imaging". In: *International Society for Optics and Photonics* 3828 (2013), p. 209.

[13] K. Humphreys et al. "Medical applications of terahertz imaging: a review of current technology and potential applications in biomedical engineering". In: *26th Annual International Conference of the IEEE Engineering in Medicine and Biology Society* 3 (2004), pp. 1302–1305.

[14] P. F. Taday et al. "Applications of terahertz spectroscopy to pharmaceutical sciences". In: *Philos. Trans. R. Soc. Lond. A, Math. Phys. Eng. Sci.* 362 (2004), p. 351.

[15] D. Markl et al. "Characterisation of pore structures of pharmaceutical tablets: A review". In: *International Journal of Pharmaceutics* 538 (2018), pp. 188–214.

[16] S. L. Dexheimer. *Terahertz spectroscopy : principles and applications*. CRC Press/Taylor & Francis, 2008. 360 pp. ISBN: 9780849375255.

[17] D. Zimdars et al. "Large area terahertz imaging and non-destructive evaluation applications". In: *Philos. Trans. R. Soc. Lond. A, Math. Phys. Eng. Sci.* 48 (2006), p. 537.

[18] D. M. Mittleman, R. H. J., and M. C. Nuss. "T-Ray Imaging". In: *IEEE Journal of Selected Topics in Quantum Electronics* 2.3 (1996), pp. 679–692.

[19] X. Yang et al. "Biomedical applications of terahertz spectroscopy and imaging". In: *Trends in Biotechnology* 34 (2011), pp. 810–824.

[20] P. Uhd Jepsen, D. G. Cooke, and M. Koch. "Terahertz spectroscopy and imaging – Modern techniques and applications". In: *Laser and Photonics Reviews* 5 (2011), p. 124.

[21] O. P. Cherkasova et al. "Terahertz spectroscopy of biological molecules". In: *Radiophysics and Quantum Electronics* 52 (2009), p. 576.

[22] L. Thrane et al. "THz reflection spectroscopy of liquid water". In: *Chemical Physics Letters* 240 (1996), pp. 330–333.

[23] A. J. Fitzgerald et al. "Terahertz pulsed imaging for medical applications". In: *World Congress on Physics and Biomedical Engineering* (2003).

[24] C. M. Ciesla et al. "Biomedical applications of terahertz pulse imaging". In: *Proceedings of SPIE* 3934 (2020), pp. 73–81.

[25] L. Wang. "Terahertz Imaging for Breast Cancer Detection". In: *Sensors* 21.19 (2021), p. 6465.

[26] C. D. Benzant. "Applications of THz pulses in semiconductor relaxation and biomedical imaging studies". In: *PhD Thesis: University of Nottingham* (2000).

[27] M-A. Brun et al. "Terahertz imaging applied to cancer diagnosis". In: *Physics in Medicine & Biology* 55.16 (2010), pp. 1413–1421.

[28] T.C. Bowman, M. El-Shenawee, and L.K. Campbell. "Terahertz Imaging of Excised Breast Tumor Tissue on Paraffin Sections". In: *IEEE Transactions on Antennas and Propagation* 63.5 (2015), pp. 2088–2097.

[29] F.de Fornel. *Evanescent Waves: From Newtonian Optics to Atomic Optics*. Springer, 2001. ISBN: 978-3-540-65845-0.

[30] I. Jáuregui-López et al. "THz Sensing With Anomalous Extraordinary Optical Transmission Hole Arrays". In: *Sensors* 18 (2018), p. 3848.

[31] A. Rogers. "Distributed optical-fibre sensing". In: *Measurement Science and Technology* 10 (1999).

[32] P. Arroyo Huidobro et al. *Spoof Surface Plasmon Metamaterials*. Cambridge University Press, 2018. ISBN: 9781108553445.

[33] M.H. Feng et al. "Broadband and high-efficiency conversion from guided waves to spoof surface plasmon polaritons". In: *Laser and Photonics Reviews* 8 (2014).

[34] M. Camacho et al. "Far-field and near-field physics of extraordinary THz transmitting hole-array antennas". In: *IEEE Transactions on Antennas Propagation* 67 (2019), pp. 6029–6038.

[35] S. Freer et al. "Revealing the underlying mechanisms behind TE extraordinary THz transmission". In: *Photonics Research* 8 (4 2020), pp. 430–439.

[36] K. Nallappan H. Guerboukha and M. Skorobogatiy. "Toward real-time terahertz imaging". In: *Advances in Optics and Photonics* 10 (2018), pp. 843–938.

[37] E. Y. Chao et al. "Biomechanical considerations of fracture treatment and bone quality maintenance in elderly patients and patients with osteoporosis". In: *Clinical orthopaedics and related research* 425 (2004), pp. 12–25.

[38] M. R. Stringer et al. "The analysis of human cortical bone by terahertz time-domain spectroscopy". In: *Physics in Medicine and Biology* 50 (2005), p. 3211.

[39] M. Bessou et al. "Three-dimensional terahertz computed tomography of human bones". In: *Applied Optics* 51.28 (2012), pp. 6738–6744.

[40] L. Duvillaret, F. Garet, and J. L. Coutaz. "A reliable method for extraction of material parameters in terahertz time-domain spectroscopy". In: *IEEE Journal on Selected Topics in Quantum Electronics* 2 (1996), pp. 739–745.

[41] W. Withayachumnankul et al. "Direct Fabry-Pérot Effect Removal". In: *Fluctuation and Noise Letters* 6 (2006), pp. L227–L239.

[42] I. Pupeza, R. Wilk, and M. Koch. "Highly accurate optical material parameter determination with THz time-domain spectroscopy". In: *Optics Express* 15 (2007).

[43] I. Jáuregui-López et al. "THz sensing with anomalous extraordinary optical transmission hole arrays". In: *Sensors* 18 (2018), p. 3848.

[44] M. Beruete and I. Jáuregui-López. "Terahertz Sensing Based on Metasurfaces". In: *Advanced Optical Materials* 8 (2020), p. 1900721.

[45] M. Navarro-Cía et al. "Terahertz imaging of sub-wavelength particles with Zenneck surface waves". In: *Applied Physics Letters* 103 (22 2013), p. 221103.

[46] R. S. Elliott. "On the theory of corrugated plane surfaces". In: *Transactions of the IRE Professional Group on Antennas and Propagation* 2.2 (1954), pp. 71–81.

[47] G. Carpintero et al. *Semiconductor Terahertz Technology: Devices and Systems at Room Temperature Operation*. John Wiley & Sons, Ltd, 2015.

[48] J. Coutaz, F. Garet, and V. Wallace. *Principles of Terahertz Time-domain Spectroscopy*. Pan Stanford Publishing, 2018.

[49] B. B. Hu and M. C. Nuss. "Imaging with terahertz waves". In: *Optics Letters* 20 (1995), p. 1716.

[50] A. Gorodetsky et al. "Physics of the conical broadband terahertz emission from two-color laser-induced plasma filaments". In: *Physical Review A* 89 (2014), p. 033838.

[51] N. V. Petrov et al. “Application of Terahertz Pulse Time-Domain Holography for Phase Imaging”. In: *IEEE Transactions on Terahertz Science and Technology* 6 (2016), pp. 464–472.

[52] W. L. Chan et al. “A single-pixel terahertz imaging system based on compressed sensing”. In: *Applied Physics Letters* 93 (2018), p. 121105.

[53] R. I. Stantchev et al. “Noninvasive, near-field terahertz imaging of hidden objects using a single-pixel detector”. In: *Science Advances* 2 (2016), e1600190.

[54] M. Naftaly. *Terahertz Metrology*. Artech House, 2014.

[55] P. F. Goldsmith. *Quasioptical Systems: Gaussian Beam Quasioptical Propogation and Applications*. Wiley-IEEE Press, 1998.

[56] P. U. Jepsen and S. R. Keiding. “Radiation patterns from lens-coupled terahertz antennas”. In: *Photonics Research* 20 (1995), pp. 807–809.

[57] F. Garet et al. “Evidence of frequency-dependent Thz beam polarization in time-domain spectroscopy”. In: *Proceedings of SPIE–the international society for optical engineering* 3617 (1999), pp. 30–37.

[58] J. Van Rudd, Jon L. Johnson, and Daniel M. Mittleman. “Cross-polarized angular emission patterns from lens-coupled terahertz antennas”. In: *J. Opt. Soc. Am. B* 18.10 (2001), pp. 1524–1533.

[59] J. V. Rudd and D. M. Mittleman. “The influence of substrate lens design in terahertz time-domain spectroscopy”. In: *Journal of the Optical Society of America B* 19 (2002), pp. 319–329.

[60] B. Globisch et al. “Fiber-coupled transceiver for terahertz reflection measurements with a 4.5 THz bandwidth”. In: *Journal of the Optical Society of America B* 41 (2016), pp. 5262–5265.

[61] M. T. Reiten, S. A. Harmon, and R. A. Cheville. "Terahertz beam propagation measured through three-dimensional amplitude profile determination". In: *Journal of the Optical Society of America B* 20 (2003), pp. 2215–2225.

[62] J. F. Molloy, M. Naftaly, and R. A. Dudley. "Characterization of terahertz beam profile and propagation". In: *IEEE Journal of Selected Topics in Quantum Electronics* 19 (2013).

[63] J. Klier et al. "Influence of Substrate Material on Radiation Characteristics of THz Photoconductive Emitters". In: *International Journal of Antennas and Propagation* 2015 (2015), p. 540175.

[64] A. Garufo et al. "Norton equivalent circuit for pulsed photoconductive antennas—part ii: Experimental validation". In: *IEEE Transactions on Antennas and Propagation* 66.4 (2018), pp. 1646–1659.

[65] K. Elmabruk et al. "Time-Domain Characterization of the Radiation Pattern of the Terahertz Photoconductive Antennas". In: *Journal of Infrared, Millimeter, and Terahertz Waves* 40.6 (2019), pp. 595–605.

[66] M. A. Báez-Chorro, M. Usó-Izquierdo, and B. Vidal. "Accurate Beam Profile Characterization in THz Transmission Imaging Systems". In: *IEEE Transactions on Terahertz Science and Technology* 11.5 (2021), pp. 577–582.

[67] R. J. B. Dietz et al. "64 μW pulsed terahertz emission from growth optimized InGaAs/InAlAs heterostructures with separated photoconductive and trapping regions". In: *Applied Physics Letters* 103.6 (2013), p. 061103.

[68] B. Globisch et al. "Carrier dynamics in Beryllium doped low-temperature-grown InGaAs/InAlAs". In: *Applied Physics Letters* 104.17 (2014), p. 172103.

[69] M. Navarro-Cía et al. "Modes in silver-iodide-lined hollow metallic waveguides mapped by terahertz near-field time-domain microscopy". In: *Journal of the Optical Society of America* 30.1 (2013), p. 127.

[70] M. Navarro-Cía, M. Vitiello, and C. Bledt. "Terahertz wave transmission in flexible polystyrene-lined hollow metallic waveguides for the 2.5-5 THz band". In: *Optics Express* 21.20 (2013), pp. 23748–23755.

[71] M. Navarro-Cía et al. "Silver-Coated Teflon Tubes for Waveguiding at 1–2 THz". In: *Journal of Infrared, Millimeter, and Terahertz Waves* 36.6 (2015), pp. 542–555.

[72] A. Podzorov, A. Wojdyla, and G. Gallot. "Beam waist measurement for terahertz time-domain spectroscopy Experiments". In: *Optics Letters* 35.7 (2010), pp. 901–903.

[73] A. J. Seeds et al. "Coherent terahertz photonics". In: *Optics Express* 21.19 (2013), pp. 22988–23000.

[74] M. J. Gans. "Cross Polarization in Reflector-Type Beam Waveguides and Antennas". In: *The Bell System Technical Journal* 55.3 (1976), pp. 289–316.

[75] A. Neto et al. "Demonstration of the leaky lens antenna at submillimeter wavelengths". In: *IEEE Transactions on Terahertz Science and Technology* 4.1 (2014), pp. 26–32.

[76] C. Cappellin et al. "Detailed design and RF analysis of a scatterometer for material characterization in the 50–750 GHz range". In: *12th European Conference on Antennas and Propagation (EuCAP 2018)* (2018), pp. 1–5.

[77] M. Neshat and N. P. Armitage. "Terahertz time-domain spectroscopic ellipsometry: instrumentation and calibration". In: *Optics Express* 20.27 (2012), pp. 29063–29075.

[78] C. D. Mosley et al. "Terahertz spectroscopy of anisotropic materials using beams with rotatable polarization". In: *Scientific Reports* 7.1 (2017), pp. 1–9.

[79] S. A. Kuznetsov et al. "Planar Holographic Metasurfaces for Terahertz Focusing". In: *Scientific Reports* 5 (2015), p. 7738.

[80] W. Y. Kim et al. "Graphene-ferroelectric metadevices for nonvolatile memory and reconfigurable logic-gate operations". In: *Nature Communications* 7 (2016), pp. 1–6.

[81] T.-T. Kim et al. "Electrical access to critical coupling of circularly polarized waves in graphene chiral metamaterials". In: *Science Advances* 3.9 (2017), e1701377.

[82] D. Wang et al. "Photonic Weyl points due to broken time-reversal symmetry in magnetized semiconductor". In: *Nature Physics* 15.11 (2019), pp. 1150–1155.

[83] A. V. Belashov et al. "Effect of object thickness on ultrashort pulse diffraction". In: *Applied Optics* 58.34 (2019), p. 9434.

[84] C.-T. Tai and C. S. Pereira. "An approximate formula for calculating the directivity of an antenna". In: *Applied Optics* 24.2 (1976), pp. 235–236.

[85] K. Matsushima and T. Shimobaba. "Band-limited angular spectrum method for numerical simulation of free-space propagation in far and near fields". In: *Optics Express* 17.22 (2009), p. 19662.

[86] J. Magnes et al. "Quantitative and qualitative study of gaussian beam visualization techniques". In: (2006). arXiv: 0605102 [physics].

[87] S. Freer et al. "Temperature Dependent Hyperspectral Terahertz Imaging of Human Bone for Disease Diagnosis". In: *Biomedical Optics Express* 12.8 (2021), pp. 4807–4820.

[88] P. Jepsen, D. G. Cooke, and M. Koch. "Terahertz spectroscopy and imaging – Modern techniques and applications". In: *Laser and Photonics Reviews* 5 (2011), p. 124.

[89] C. Yu et al. "The potential of terahertz imaging for cancer diagnosis: A review of investigations to date". In: *Quantitative Imaging in Medicine and Surgery* 2 (2012), p. 33.

[90] S. Sy et al. "Terahertz spectroscopy of liver cirrhosis: investigating the origin of contrast". In: *Physics in Medicine and Biology* 55 (2010), p. 7587.

[91] P. Knobloch et al. "Medical THz imaging: an investigation of histo-pathological samples". In: *Physics in Medicine and Biology* 47.21 (2002), pp. 3875–3884.

[92] B. A. Knyazev et al. "Using of terahertz radiation for monitoring of senile osteoporosis development". In: *IRMMW-THz2007 - Conference Digest of the Joint 32nd International Conference on Infrared and Millimetre Waves, and 15th International Conference on Terahertz Electronics* (2007), pp. 563–564.

[93] M. Granke, M. D. Does, and J. S. Nyman. "The Role of Water Compartments in the Material Properties of Cortical Bone". In: *Calcif Tissue International* 97.3 (2015), pp. 292–307.

[94] V. Lucarini et al. "Detection and correction of the misplacement error in terahertz spectroscopy by application of singly subtractive Kramers-Kronig relations". In: *Physical Review B - Condensed Matter and Materials Physics* 72 (2005).

[95] E. M. Vartiainen et al. "Numerical phase correction method for terahertz time-domain reflection spectroscopy". In: *Journal of Applied Physics* 96 (2004), pp. 4171–4175.

[96] Dayou Liu, Tianqi Lu, and Feng Qi. "A Reliable Method for Removing Fabry-Perot Effect in Material Characterization with Terahertz Time-Domain Spectroscopy". In: *IEEE Transactions on Terahertz Science and Technology* 10 (2020), pp. 443–452.

[97] M. Naftaly. *Terahertz Metrology*. Artech House, 2015. 360 pp. ISBN: 978-1608077762.

[98] S. Nashima et al. "Measurement of optical properties of highly doped silicon by terahertz time domain reflection spectroscopy". In: *Applied Physics Letters* 79 (2001), p. 3923.

[99] M. Khazan, R. Meissner, and I. Wilke. "Convertible transmission-reflection time-domain terahertz spectrometer". In: *Review of Scientific Instruments* 72 (2001), p. 3427.

[100] A. Pashkin et al. "Phase-sensitive time-domain terahertz reflection spectroscopy". In: *Review of Scientific Instruments* 74 (2003), p. 4711.

[101] K. E. Peiponen, E. M. Vartiainen, and T. Asakura. *Dispersion, Complex Analysis and Optical Spectroscopy*. Springer, Berlin, 1999. ISBN: 978-3-540-64522-1.

[102] John S. Toll. "Causality and the Dispersion Relation: Logical Foundations". In: *Phys. Rev.* 104 (6 1956), pp. 1760–1770.

[103] H. M. Nussenzveig. *Causality and Dispersion Relations*. Academic Press, New York, 1972. ISBN: 9780124110793.

[104] F. Bassani and V. Lucarini. "Asymptotic behaviour and general properties of harmonic generation susceptibilities". In: *The European Physical Journal B - Condensed Matter and Complex Systems* 17 (2000), pp. 567–573.

[105] K. E. Peiponen et al. "Kramers-Kronig relations and sum rules in nonlinear optical spectroscopy". In: *Applied Spectroscopy* 58 (2004), pp. 499–509.

[106] V. Lucarini et al. "Dispersion theory and sum rules in linear and nonlinear optics". In: *La Rivista del Nuovo Cimento* 26 (2003), p. 1.

[107] R. Nitsche and T. Fritz. "Determination of model-free Kramers-Kronig consistent optical constants of thin absorbing films from just one spectral measurement: Application to organic semiconductors". In: *Physical Review B* 70 (2004), p. 195432.

[108] V. Lucarini, Saarinen J. J., and K. E. Peiponen. "Multiply subtractive Kramers–Krönig relations for arbitrary-order harmonic generation susceptibilities". In: *Optics Communications* 218 (2003), pp. 409–419.

[109] V. Lucarini et al. *Kramers-Kronig Relations in Optical Materials Research*. Springer-Verlag Berlin Heidelberg, 2005. ISBN: 978-3-540-27316-5.

[110] M. Bernier et al. "Accurate Characterization of Resonant Samples in the Terahertz Regime Through a Technique Combining Time-Domain Spectroscopy and Kramers–Kronig Analysis". In: *IEEE Trans. Terahertz Sci. Technol.* 6.3 (2016), pp. 442–450.

[111] M. Scheller, C. Jansen, and M. Koch. "Analyzing sub-100-μm samples with transmission terahertz time domain spectroscopy". In: *Optics Communications* 282 (2009), pp. 1304–1306.

[112] R. Fastampa, L. Pilozzi, and M. Missori. "Cancellation of Fabry-Perot interference effects in terahertz time-domain spectroscopy of optically thin samples". In: *Physical Review A* 95.6 (2017), pp. 1–6.

[113] R. Peretti et al. "THz-TDS Time-Trace Analysis for the Extraction of Material and Metamaterial Parameters". In: *IEEE Transactions on Terahertz Science and Technology* 9.2 (2019), pp. 136–149.

[114] P. Uhd Jepsen, U. Møller, and H. Merbold. "Investigation of aqueous alcohol and sugar solutions with reflection terahertz time-domain spectroscopy". In: *Optics Express* 15 (2007), pp. 14717–14737.

[115] S. Freer, A. Gorodetsky, and M. Navarro-Cia. "Beam Profiling of a Commercial Lens-Assisted Terahertz Time Domain Spectrometer". In: *IEEE Transactions on Terahertz Science and Technology* 11.1 (2021), pp. 90–100.

[116] E. E. Wilson et al. "Three Structural Roles for Water in Bone Observed by Solid-State NMR". In: *Biophysical Journal* 90.10 (2006), pp. 3722–3731.

[117] Jun Zhou et al. "Temperature dependent optical and dielectric properties of liquid water studied by terahertz time-domain spectroscopy". In: *AIP Advances* 9.035346 (2019).

[118] B. L. Yu et al. "Reorientation of the H2O cage studied by terahertz time-domain spectroscopy". In: *Applied Physics Letters* 86.061912 (2005).

[119] W.J. Ellison. "Permittivity of Pure Water, at Standard Atmospheric Pressure, over the Frequency Range 0–25THz and the Temperature Range 0–100∘C". In: *Journal of Physical Chemistry Reference Data* 36 (2007), pp. 1–18.

[120] S. Carvalho et al. “Glucose diffusion in colorectal mucosa - A comparative study between normal and cancer tissues”. In: *Journal of Biomedical Optics* 22.9 (2017), p. 91506.

[121] S. Pauklin and L. Vallier. “The cell-cycle state of stem cells determines cell fate propensity”. In: *Cell* 155 (2013), pp. 135–147.

[122] S. Tripathi et al. “Morphology of human sweat ducts observed by optical coherence tomography and their frequency of resonance in the terahertz frequency region”. In: *Scientific Reports* 5.9071 (2015).

[123] A. Menikh et al. “Terahertz Biosensing Technology: Frontiers and Progress”. In: *Journal of ChemPhysChem* 3.8 (2002), pp. 655–658.

[124] J. Homola. “Optical fiber sensor based on surface plasmon excitation”. In: *Journal of Sensors and Actuators A: Physical* 29 (1995), pp. 401–405.

[125] T. Kalkbrenner et al. “A single gold particle as a probe for apertureless SNOM”. In: *Journal of microscopy* 202 (2001).

[126] SA. Maier et al. “Local detection of electromagnetic energy transport below the diffraction limit in metal nanoparticle plasmon waveguides”. In: *Nature Materials* 2 (2013).

[127] M. Mitsushio, K. Miyashita, and M. Higo. “Sensor properties and surface characterization of the metal-deposited SPR optical fiber sensors with Au, Ag, Cu, and Al”. In: *Journal of Sensors and Actuators A: Physical* 125 (2006), pp. 296–303.

[128] V.V. Gerasimov et al. “Growth of terahertz surface plasmon propagation length due to thin-layer dielectric coating”. In: *Journal of the Optical Society of America B* 33 (2016), pp. 2196–2203.

[129] S. Freer et al. “Study of Leaky Waves Responsible for Terahertz TE Extroardinary Transmission”. In: *12th UK-Europe-China Workshop on Millimeter Waves and Terahertz Technologies (UCMMT)* (2019), pp. 1–4.

[130] R. E. Betzig. “Nondestructive optical imaging of surfaces with 500 angstrom resolution”. PhD thesis. Cornell University, 1988.

[131] A. Lewis R. E. Betzig et al. “Near-field scanning optical microscopy (NSOM): Development and Biophysical Applications”. In: *Biophysical Journal* 49 (1986), pp. 269–279.

[132] H. F. Ghaemi et al. “Surface plasmons enhance optical transmission through subwavelength holes”. In: *Physical Review B* 58.11 (1998), pp. 6779–6782.

[133] T. Ebbesen et al. “Extraordinary optical transmission through sub-wavelength hole arrays”. In: *Nature* 391 (1998), pp. 667–669.

[134] F. J. Garcia-Vidal et al. “Light passing through subwavelength apertures”. In: *Reviews of Modern Physics* 82 (2010), pp. 729–787.

[135] M. Beruete et al. “Enhanced millimeter wave transmission through quasioptical subwavelength perforated plates”. In: *IEEE Transactions on Antennas and Propagation* 53.6 (2005), pp. 1897–1903.

[136] F. Medina, F. Mesa, and R. Marqués. “Extraordinary transmission through arrays of electrically small holes from a circuit theory perspective”. In: *IEEE Transactions on Microwave Theory Technology* 56.12 (2008), pp. 3108–3120.

[137] D. R. Jackson et al. “Beaming of light at broadside through a subwavelength hole: leaky wave model and open stopband effect”. In: *Radio Science* 40 (2005), RS6510.

[138] M. Beruete et al. “Enhanced millimeter-wave transmission through subwavelength hole arrays”. In: *Optics Letters* 29 (2004), pp. 2500–2502.

[139] A. Ishimaru. *Electromagnetic Wave Propagation, Radiation, and Scattering*. Prentice Hall, 1991. ISBN: 9781118098813.

[140] E. Hendry, A. P. Hibbins, and J. R. Sambles. "Importance of diffraction in determining the dispersion of designer surface plasmons". In: *Physical Review B* 78 (2008), p. 235426.

[141] V. O. Byelobrov et al. "Periodicity Matters: Grating or lattice resonances in the scattering by sparse arrays of subwavelength strips and wires." In: *IEEE Antennas and Propagation Magazine* 57.6 (2015), pp. 34–45.

[142] R. Ulrich, ed. *Proceedings of the 1974 The Symposium on Optical Acoustical Micro-Electronics*. New York, 1975.

[143] V. Lomakin and E. Michielssen. "Enhanced transmission through metallic plates perforated by arrays of subwavelength holes and sandwiched between dielectric slabs". In: *Physical Review B* 71 (2005), p. 235117.

[144] A. Hessel and A. Oliner. "A New Theory of Wood's Anomalies on Optical Gratings". In: *Applied Optics* 4 (1965), pp. 1275–1297.

[145] V. Lomakin and E. Michielssen. "Transmission of transient plane waves through perfect electrically conducting plates perforated by periodic arrays of subwavelength holes". In: *IEEE Transactions on Antennas and Propagation* 54 (2006), pp. 970–984.

[146] A. Oliner. "Radiating periodic structures: analysis in terms of k vs. β diagrams". In: *Short Course on Microwave Field and Network Techniques* (1963), pp. 1–32.

[147] S. G. Rodrigo, F. de Leon-Perez, and L. Martin-Moreno. "Extraordinary Optical Transmission: Fundamentals and Applications". In: *Proceedings of the IEEE* 104.12 (2016), p. 22882306.

[148] M. Beruete et al. "Quasioptical polarizer based on self-complementary sub-wavelength hole arrays". In: *IEEE Microwave and Wireless Components Letters* 17.12 (2007), p. 834836.

[149] V. Torres et al. "Compact dual-band terahertz quarter-wave plate metasurface". In: *IEEE Photonics Technology Letters* 26.16 (2014), p. 16791682.

[150] J. B. Pendry, L. Martín-Moreno, and F. J. García-Vidal. "Mimicking surface plasmons with structured surfaces". In: *Science* 305 (2004), pp. 847–848.

[151] M. Beruete et al. "Extraordinary transmission and left-handed propagation in miniaturized stacks of doubly periodic subwavelength hole arrays". In: *Optics Express* 15 (2007), pp. 1107–1114.

[152] M. Navarro-Cía et al. "Negative group delay through subwavelength hole arrays". In: *Physical Review B* 84 (7 2011), p. 075151.

[153] David M. Pozar. *Microwave Engineering*. John Wiley & Sons, 1997. ISBN: 0471170968.

[154] A.Y Nikitin, F. J. García-Vidal, and L. Martín-Moreno. "Enhanced optical transmission, beaming and focusing through a subwavelength slit under excitation of dielectric waveguide modes". In: *Journal of Optics A: Pure and Applied Optics* 11.12 (2009), p. 125702.

[155] M. Navarro-Cía, M. Beruete, and M. Sorolla. "Numerical and experimental parametric analysis of anomalous enhanced transmission through subwavelength apertures". In: *Metamaterials* 5 (2 2011), pp. 125–134.

[156] S. A. Kuznetsov et al. "Regular and anomalous extraordinary optical transmission at the THz-gap". In: *Optics Express* 17 (2009), pp. 730–738.

[157] M. Navarro-Cía et al. "Route for bulk millimeter wave and terahertz metamaterial design". In: *IEEE Journal of Quantum Electronics* 47 (2011), pp. 375–385.

[158] M. Navarro-Cía et al. “Extraordinary THz transmission with a small beam spot: the leaky wave mechanism”. In: *Advanced Optical Materials* 6 (2018), p. 1701312.

[159] F. Miyamaru and M. Hangyo. “Far-field and near-field physics of extraordinary THz transmitting hole-array antennas”. In: *Applied Physics Letters* 84 (2004), pp. 2742–2744.

[160] T. Matsui et al. “Transmission resonances through aperiodic arrays of subwavelength apertures”. In: *Nature* 446 (2007), pp. 517–521.

[161] M. Beruete, U. Beaskoetxea, and T. Akalin. “Flat Corrugated and Bull’s-Eye Antennas”. In: *Aperture Antennas for Millimeter and Sub-Millimeter Wave Applications*. Springer, Cham, 2018.

[162] D. R. Jackson and A. A. Oliner. “Modern Antenna Handbook”. In: Hoboken, NJ, USA: Wiley-Blackwell, 2017. Chap. Leaky-Wave Antennas.

[163] K. S. Reichel et al. “Extraordinary optical transmission inside a waveguide: spatial mode dependence”. In: *Optics Express* 24 (2016), pp. 28221–28227.

[164] M. Beruete et al. “Circuit approach to the minimal configuration of terahertz anomalous extraordinary transmission”. In: *Applied Physics Letters* 98 (2011), p. 014106.

[165] M. Beruete, M. Navarro-Cía, and M. Sorolla. “Understanding anomalous extraordinary transmission from equivalent circuit and grounded slab concepts”. In: *IEEE Transactions on Microwave Theory Technology* 59 (2011), pp. 2180–2188.

[166] J. Bravo-Abad et al. “How light emerges from an illuminated array of subwavelength holes”. In: *Nature Physics* 2 (2006), pp. 120–123.

[167] U. Beaskoetxea et al. “3D-Printed 96 GHz Bull’s-Eye Antenna with Off-Axis Beaming”. In: *IEEE Transactions on Antennas and Propagation* 65 (2017), pp. 17–25.

[168] U. Beaskoetxea et al. “77-GHz High-Gain Bull’s-Eye Antenna With Sinusoidal Profile”. In: *IEEE Antennas and Wireless Propagation Letters* 14 (2015), pp. 205–208.

[169] M. Guillaume et al. "Observation of enhanced transmission for s-polarized light through a subwavelength slit". In: *Optics Express* 18 (2010), pp. 9722–9727.

[170] S. A. Kuznetsov, V. V. Kubarev, and P. V. Kalinin. "Electroformed metal mesh THz-filters for selecting harmonics of NovoFEL radiation". In: *2008 33rd International Conference on Infrared, Millimeter and Terahertz Waves*. 2008, pp. 1–1.

[171] N. Yudasari, J. Anthony, and R. Leonhardt. "Terahertz pulse propagation in 3D-printed waveguide with metal wires component". In: *Optics Express* 22.21 (2014), pp. 26042–26054.

[172] T. H. Isaac, W. L. Barnes, and E. Hendry. "Determining the terahertz optical properties of subwavelength films using semiconductor surface plasmons". In: *Applied Physics Letters* 93 (2008), p. 241115.

[173] J. G. Han, X. C. Lu, and W. L. Zhang. "Terahertz transmission in subwavelength holes of asymmetric metal-dielectric interfaces: the effect of a dielectric layer". In: *Journal of Applied Physics* 103 (2008), p. 033108.

[174] C. Russell et al. "Integrated on-chip THz sensors for fluidic systems fabricated using flexible polyimide films". In: *IEEE Transactions on Terahertz Science and Technology* 6.4 (2016), pp. 619–624.

[175] A. Treizebre S. Laurette and B. Bocquet. "Corrugated Goubau lines to slow down and confine THz waves". In: *IEEE Transactions on Terahertz Science and Technology* 2 (2012), pp. 340–344.

[176] Y. Zhang et al. "Terahertz spoof surface-plasmon-polariton subwavelength waveguide". In: *Photonics Research* 6.1 (2018), pp. 18–23.

[177] M. Navarro-Cía et al. "Broadband spoof plasmons and subwavelength electromagnetic energy confinement on ultrathin metafilms". In: *Applied Physics Letters* 17 (20 2009), pp. 18184–18195.

[178] S. M. Hanham et al. "Exploiting plasmonics for THz and infrared sensing". In: *Proceedings Volume 9102, Terahertz Physics, Devices, and Systems VIII: Advanced Applications in Industry and Defense* (2014), 91020J.

[179] M. Ayata et al. "High-speed plasmonic modulator in a single metal layer". In: *Science* 358 (2017), pp. 630–632.

[180] F. J. Garcia-Vidal, L. Martín-Moreno, and J. B. Pendry. "Surfaces with holes in them: new plasmonic metamaterials". In: *Journal of Optics A: Pure and Applied Optics* 7.2 (2005).

[181] S. Papantonis, S. Lucyszyn, and E. Shamonina. "Dispersion effects in Fakir's bed of nails metamaterial waveguides". In: *Journal of Applied Physics* 115 (2014), p. 054903.

[182] C. A. Fernandes M. G. Silveirinha and J. R. Costa. "Electromagnetic Characterization of Textured Surfaces Formed by Metallic Pins". In: *IEEE Transactions on Antennas and Propagation* 56.2 (2008), pp. 405–415.

[183] P. A. Belov et al. "Strong spatial dispersion in wire media in the very large wavelength limit". In: *Physical Review B* 67 (2003), p. 113103.

[184] K. W. Steijn, R. J. Seymour, and G. I. Stegeman. "Attenuation of far-infrared surface plasmons on overcoated metal". In: *Applied Physics Letters* 49.18 (1986), pp. 1151–1153.

[185] C. R. Williams et al. "Highly confined guiding of terahertz surface plasmon polaritons on structured metal surfaces". In: *Nature Photonics* 2.3 (2008), pp. 175–179. ISSN: 17494885.

[186] S. Pandey et al. "Non-Drude like behaviour of metals in the terahertz spectral range". In: *Advances in Physics: X* 1.2 (2016), pp. 176–193.

[187] C. R. Williams et al. "Dual band terahertz waveguiding on a planar metal surface patterned with annular holes". In: *Applied Physics Letters* 96.1 (2010), p. 011101.

[188] J. Saxler et al. "Time-domain measurements of surface plasmon polaritons in the terahertz frequency range". In: *Phys. Rev. B* 69 (15 2004), p. 155427.

[189] A. Roggenbuck et al. "Broadband Continuous-Wave Terahertz Coherent-Wave Terahertz Spectroscopy on Solid-State Samples". In: *New Journal of Physics* 12 (2010).

[190] S. Yamauchi et al. "Terahertz Time-Domain Spectroscopy to Identify and Evaluate Anomer in Lactose". In: *American Journal of Analytical Chemistry* 4.12 (2013), pp. 756–762.

[191] S. Saito et al. "First Principles Calculation of Terahertz Vibrational Modes of a Disaccharide Monohydrate Crystal of Lactose". In: *Japanese Journal of Applied Physics* 45.11L (2006).

[192] H. F. Ma et al. "Broadband and high-efficiency conversion from guided waves to spoof surface plasmon polaritons". In: *Laser Photonics Reviews* 8 (2014), pp. 146–151.

[193] P. N. Penchev. "Reconfigurable laser micro-processing systems: Development of generic system-level tools for implementing modular laser micro-manufacturing platforms". In: *University of Birmingham* (2016).

[194] Alicona. "Form and roughness in one system". In: *Alicona Focus Variation magazine* Edition 5 (2015).

[195] Alicona Imaging. "IF-Measure Suite manual". In: *Alicona measuring suite manual* Version 4.1 (2013).

[196] *BN ISO 4287/4288. Geometrical Product Specifications (GPS) – Surface texture: Profile method – Terms, definitions and surface texture parameters.*

[197] *ISO 1101. Geometrical Product Specifications (GPS)- Geometrical tolerance - Tolerances of form, orientation, location and run-out.*

[198] F. Capasso, C. Sirtori, and A. Y. Cho. "Coupled quantum well semiconductors with giant electric field tunable nonlinear optical properties in the infrared". In: *IEEE J. Quantum Electron.* 30 (1994), p. 1313.

[199] K. S. Breuer P. Huang and J. S. Guasto. *Evanescent Wave Microscopy, Encyclopedia of Microfluidics and Nanofluidics*. Springern New York NY, 2015. ISBN: 978-1-4614-5488-5.

[200] Y.C. Sim et al. "Terahertz imaging of excised oral cancer at frozen temperature". In: *Biomedical Optics Express* 4.8 (2013), pp. 1413–1421.

[201] H. Chen et al. "Performance of THz fiber-scanning near-field microscopy to diagnose breast tumors". In: *Optics Express* 19.20 (2011), pp. 19523–19531.

[202] S. J. Oh et al. "Study of freshly excised brain tissues using terahertz imaging". In: *Biomedical Optics Express* 5.8 (2014), pp. 2837–2842.

[203] M. Kulya et al. "Spatio-temporal and spatiospectral metrology of terahertz broadband uniformly topologically charged vortex beams". In: *Applied Optics* 58.5 (2019), A90.

[204] M. Kulya et al. "Modeling of referenceless holographic recording and reconstruction of images by means of pulsed terahertz radiation". In: *Journal of Optical Technology* 74.11 (2007), p. 745.

[205] S. Freer et al. "Temperature Dependent Hyperspectral Terahertz Imaging of Human Bone for Disease Diagnosis". In: *SPIE Photonics West 2022* (2022).

[206] B. R. Hibbins A. P.and Evans and J. R. Sambles. "Experimental verification of designer surface plasmons". In: *Science* 308 (2005), pp. 670–672.

[207] W.X. Tang et al. "Concept, Theory, Design, and Applications of Spoof Surface Plasmon Polaritons at Microwave Frequencies". In: *Advanced Optical Materials* 7 (2018).

[208] F. J. Zucker. *Surface-Wave Antennas*. Antenna Engineering Handbook, 1988.

[209] S. Freer et al. "Metal 3D Printed D-Band Waveguide to Surface Wave Transition". In: *2020 45th International Conference on Infrared, Millimeter, and Terahertz Waves (IRMMW-THz)*. 2020, pp. 1–2.

[210] M.M. Nazarov et al. "Characterization of highly doped Si through the excitation of THz surface plasmons". In: *IEEE Transactions on Terahertz Science and Technology* 5 (2015), pp. 680–686.

[211] TeraSense Group. *Sub-Thz Imaging Cameras*. 2019. URL: http://terasense.com/products/sub-thz-imaging-cameras/ (visited on 08/18/2019).

[212] TeraSense Group. *Terahertz Sources*. 2019. URL: http://terasense.com/products/terahertz-sources/ (visited on 08/18/2019).